Academic Year
2018/2019
PhD in
BioRobotic
XXXI Cycle

Tactile Sensing and Haptic Technologies for BioRobotic Applications

AUTHOR:
Luca Massari

SUPERVISOR:
Prof. Arianna Menciassi

TUTORS:
Dr. Calogero Maria Oddo
Dr. Gastone Ciuti

EXTERNAL TUTORS:
Dr. Edoardo Sinibaldi

Table of Contents

1 Introduction

1.1 The Era of Touch

Touch plays a key role in human interaction with the surrounding environment by encoding information about properties such as temperature, pain, force, pressure, texture and shape detection. Information arises from the multiple receptors available within the human skin, in particular in hands and fingers, [1], [2]. Tactile sensing supports most of the manipulation tasks such as object handling, grasping, controlling and many other associated tasks, [3]. Furthermore, tactile sensing allows determining, by means of contact, objects physical properties. During manipulation, the hand partially occludes the object from sight. Thus, tactile sensing allows to obtain measurements in areas that are inaccessible through vision. Prior behavioural studies have demonstrated the tactile reliance of human manipulation, for both simple grasping and dexterous manipulation. Artificial tactile sensors should be able to measure contact conditions such as force and location and to retrieve related geometrical information. The fields of application of tactile sensing include prosthetics, [4]–[6], medicine, [7], dentistry, [8], minimally invasive surgery, [9], augmented and virtual reality, [10], [11], telepresence, [12], [13], mechatronics, [14] and robotics, [15]–[17]. Providing a tactile feedback is essential in order to perform manipulation tasks autonomously or to retrieve interaction information, [18]–[20].

1.2 General aim of the Thesis

The scientific challenge of this PhD thesis is to devise new tactile sensors and haptic interfaces, identifying innovative solutions in terms of design and development, exploiting them for applications in different biorobotics fields such as: medical robotics, wearable technologies, collaborative robotics, neuroscience robotics, rehabilitation robotics and implantable technologies. Touch is deeply involved and highly relevant in Biorobotics applications that rely on tactile information as main communication channel, such as surgical robotics, prosthesis, telepresence and collaborative robotics. Several aspects have been taken in account in order to find novel solutions going beyond the state-of-the-art. In particular, such thesis contributes to the fields of touch for biorobotics application with soft tactile sensors, tactile sensing through mechatronic platform and haptic interfaces for telepresence. The research work that was

performed within this topic during the PhD program of the candidate, is presented in this thesis dividing it in three main sections concerning: i) Optical sensing solution for soft tactile sensor array, ii) Tactile sensing through mechatronic platform for medical applications and iii) Haptic feedback for medical telepresence applications.

The Section 1 is further divided in three case studies that explain the use of embedded optical fibers as sensing elements in soft tactile sensors, in particular focusing on the Fiber Bragg Grating (FBG) technology. Thanks to their characteristics such as flexibility, electromagnetic immunity, high sensitivity, light weight, multiplexing and distributed sensor capabilities, optical sensing technologies can be considered as an good alternative to conventional transducers. In Section 1.1 after a short explanation of the transduction principle, it is explained the design and development of a novel soft tactile sensors array able to solve both contact location and force. Such a sensor has been characterized through a mechatronic platform with 4 degree of freedom (X-Y-Z and Rotation) developed to perform automatic force-controlled indentation throughout the sensor surface. The promising results obtained from this soft sensor paved the path for the development of new tactile sensors (based on the same concept and technology) that were integrated onto a robotic hand for tactile sensing and control of the robotic manipulator (Section 1.2) and on a custom human-like robotic forearm to mimic the human skin (Section 1.3).

Section 2 of this thesis deals with the development of a mechatronic platform, which was also adopted to characterize the soft sensor described in Section 1.1. Such a robotic platform was used for detection of nodules in anatomopathological analyses via force and ultrasound measurements (Section 2.1) and for the experimental evaluation of the fingertip of a biomimetic finger able to reproduce the tactile feedback as the one provided by the spiking activity of human mechanoreceptors (Section 2.2). Three motorized translational stages ensured the motion of the sensor along X-Y-Z axes, while a motorized rotational stage ensured the rotation along one of the axis. A probe, with varying diameter depending on the application, was used to indent the sample. A load cell mechanically linked to the indenter, was employed to collect data about the force arising from the contact between sensor and probe. Moreover, such

a load cell was responsible of the trigger generated upon reaching the threshold value (F_{MAX}) used to pilot the indentations.

The last Section (Section 3) of this thesis refers to the development of an haptic interface based on a piezoelectric transducer embedded in a soft polymer to deliver vibro-tactile feedback in telepresence conditions. Section 3.1 presents the design, fabrication procedure and characterization for the developed vibro-tactile haptic transducer with polymeric encapsulation. In Section 3.2 we present a tactile telepresence system for real-time transmission of information about object stiffness to the human fingertips. Experimental tests were performed across two laboratories (Italy and Ireland). In the Italian laboratory, a mechatronic sensing platform (the same mentioned in previous Section 1 and 2) indented different rubber samples. Information about rubber stiffness was converted into on-off events using a neuronal spiking model and sent to a vibro-tactile glove in the Irish laboratory. Moreover, going further in this direction, in Section 3.3 we present a tele-palpation apparatus that enables the user to detect nodules with various distinct stiffness buried in an ad-hoc polymeric phantom for medical applications.

In the present thesis, the candidate exploited different aspects related to the touch area with different approaches, that are connected between them through the design and development of a robotic platform. The proposed platform has been used for detection of nodules in anatomopathological analyses (Section 2), for characterization of the human-like soft skin (Section 1) and for the telepresence applications (Section 3).

1 Optical Sensing Solution for Soft Tactile Sensor Array

1.1 A Machine-Learning-Based Approach To Solve Both Contact Location And Force In Soft-Material Tactile Sensors[1]

1.1.1 Framework

Tactile sensing allows determining, by means of contact, objects physical properties. Touch plays a key role in human interaction with the surrounding environment by encoding information about properties such as temperature, pain, force, pressure, texture and shape detection. Information arises from the multiple receptors available within the human skin, in particular in hands and fingers, [1], [2]. Moreover, tactile sensing supports most of the manipulation tasks such as object handling, grasping, controlling and many other associated tasks, [3]. Artificial tactile sensors should be able to measure contact conditions such as force and location and to retrieve related geometrical information. The fields of application of tactile sensing include prosthetics, [4]–[6], medicine, [7], dentistry, [8], minimally invasive surgery, [9], augmented and virtual reality, [10], [11], telepresence, [12], [13], mechatronics, [14] and robotics, [15]–[17]. Providing a tactile feedback is essential in order to perform manipulation tasks autonomously or to retrieve interaction information, [18]–[20].

Conventional tactile sensors are usually built using inflexible and relatively stiff materials, that limit their capacity to deform or to adapt their shapes to external constraints. Regardless of their high resolution or precision, such sensors tend to be functional only in a specific domain. The emerging class of soft materials, which includes deformable components such as gels, polymers and fluids, represents a solution for the increasing demand of flexibility, [21]–[24]. Nowadays, state-of-the-art provides evidence of development of soft tactile sensors used in several applications, [25]–[30]. Next soft tactile sensor generations will be able to change configuration

[1] This section has been excerpted from the paper, [280], that is under review in an international scientific journal, with the PhD candidate being first author of the study.

depending on the surface where they are attached. Along this trend, in this work we adopt a soft material to realize a flexible tactile sensor. The transducer has to be flexible as well, so as to be integrated in the soft matrix. Among all the available technologies, optical fibers can successfully meet the aforementioned requirements. The use of optical fibers as sensing elements in tactile sensors is growing fast thanks to their characteristics such as flexibility, electromagnetic immunity, high sensitivity, light weight, multiplexing and distributed sensor capabilities, [31]–[34]. Such sensors can be considered as a good alternative to classic sensors to measure mechanical variables. Indeed, optical fibers have been used with promising results in different scenarios, such as smart textiles, [35], automotive, [36], medicine, [37], and civil engineering, [38]. Fiber optic-based sensors can be developed in different ways depending on the adopted working principle, for example: hybrid optoelectronic, [39], micro and macro bending [40], [41], interferometry, [42], and Fiber Bragg Grating (FBG) sensors, [43]–[45]. The latter technology was chosen for our sensor, due to its reliability in measuring strain and capability to use a single fiber for reading information from multiple transducers, via wavelength separation, [46]–[52]. State-of-art on FBG technology gives evidence of different scenarios. Typically such gratings are used as elongation sensors leveraging the axial deformation of the gratings, with illustrative applications including cardiac and respiratory monitoring, [53] structural monitoring of bridges, [54] and tissue palpation in minimally invasive surgery, [44]. Moreover, FBGs have been successfully used also for the development of tactile sensors, [55]. In this work we present a soft tactile sensor based on FBG sensing elements that, compared to related works, [45]–[48], [52] shares the idea of embedding the optical fiber inside a soft polymer that mediates loads applied to the buried FBGs. Amongst the available soft materials we chose to adopt Dragon Skin 10 medium (Smooth-on, USA) due to its low delamination and high flexibility, and investigated its behaviour with the developed FEM numerical model. Within this paper we intend to measure the force and, simultaneously, to locate the point of contact between the sensor and the objects. Accurate detection of both variables is crucial for many applications and it is still an open research topic. We defined the force range (up to 2.5N), by considering gentle touch tasks like those typically occurring in fine manipulation activities, [13], [56]–

[59]. Moreover, we advance the state of the art by proposing a model-based calibration to obtain the sensor inverse function using machine learning. A neural network for force coding of a tactile sensor based on Fiber Bragg Grating was proposed by Saccomandi et al., [45] whereas, differently from this work, the training set was retrieved exclusively from experimental data and there was no indentation localization Provided that the model is accurate, this approach can significantly reduce individual calibration requirements of soft tactile sensors and the time to market, enhancing their industrial impact. In particular, a Finite Element Model (FEM) simulation of the sensor has been employed to generate a huge set of data to train a neural network, later validated through experimental data, and thus getting the inverse function from the sensor output, namely the load amplitude and position. Moreover, the numerical model has been used to study the variation in the FBGs output as consequence of changes of design parameters such as the thickness of the soft encapsulating material, in searching the optimal trade-off between sensitivity and receptive field. Our investigation on the effect of thickness complements the study recently published by Lun et al., [60] focused on shape sensing.

The present work is organized as follows: in the Materials & Methods Section, we present the sensor design followed by the numerical model and the adopted constraints. Then, a brief description on the FBG working principle and its application to our sensor is given. Both numerical and experimental results, discussion and concluding remarks are presented in the Results & Discussion Section: model simulation, experimental data, comparison between model and experimental data and neural networks results.

1.1.2 Materials & Methods

DEVELOPMENT OF SOFT SENSOR INTEGRATING FBG TRANSDUCERS

The sensor was fabricated by embedding an optical fiber throughout a soft polymeric matrix in order to obtain a thin and flexible pad, leading to sensors that could be easily wrapped, embedded or attached onto a specific surface.

A Fiber Bragg Grating (FBG) is a microstructure with a typical length between 1 mm and 24 mm inscribed in the core of a single mode optical fiber. The realization process is based on the transverse illumination of the fiber with an ultraviolet laser beam and the

generation of an interference pattern in its core through a phase mask. Therefore, a resonant structure is created by means of a spatial periodic modulation of the refraction core index. When a light source is injected into the optical fiber, generally with an optical interrogator, the FBG acts as a narrow band filter: part of the light is transmitted and goes through the fiber, while another narrow part is reflected back. Such a reflected spectral segment is centred around the Bragg wavelength (λ_B) and it is defined by the effective refraction index (n_{eff}) of the fiber core and the grating period (Λ_B) as in Equation 1:

$$\lambda_B = 2\, n_{eff}\, \Lambda_B \quad (1)$$

FBGs are sensitive strain, that leads to variations of λ_B. One of the biggest advantages of FBGs is the possibility to add multiples gratings in a single optical fiber, provided that a constraint is respected: all the reflected wavelengths need to be different, thus avoiding overlapping and consequentially data loss from one or more gratings. The chosen optical fiber (DTG's In Reduced Cladding Fibers, FBGS, Geel, Belgium), 115 µm of diameter, housed 4 FBGs, placed along its length in selected slots. Each grating was 8 mm long and spatially coupled with the adjacent FBG providing a short interval (centre to centre) of 12 mm (*d*) between FBG1-FBG2 and FBG3-FBG4, and a long interval of 48 mm (*3d*) between FBG2-FBG3 (Figure 1A). FBG1 and FBG2 were placed at a short distance (d) to evaluate the crosstalk between close adjacent gratings. Then a longer distance (3d) was set between FGB2 and FBG3 so to evaluate the relationship between material thickness and sensors positioning with respect to combined force-position measurement accuracy. Furthermore, the fourth grating (FBG4) was added for obtaining a symmetric configuration (FBG1-FBG2 versus FBG3-FBG4) that was also functional for investigating reproducibility in a single setup. The following nominal reflected wavelengths have been chosen for the FBGs in the proposed sensor: 1544 nm, 1546 nm, 1553 nm, 1555 nm (from FBG1 to FBG4). The polymer employed to cover the sensor was Dragon Skin (10 medium, Smooth-on, USA). This silicone rubber is highly stretchable (high elongation at break), [61], and soft (shore A 10), thus enabling the sensor to be twisted, wrapped, bent and stretched within optical fiber physical limits (Figure 1C). Moreover, such a rubber allows proper demoulding of the sensor, without delamination of the thin polymer layer.

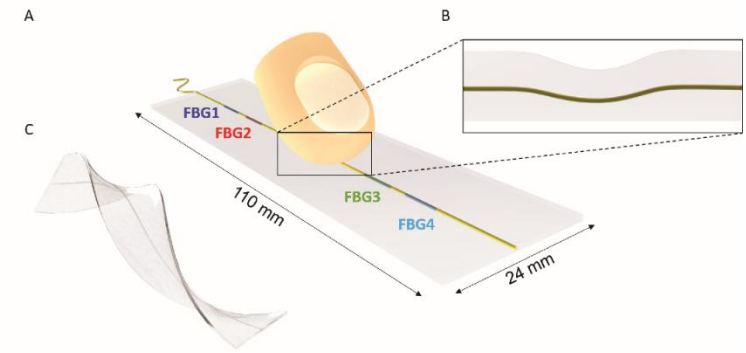

Figure 1: A. Ultra-soft tactile sensor array integrating Fiber Bragg Grating (FBG) transducers (marked in colours). B. Inset of the sensor highlighting the effect of the applied load on it. C. Deformability and ultra-soft properties of the sensor.

The sensors had a parallelepiped shape and same physical dimension apart from the thickness (thickness refers to the whole encapsulating material, with the optical fiber embedded at the middle of the brick). They were 110 mm long, 24 mm wide and with a variable thickness, ranging from 1 mm to 8 mm in the performed FEM simulations. Following the simulations, two sensors were fabricated, with 1 mm and 6 mm thickness, respectively. The optical fiber was aligned with the longitudinal axis and laterally centred in the middle of the brick. During the fabrication process, the liquid polymer was casted inside a customized mould. To minimize air bubbles, vacuum degassing of the liquid rubber was performed before casting. The optical fiber was held in the desired position in the mould before starting the casting process. The rubber was cured at room temperature until solidification and subsequent demoulding of the sensor.

As showed in Figure 1A, we applied loads along the sensor top surface. The polymeric matrix mediated the transmission of the applied load to the optical fiber, thus passing from an unstrained to a strained condition, as highlighted in the inset (Figure 1B). Figure 2 explains the FBG working principle applied to our study. In the upper part of the figure a lateral view of the sensor is presented, illustrating 6 example cases, from no indentation (N) to indentation in five locations (P1-P5). In the bottom part of Figure 2 the outputs of two FBGs are displayed per each case in either the 1 mm thick sensor and

the 6 mm thick sensor. Each case refers to a particular indentation site, apart from N, which represents the null load condition (unstrained condition for the optical fiber). P2 and P4, correspond to the cases where the load is applied above FBG1 (for P2) and FBG2 (for P4). Such conditions represent, respectively, the cases with max strain suffered by FBG1 and FBG2 and thus with max shift of the reflected signals, since higher strain entails higher grating period variation and thus higher shifts of the reflected wavelengths. The effect of the thickness of the soft polymeric packaging material on the strain acting on the optical fiber is investigated in the present study.

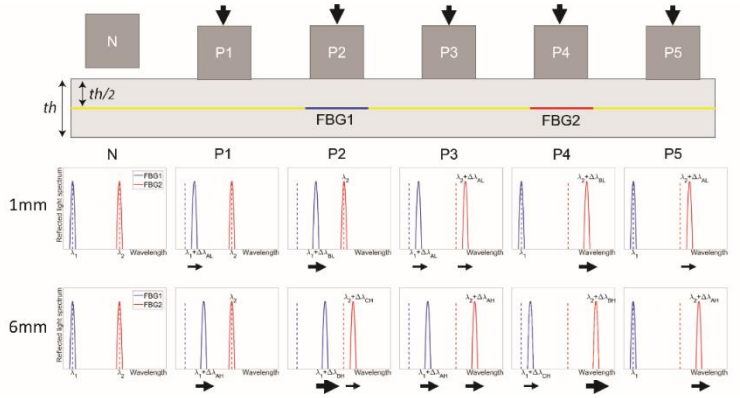

Figure 2: Working principle of the FBG transducers in the developed phantom. Only FBG1 and FBG2 are showed for ease of illustration

Soft sensor Finite Element Model simulation

A FEM simulation of the sensors was performed by means of COMSOL Multiphysics (COMSOL Inc., Palo Alto, CA, USA), with the structural mechanics module. Such simulations addressed the evaluation of load/unload cycles applied onto the sensor surface. Moreover, we investigated the effect of thickness in determining a suitable trade-off between receptive field and sensitivity. The developed model was employed to generate a very large dataset to train a neural network to obtain the sensor inverse function, namely the detection of the indentation sites and the applied load. The model reproduced the sensor with parametric thickness, in the 1 mm – 8 mm range. We assumed to deal with linear elastic sensor deformations (working assumption). Hence, we defined the Young modulus (E), Poisson coefficient (*v*) and density (*d*) for both the

encapsulation polymer and the optical fiber. In literature, [62]–[65], we found the following values for the rubber: E = 100 kPa, ν = 0.49, d = 1070 kg/m^3, while, for the optical fiber we adopted the values reported in the datasheet, *i.e.,* E = 36 GPa, ν = 0.17, d = 2203 kg/m^3. The simulation was based on the experimental protocol described in the following paragraph, which consisted in applying a load onto a specific location of the sensor through a cylindrical indenter. The load was applied on an area equal to the size of the cylindrical indenter surface along the sensor top side. Each pair of force and position values corresponded to a certain strain of the fiber. In this work, the used force ranged between 0.1 N to 2.5 N, with steps of 0.1 N, and the indentation position between 0 and 86 mm, with steps of 0.25 mm. Since the sensor was attached to a flat rigid surface, in the FEM simulation a null displacement was set at the bottom surface of the sensor. We assumed a perfect bonding between the optical fiber and the encapsulation polymer. We adopted some simplifications in the model in order to reduce the computational time to retrieve the solution. Taking into account the small diameter of the optical fiber, Ø115 µm, with respect to the thickness of the sensor (1 mm or 6 mm), we described the optical fiber by means of a truss element, *i.e.,* a slender member that can only sustain axial forces. Such a modification allowed to treat the optical fiber as a 1D solid. Moreover, thanks to the symmetry of the sensor, we only considered half sensor, thus further reducing the computational burden. Mesh-independence was carefully obtained through preliminary runs. In particular we applied a finer mesh around the optical fiber and on the surface where we applied the normal load (*i.e.,* indenter area).

EXPERIMENTAL SETUP AND PROTOCOL

The experimental phase was carried out by means of a mechatronic platform, developed to perform automatic force-controlled indentation throughout the sensor surface (Figure 3A-D). Three motorized translational stages ensured the motion of the sensor along X-Y-Z axes. Such stages allowed motion with 2.5 µm step resolution along the horizontal X-Y axes (8MTF-102LS05, STANDA, Vilnius, Lithuania) and motion with 5 µm step resolution along the vertical Z axis (8MVT120-25-4247). An aluminium cylindrical probe of 6 mm diameter was used to indent the sample. A load cell (Nano 43, ATI Industrial Automation, Apex, NC, USA), mechanically linked to the indenter, was employed to collect data about the force arising from the contact between sensor and probe. Moreover, such a load cell

was responsible of the trigger generated upon reaching the threshold value (F_{MAX}) used to pilot the indentations. An optical interrogator (si425, Micron Optics, Atlanta, USA) was used to collect the data coming out from the FBGs transducers, namely the reflected wavelengths of the different gratings. All the components of the setup were controlled through LabVIEW routines (National Instruments Corp., Austin, USA) by means of a PC Graphical User Interface (GUI) (Figure 3E). Furthermore, using such software ensured the synchronization of the data coming out from the load cell and the optical interrogator, thus enabling and facilitating data elaboration.

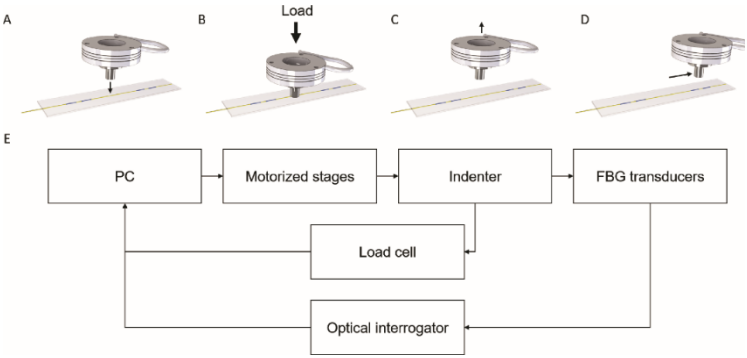

Figure 3: A-D. Indentation process during the experimental acquisition (the direction of the arrow indicates relative motion). E. Block diagram of the experimental setup.

The protocol consisted in automatic force-controlled indentations of the sensor in different sites and using several F_{MAX} (*i.e.,* load/unload cycles). We considered as reference position a point located 12 mm before the centre of the first grating (FBG1). The X coordinates of the indentations ranged from this reference position up to 86 mm with 2 mm steps. The F_{MAX} ranged from 1 N up to 2.5 N with steps of 0.5 N (*i.e.,* on each site 4 indentations were performed). Considering such a procedure, we obtained 176 load/unload indentations (44 sites and 4 forces), that were repeated 3 times each.

FEM-BASED MACHINE LEARNING TO RETRIEVE SENSOR INVERSE FUNCTION AND EXPERIMENTAL DATA ANALYSIS

As a first step, we assessed the predictive capability of the numeric model that was used to train a neural network so as to obtain the inverse sensor function. During the experimental sessions,

indentation force values, indentation sites and FBGs reflected wavelengths were stored. In particular, per each indentation we retrieved the maximum normal force value, the position of the indenter and the corresponding reflected wavelength of the four FBGs. Such values were then compared with the numerical model output to validate the proposed simulations. The strain suffered by the fiber during the load/unload cycle of the cylindrical indenter was retrieved from the FEM simulations. Moreover, the solid displacement of the soft polymer and the coupled relative displacement of the optical fiber were analysed. Each pair of probe position and exerted force corresponded to a certain axial strain of the fiber. Since the position of the 4 FBG transducers along the fiber, the F_{MAX} level and the indentation sites were known experimental parameters, we used the Δε, retrieved from the numerical model to build the sensor direct function and, thus, obtaining the reflected wavelengths. The strain was converted into reflected wavelengths via Equation 2.

$$\Delta\lambda = 0.78 \cdot \lambda \cdot \varepsilon \quad (2)$$

Where λ is the reflected wavelength and ε is the strain suffered by the fiber. To obtain the sensor inverse function using machine learning we designed a cascade of two feedforward neural networks, each with 10 hidden neurons. The architecture of each neural network was a two-layer feed-forward network with sigmoid hidden neurons and output neurons. The Levemberg-Marquardt method was employed to train the network. The first neural network (NN1) had 4 inputs, which were the FBGs reflected wavelengths, and 1 output, which was the estimated position. The second neural network (NN2) was in cascade, with 5 inputs, which were the 4 FBGs reflected wavelengths plus the position estimated by NN1, and 1 output, which was the estimation of the applied force (Figure 4B). For both the neural network cascade (NN1 and NN2), we employed the FEM model data as training set, part of the the experimental data (25% of the total) as the validation set and the rest of the experimental data (75% of the total) as test set. FEM model data were employed to train both the neural networks, by using the Levenberg-Marquardt training algorithm. To assess the neural networks performance, Root Mean Square Error (RMSE) and correlation coefficient (R) between output and target were estimated. We applied the same procedure to the experimental data

as well (Figure 4), thus first retrieving the reflected wavelengths from the sensor direct function (experimental), and then obtaining the sensor inverse function using the trained neural network. Experimental data were also used to validate the neural networks. The whole data-processing was performed by means of the Neural Networks toolbox (Matlab, The MathWorks, Inc., MA, USA).

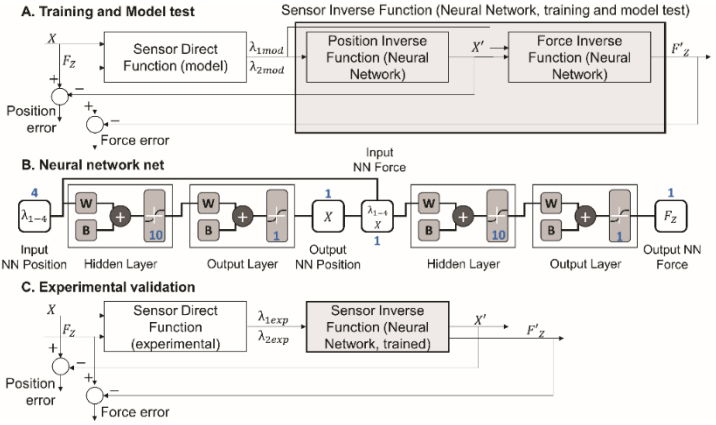

Figure 4: Machine-learning-based construction of the sensor inverse function. A. Block diagram of the training part based on the numerical model. B. Graphical view of the network connectivity C. Block diagram of the validation part based on the experimental data.

1.1.3 Results & Discussion

FEM MODEL RESULTS

Numerical model results are summarized in (Figure 5). Figure 5D shows the model of the 1 mm-thick sensor, with an overall view of the fiber strain. Figure 5E, represents the axial stain suffered by the optical fiber as a function of the distance from the indenter. Figure 5A-C and Figure 5F-H show the behaviour of the encapsulating polymer and of the optical fiber, respectively. The chosen graphs are 2D cut-views on the sagittal plane through the fiber and the indenter axis, and they highlight the solid displacement due to the applied load (on the left for the polymeric matrix, on the right for the optical fiber). For a given load, changes in the sensor thickness lead to a change in the axial strain transduced by the optical fiber, affecting the receptive field. We thus numerically investigated the effect of sensor thickness on the axial strain, which is shown in Figure 6. Counterintuitively, by increasing the thickness, the axial strain

propagating in the soft material up to the FBG sites increases as well in an initial range of thickness. For thickness above 6 mm, the trend reverts and the axial strain starts decreasing.

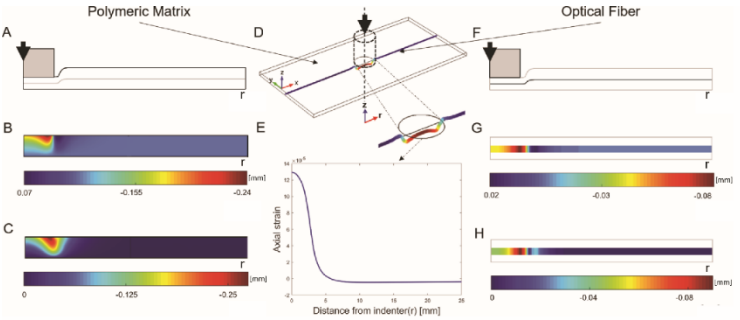

Figure 5: A. Schematic of the solid displacement due to the applied load (half sensor is considered in the whole panel, thanks to symmetry). B. Contour plot of the z displacement of the polymeric matrix versus the radial distance (r) from the indenter axis. C. Contour plot of the displacement of the polymeric matrix. D. 3D view also showing the axial strain experienced by the optical fiber during indentation. E. Graph showing the axial strain versus the radial distance (r). F-G-H. Same of panel A-B-C but for the optical fiber.

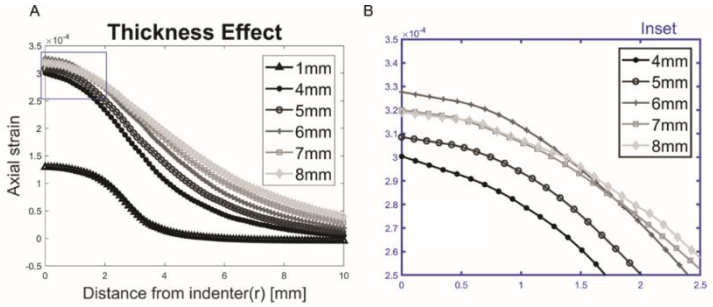

Figure 6: A. Axial strain of the optical fiber for different thickness of the sensor. B. Detail of the panel A highlighting the axial strain under the indenter. As showed in Figure 2 the thickness refers to the whole encapsulating material, with the optical fiber embedded at the middle of the brick.

Experimental results

Figure 7 shows the reflected wavelengths for the 4 FBGs as a function of the indentation location both for the experimented force values and normalized with respect to force, highlighting a linear response in the considered range of forces. This result highlights the difference in receptive field between the 1 mm-thick sensor (dashed lines) and

the 6 mm-thick sensor (straight lines): counterintuitively, for the same load and indentation site, higher thickness values permit to enhance strain transmission. Cross-talk between adjacent FBGs is a key factor since it allows the joint discrimination of force and position by means of the neural network. The output of the thinner sensor has no crosstalk between FBG2 and FBG3 and nearly negligible crosstalk between FBG1 and FBG2 or FBG3 and FBG4, whereas the thicker sensor shows a considerable crosstalk in both cases Moreover, Figure 7D shows the relationship between the sensor output (*i.e.,* wavelength variation) and the applied load for indentations performed with different forces onto the centre of each of the gratings. Figure 7D demonstrates linearity (R^2 = 0.995 for 6mm and R^2 = 0.983 for 1mm) and repeatability (max 0.08nm std and mean 0.018nm std of Δλ over the force range for 6mm and max 0.03nm std and mean 0.007nm std of Δλ over the force range for 1mm), as well as greater sensitivity of the ticker sensor.

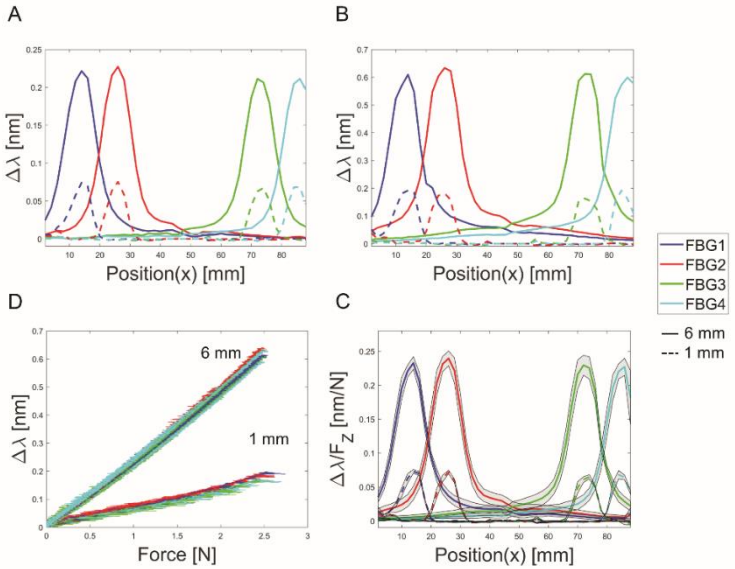

Figure 7: Experimental data showing the wavelength variation of the different FBG sensors as a function of the position of the applied load for both the sensors 1mm (dashed lines) and 6mm (continuous lines). A. The wavelength shift function of the position is represented for 1N indentation force B. The wavelength shift function of the position is represented for 2.5N indentation force C. The wavelength shift per unit indentation force is represented, in order to highlight the linear character observed for the corresponding trend (some deviations being associated with higher indentation

forces) D. Relationship between the sensor output (wavelength variation) and the applied load for indentations performed with different forces onto the centre of each of the gratings. For each thickness (1mm dotted line and 6mm solid line), the plots show 48 datasets: the transient forces spanned while targeting 4 force values (1 N, 1.5 N, 2 N, 2.5 N), for 4 FBG transducers and 3 experimental repetitions.

Model validation

The comparison between numerical simulations and experimental data is shown in Figure 8 (1 mm-thick sensor on the left, 6 mm-thick sensor on the right); reflected wavelength values are shown as a function of the indented points, for all the 4 FBGs. The optical fiber (thick yellow line), the FBG grating (thick blue line) and the indentation sites (black dots) are schematically represented at the bottom of the figure at hand. The reflected wavelength variations predicted by the model (blue line) are directly compared to the experimental data (red dots) per each indentation site and each FBG, showing that the numerical simulations accurately predicted the experimental observation for both sensors.

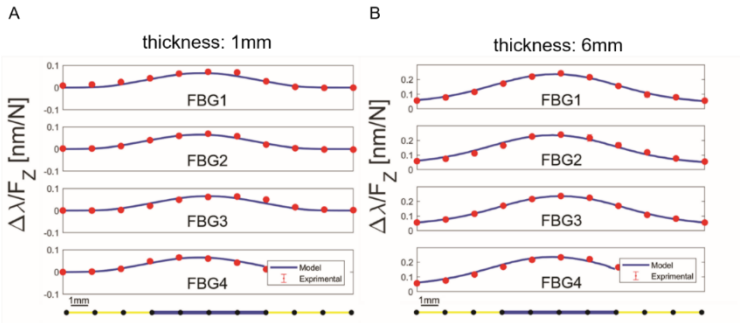

Figure 8: Comparison of the experimental data (red dots) and the model data (blue line) for all the FBG sensors embedded in the soft polymeric matrix. The indented points (black dots) and the position of the FBG (blue line) are shown at the bottom of the figure. The size of the black dots doesn't represent the size of the indenter.

Sensor inverse function

The accuracies in sensing the indentation location by means of the proposed neural networks are reported in Figure 9. Training results, based on the numerical simulation data (for both the 1 mm- and the 6 mm- thick soft sensors) are shown in Figure 9A, while Figure 9B reports the validation results based on the experimental data. Each graph shows the estimated position, namely the output of the neural network, as a function of the nominal position, namely the target of

the neural network. A perfect fit would correspond to a state where network output is equal to the targets (data on the bisecting solid line in figure). The correlation coefficient (R) and Root Mean Square Error (RMSE) were calculated for each case. High R values (R = 0.993 for model training, R = 0.992 for validation and R = 0.9917 for experimental test) and low RMSE values (RMSE = 1.81 mm for model training, RMSE 2.63 mm for validation and RMSE = 2.45 mm for experimental test) were obtained when indenting the thicker sensor (for the thinner one we got R = 0.854 and RMSE = 8.47 mm for model training, R = 0.926 and RMSE = 7.53 mm for validation and R = 0.844 and RMSE = 10.73 mm for experimental test).

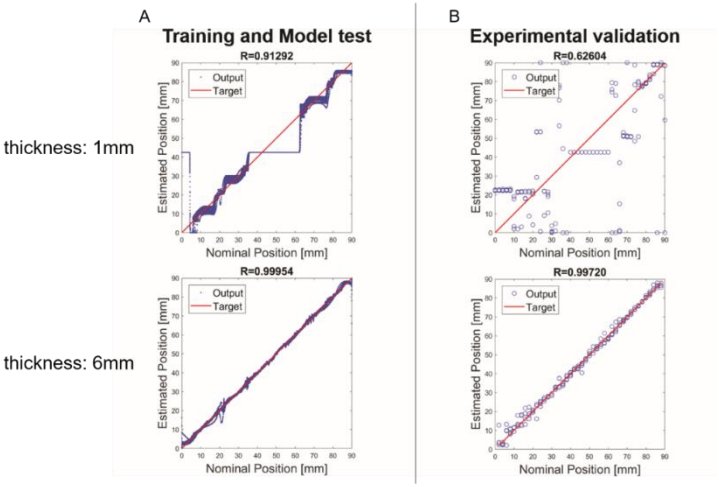

Figure 9: Accuracy in sensing the indentation location by means of the proposed neural network, based on the developed numerical model, for both the 1 mm-thick and the 6 mm thick sensors, Input: reflected wavelengths (λ1; λ2; λ3; λ4), Output: indenter location position along the optical fiber. A. Training results. B. Validation results. C. Test results.

The accuracy in sensing the indentation force is finally shown in Figure 10. We obtained the same trend as that one resulting when estimating the indentation position. High correlation and smaller error were obtained with the thicker sensor: R = 0.998 and RMSE = 0.029 N for the model training, R = 0.979 and RMSE = 0.166 N for validation and R = 0.977 and RMSE = 0.164 N for test (whereas for the thinner one we obtained R = 0.618 and RMSE = 0.52 N for model training, R = 0.306 and RMSE = 0.58 for validation and R = 0.191 and

RMSE = 0.69 N for test). Table 1 summarizes the results of the adopted neural networks.

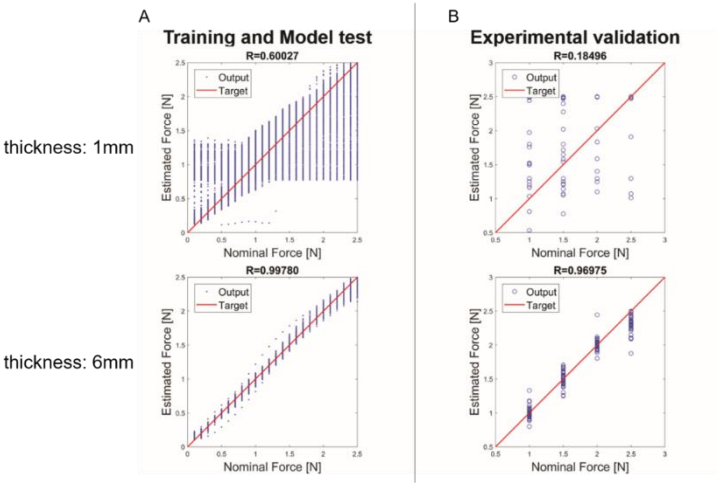

Figure 10: Accuracy in sensing the force exerted by means of the proposed neural network, based on the developed numerical model, for both the 1 mm-thick and the 6 mm thick sensors, Input: reflected wavelengths (λ1; λ2; λ3; λ4) and the probe position along the optical fiber, Output: force along the optical fiber. A. Training results. B. Validation results. C. Test results.

Table 1: Correlation coefficient and root mean square error

	Model training NN1	Model Training NN2	Experimental validation NN1	Experimental validation NN2	Experimental test NN1	Experimental test NN2
R (1mm)	0.85442	0.61882	0.92644	0.30669	0.84419	0.19075
RMSE (1mm)	8.47 mm	0.52 N	7.53 mm	0.58 N	10.7 mm	0.69 N
R (6mm)	0.99272	0.99861	0.99244	0.97938	0.99078	0.97735
RMSE (6mm)	1.81mm	0.029 N	2.63 mm	0.166 N	2.45 mm	0.164 N

Discussions

In this work we presented the model-based development and calibration of a soft tactile sensor able to solve both the magnitude and the position of an applied normal load on its surface. Four FBGs

transducers housed in an optical fiber were embedded in a soft silicone brick. The silicone mediates the transmission of the applied load to the buried FBGs, thus inducing strain on the optical fiber, which in turns induces a shift of the nominal reflected wavelengths of the FBGs. Such a shift depends on both the applied load and the indentation site. We built a numerical model, based on the working assumption of linear elastic sensor deformations in the range of forces considered, successfully validated through experimental results. We used the model to create a large calibration dataset and machine learning to obtain the sensor inverse function.

As part of the numerical investigation, we considered a parametric sweep to probe the effect of sensor thickness on the receptive field of the gratings. Simulations results indicated that, for the chosen working parameters, a thickness of 6 mm contemporarily provided very good crosstalk between sensors and proper sensitivity of individual sensors (whereas the 1 mm-thick crosstalk between adjacent FBGs was much lower). Once calibrated the neural network with numerical results, it was able to resolve the applied normal load (0.97 R) and its location (0.99 R). In this study we exploited widely used NNs available through a common software library: more refined algorithms could be used for achieving higher computational performances (even if the main computational burden with a neural network approach is associated with training, whereas the operation of the trained network is relatively lean). Moreover, since both the receptive field and the sensitivity of the buried FBGs are better in the ticker sensor we claim that the 6mm-sensor shows better performances in terms of localization and intensity prediction. Anyhow, in those application where there are some constraints in terms of thickness or were flexibility is a key factor the 1mm-sensor could be preferable compared to the 6mm-sensor. With respect to previous studies, we originally demonstrated one main element of novelty: the capability to detect simultaneously, using machine learning and a numerical model of the sensor, the location and intensity of an applied load onto soft tactile sensors suitable for covering large areas in robotic applications. Nevertheless, we originally demonstrated a design/calibration methodology that can be extended to a wider set of materials and geometries, thus bringing a positive contribution at the crossroad between machine learning and soft tactile sensors design. The proposed tactile sensor is intended to be wrapped, twisted and attached on different surfaces

and it could be effectively employed for a broad range of applications, including those where electromagnetic immunity is a key requirement (such as magnetic resonance imaging). Scalability is another advantage of the proposed sensor. Indeed, multiple FBGs can be housed along the same optical fiber with only minor arrangements, thus enhancing sensing capabilities without penalizations in terms of bulkiness/complexity. Future studies will address dynamic effects and will involve the development of more complex geometries. As mentioned before, one of the main achievement of the present work is the model-based design and calibration. Starting from such results, future works will involve the development of an artificial skin that aims at localizing the point of contact in a curved 2D matrix and the applied load force.

1.2 Tactile Sensing and Control of Robotic Manipulator Integrating Fiber Bragg Grating Strain-Sensor[2]

1.2.1 Framework

The sense of touch is a key sensory modality of prehensile manipulation. Through tactile perception, humans are able to perceive object properties such as size, hardness, temperature, contour, etc. Information arises from the multiple receptors available within the human skin, especially across hand and fingers, [1], [2]. During manipulation, the hand partially occludes the object from sight. Tactile sensing allows to obtain measurements in areas that are inaccessible through vision. Prior behavioural studies have demonstrated the tactile reliance of human manipulation, for both simple grasping and dexterous manipulation, [3]. In the last years, the field of robotics has expanded toward more complex environments, [66], including dangerous and not accessible scenarios such as nuclear meltdown disasters and space missions to other planets, where robots are demanded to take over human jobs. The successful automation of complex human-like manipulative tasks depends on robot's perception capabilities, including through a tactile sensor, to characterize the relation between the operated objects and the robotic manipulator, [18], [19], [67]. Although the human hand represents a point of inspiration for many prehensile robotic hardware, [68], [69], the field of artificial tactile sensing covers a large spectrum of underlying principles, [70]. The literature, for instance, shows relative success with capacitive, piezoelectric, piezoresistive and resistive sensors. Such sensing systems rely on changes of the measured variable (i.e. capacitance, electrical charge, resistance, etc.) that involve different advantages and disadvantages. Capacitive sensors consist of two conductive plates interfaced by means of a compressible dielectric material, [71]–[73]. The transduction principle relies on the capacitance variations that occur when, during the loading phase, the gap between the plates changes. Such transducers entail high sensitivity and frequency response but are susceptible to electro-magnetic noise, tend to be non-linear and

[2] This section has been excerpted from the paper, [281], that has been published in an international scientific journal: Frontiers in NeuroRobotics, with the PhD candidate being first author of the study.

to have hysteresis. Capacitive sensors are extensively used in robotic applications for tactile feedback, [58], [74]–[76]. Piezoelectric sensors depend on the electrical charge generation in the quartz crystal, as it deforms by applying a load. Such sensors are frequently employed for dynamic sensing, due to a very high frequency response and can be used to build flexible tactile sensors, [56], [77]–[83]. On the other hand, piezoelectric sensors suffer temperature sensitivity and are generally fragile, [84]. Piezoresistive sensors rely upon the electrical changes in resistance occurring to the material during load/pressure application, [85]–[87]. Such sensors are widely used as they are relatively easy to produce and can be flexible, [88]. The main drawbacks of these transducers refer to the low repeatability, fragility to shear forces, non-linear response and hysteresis. Among all the technologies, the use of optical fibers as transducers for tactile sensors is spreading due to the multiple advantages such as: electromagnetic immunity, flexibility, high sensitivity, multiplexing capability and lightness, [31]–[33]. Several studies promote such sensors for different fields of application such as: automotive, [36], medicine, [37] and smart textile, [35] among the other ones. Depending on the working principle, fiber optic based sensors entail different ways of operation: micro and macro bending, [40], [41], interferometry, [42], hybrid optoelectronics, [39] and Fiber Bragg Grating (FBG), [43]. In parallel to the development of tactile sensors, the robotics community has produced a vast amount of research on hand design. Hand design is typically application-driven, leading to different arrangements ranging from simple two-finger grippers to complex contraptions that mimic the mechanics of the human hand [89]–[92]. This work presents the case of a four-finger under-actuated hand (Cam-Hand) that endows Jet Propulsion Laboratory's (JPL) quadruped RoboSimian robot with both manipulation and versatile mobility capabilities [93], [94]. This robot uses its limbs for mobility and manipulation such as grasping. Each seven degree of freedom limb consists of a set of three elbow assemblies and an actuator mechanically linked to the main body. The limbs end with a six-axis force sensor which interfaces the Cam-Hand (Figure 11).

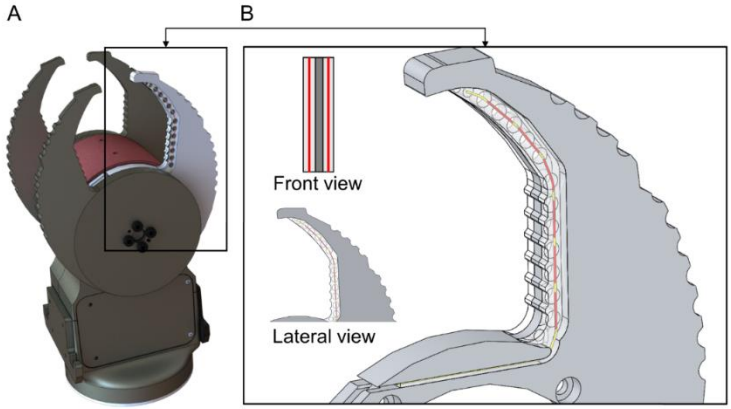

Figure 11: (A) Cam-Hand. (B) Inset of the sensorized finger. The red lines represent the FBGs. Each optical fiber houses 6 FBGs (8mm length).

The hand consists of an aluminium body and four aluminium fingers configured for many uses including being used as a gripper tool. The chosen design, conceived for use in scenarios that require robust manipulation, resulted in a system that enhances grip strength and robustness over dexterity and flexibility. Not being designed to prioritize complex manipulation tasks or handling fragile objects limits the variety of tasks the robot is able to perform. The present work is aimed at overcoming these limitations and enhancing safety and control during interaction with the surrounding environment. The RoboSimian Cam-Hand has been redesigned by sensorizing the artificial fingers to enable tactile feedback. New sensorized robotic fingers have been devised, embedding optical fiber sensing technologies, to gain information on grasped object properties as well as the contact conditions. The choice of the robotic hand sensorization was based on some crucial requirements such as *i)* the ability to provide information about the contact (*i.e.,* intensity), *ii)* the ability to provide information about the grasped objects (*i.e.,* size, rigidity, etc.) and *iii)* the ability to perform manipulation tasks (*i.e.,* estimation of grasp stability), [95]. Moreover, it is worth to mention that the robotic hand presents additional constraints related to the physical integration of the sensors. The adopted technology has to meet the requirements imposed by the robotic hand layout and design. Hence, the sensorization needs to be achieved without affecting the dexterity of the hand, i.e. without drawbacks in terms

of bulkiness and encumbrance. Considering the aforementioned physical and tactile requirements, FBG technology was chosen to realize the sensor due to its adaptability to the design of the artificial hand, for its reliability in strain measurements and for the multiplexing capabilities that entail a high spatial resolution without an overwhelming amount of wires. State-of-art regarding applications adopting FBGs as transducers give evidence of tactile sensors used in different scenarios. Compared to related works (*i.e.,* soft tactile sensors embedding FBGs), [44]–[47], [51], [52], [96], the present sensor shares the concept of encapsulating the optical fiber in a soft matrix. Such cover not only protects the fiber from mechanical ruptures but also affects the transduction of the signal by mediating the transmission of pressure to the buried FBGs. In comparison to previous studies embedding FBGs in prototypical matrices (*e.g.,* parallelogram bricks), the location of our FBGs were based on the design of the robotic hand, expressly functional to gripping tasks. One common elastomer used as encapsulating material is PDMS [45], [46], [52], [96], while in this study a soft Dragon Skin silicone (20 medium, Smooth-on, USA) was used, due to its higher flexibility and lower delamination between layers. Further details on the adopted elastomer, are given in the Materials & Methods Section. The scope of the present study goes beyond the development of a soft and flexible tactile sensor. The novelty of the work also relies in the demonstration of a closed-loop control strategy for fine manipulation (Fragile Task), and in extracting features of manipulated objects, whereas in state of the art studies FBG wavelength variations were used to estimate several quantities (e.g., pressure, force, hardness) but within an open-loop scheme, without affecting the control variable.

1.2.2 Materials & Methods

Fiber Bragg Grating Transduction Principle

An FBG is a reflector, formed by systematic variation of refractive index, inscribed in the core of an optical fiber. This resonant microstructure acts as a narrow band filter. When light propagates along the optical fiber, and reaches the etched FBGs, part of the source is reflected back. This reflected signal is called Bragg Wavelength (λ_B) and it depends on the grating spatial period (Δ_B) and the effective refraction index (η_{eff}) of the optical fiber as in Equation 3:

$$\lambda_B = 2 \cdot \eta_{eff} \cdot \Lambda_B \quad (3)$$

Strain conditions and temperature variations imparted on the FBGs leads to variation of λ_B resulting in changes of the grating spatial period (Λ_B), or effective refraction index (η_{eff}). In the present work the contribution of temperature is negligible, since the whole experimental session was performed at room temperature.

SENSORIZED ROBOTIC HAND DESIGN

The Cam-Hand body houses the driving electronics and three brushed DC motors (Maxon precision motor, Sachseln, Switzerland). The finger geometry follows a cam profile on the outside and a hook style shape on the inner profile. The system is comprised of two outer fingers slaved together and two inner fingers that are independent. Through continuous rotation of the fingers the Cam-Hand is able to achieve a huge number of configurations and grasping angles. The Cam-Hand includes four fingers and. the inner fingers were sensorized due to their independent actuation. Optical fibers (Technica Optical Components, Atlanta, GA, USA) that exhibit a diameter of 80 µm (100 µm with polyimide coating) were chosen since small diameters allows low bending radius configurations. The fibers house 6 FBGs, each grating is 8 mm long and located at a distance of 10 mm, centre-to-centre, from the adjacent FBG. Table 2 provide further details about the chosen technology.

Table 2: Datasheet of the optical fibers integrating FBG transducers

Reflectivity	Coating	Wavelengths	SLSR*	FWHM**
>70%	Polyimide	1535:5:1570 nm	>15db	0.5nm

*SLSR: Side Lobe Suppression Ratio
**FWHM: Full Width Half Max

The optical fibers were encapsulated in a soft polymeric material integrated into the rigid artificial finger. According to previous works, [12], Dragon Skin (20 medium, Smooth-on, USA) was chosen as the soft material for encapsulating the optical fibers. This polymer shows remarkable physical properties such as high elongation at break and high flexibility [61]. Moreover, during grasping, the silicone mediated the transmission of pressure, applied by the grasped object to the robotic finger, to the buried FBGs. Maintaining the same design of the previous Cam-Hand, new customized fingers were developed, in

aluminium, with a notch to allow the insertion of the soft material and the relative optical fibers (Figure 11B). Such groove held an irregular shape that followed the curvature of the robotic fingers. Both the side of the finger presented the groove and were connected by means of a series of holes (3.5 mm diameter) whose purpose was to hold the polymer in a fix in a fixed position. Approximately, the notch resulted 62 mm in length, 4.4 mm in width and 2.5 mm height. The liquid polymer was casted to filling the notch and thus filling out the shape of the artificial finger when not sensorized. The final design includes two optical fibers located at each side of the finger. The sensitive area of the finger is approximately 60 mm, which corresponds to the front part of the finger, namely the area responsible for the grip. Several iterations of moulds where created to realize the polymeric filling and fabrication process. This involves three consecutive steps:

i) Realization Development of the first layer of silicone with a groove to insert the optical fiber
ii) Insertion of the optical fiber in the right position
iii) Realization Development of the second layer of silicone to cover and protect the optical fiber

In step *i)* and *iii)* the silicone was degassed to minimize air bubbles and cured at room temperature until solidification.

CAM-HAND CONTROLLER

The movements of the Cam-Hand were piloted by means of a DC voltage supply (HMC804x Power Supply, Rohde & Schwarz, Munich, Germany), a relays circuit (4-channel 5V USB Relay Module, SainSmart, USA) and an optical interrogator (Hyperion si155, Micron Optics, GA, USA), that was reading the FBGs output. A Graphical User Interface was realized in LabVIEW (National Instruments, TX, USA) to control the previous units and for data acquisition (Figure 12).

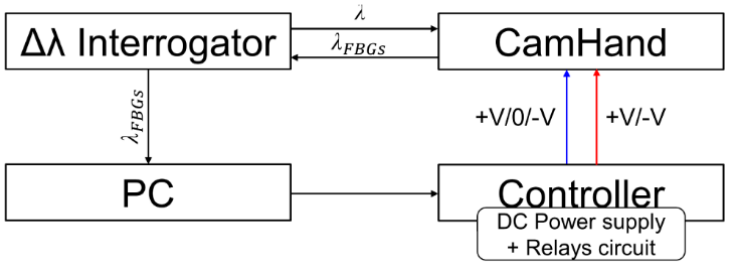

Figure 12: Block diagram of the experimental setup. The blue line shows the static controller while the red line shows the dynamic controller. λ represents the whole bandwidth of wavelengths sent through the optical fiber, λ_{FBGs} represents the reflected wavelengths of the different gratings

A positive voltage was applied to the DC motor to close the hand and vice versa a negative voltage to open it. At constant load, higher voltage values entailed higher motor speed (*rpm*) and consequentially faster movements of the fingers. Through the power supply, the voltage flow was regulated to set the velocity and the relays were switched on/off to close/stop/open (+V/0/-V) the fingers. The initial configuration, also called free configuration corresponded to a condition where the fingers were open and ready to perform the grasp, while the grasp configuration matched with the condition of the fingers closed around the objects. Two controllers were developed: *i)* static controller and *ii)* dynamic controller. In the first case a fixed voltage equal to 13.5 V was given to the motor, thus allowing the fingers to close or open at constant speed. Depending on the FBGs output and through switching the relays, the static controller achieved the action of closing, stopping and opening the fingers. Two threshold, lower and upper, were set on the mean of all FBGs wavelength variation. Enabling the static controller activated the transition from the free configuration to the grasp configuration. When the mean wavelength variation was lower than the first threshold the controller allowed the flow of a positive voltage and the corresponding closing movement. When the mean wavelength variation trespassed such threshold, due to the higher pressure applied from the object to the sensorized finger and the consequentially higher strain suffered by the optical fiber, and entered in the grasp configuration, the controller disabled the voltage flow and stopped the hand. Opening the hand, thus giving negative voltage, took place when the mean wavelength variation

raised over the upper threshold. In the second controller, instead, the given voltage was not constant but function of the mean wavelength variation. Through a PID controller (Proportional – Integrative – Derivative), in a closed loop, different values of voltage (based on the mean wavelength variation) were given in order to maintain a steady grab condition. A desirable value was established for the mean wavelength variation, corresponding to a certain grab condition, hereafter called set point, and the controller aimed at regulating the voltage values and at switching the relays on/off in order to reach this value and sequentially to maintain it. Scope of such controller was to respond, dynamically, with different voltages to changes in size of the grasped object without slipping or breaking.

EXPERIMENTAL MATERIALS AND PROTOCOLS

The performance of the proposed version of the Cam-Hand was evaluated through different tasks that involved the action of grabbing several objects in various conditions. Within this work, four tasks were performed: *i)* Size Task, *ii)* Material Task, *iii)* Fragile Task and *iv)* Dynamic Task. The first and second tasks assessed the capability of the sensorized fingers to estimate mechanical properties of grasped object, namely size and rigidity. The third task, representing a qualitative test, evaluated the ability of the system to grab fragile objects without slipping or breaking them, thus obtaining a measure of the sensitivity of the Cam-Hand. The last task measured the Cam-Hand capacity to adapt dynamically its position based on objects that could change size. For the Size Task 5 plastic cylinders, 3D printed in ABS, with varying diameter from 10 mm to 50 mm with step of 10 mm were realized. The height of such cylinders was constant and equal to 150 mm (Figure 13A). For the Material Task 4 cylinders, with 30 mm of diameter and 150 mm of height, realized in different materials were used. Such cylinders had increasing Young Modulus: Dragon Skin E ≈ 0.34 MPa, Vytaflex E ≈ 2 MPa (60A, Smooth-on, USA), ABS E ≈ 2.2 GPa and Aluminium E ≈ 70GPa (Figure 13B). For the Fragile Task commercial nachos were used, that can be considered very fragile objects (Figure 13C). The Dynamic task involved the realization of a mechanical jack composed by two concentric cylinders with, respectively, diameter of 29 mm and 23 mm and height of 40 mm and 28 mm. These objects were realized in ABS with a 3D printer and the top and bottom part were covered by a thin layer (5 mm) of Dragon Skin 20. The mechanical jack was attached to a motorized linear stage (A-LST0500B-C, Zaber

Technologies Inc., Vancouver, Canada) that could control its length by moving back and forward (Figure 13D).

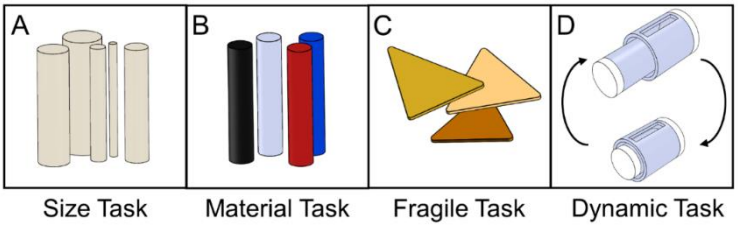

Figure 13: Representation of the used objects for the different tasks. (A) Material task: 5 ABS 3D printed cylinders with increasing diameter ranging from 10mm to 50mm with 10mm step. (B) Material task: 4 cylinders with fixed diameter of 30mm, but with different and increasing Young Modulus ranging from ≈200kPa to ≈70GPa. (C) Fragile task: Nachos used to test the sensitivity of the Cam-Hand. (D) Dynamic task: mechanical jack with variable length.

For the first three tasks the procedure consisted in performing a grasp with the Cam-Hand piloted by the static controller as follow:

i) The sample was manually held between the robotic fingers in free configuration.
ii) By enabling voltage flow, the Cam-Hand started closing its fingers until reaching the grasp configuration.
iii) After a few seconds of grasping, the robotic hand was manually released and brought back to the free configuration.

Each trial of the first two tasks was executed 10 times for repeatability, thus having 50 tests for Size Task and 40 tests for Material Task. For the Fragile Task 20 repetitions were achieved. For the first and the second task the lower threshold was set to 0.01 nm, while for the Fragile Task was set to 0.1604 nm. In the Dynamic Task a grasp of the mechanical jack was performed with the Cam-Hand piloted by the dynamic controller. The set-point was set to 0.16 nm, this value was reached after enabling voltage flow and passing from free configuration to grasp configuration. After the grasping action, random values of travel range (from -25 to 25 mm) and velocity (from 0.5 to 3 mm/s) were given to the linear motorized stage. Consequentially the mechanical jack linked to the stage started to move with different random velocity into different random position. The Cam-Hand adapted its position, with a velocity proportional to

the velocity of the stage, based on the mean wavelength variation (Figure 14). Moreover, another test was performed in which random values of travel range were given, but the values of velocity were increasing starting from 0.5 mm/s and increasing by 0.1 mm/s each 0.75 s. After reaching the destination the velocity was reinitialised to 0.5 mm/s. In order to measure the force required to break the commercial nachos, an experimental task was performed. Fifteen nachos were brought to fracture by applying a compressing force using a robotic platform composed by a load cell (Nano 43, ATI Industrial Automation, Apex, NC, USA) and a motorized vertical stage (8MVT120-25-4247, STANDA, Vilnius, Lithuania). During the experiments the motorized stage was commanded with a speed of 2.5 mm/s until breakage of the nachos samples, while the load cell was tracking the applied load force. We thus estimated the sensitivity of the FBG sensor as the ratio between the peak wavelength variation measured during grasping and the load breaking the nachos.

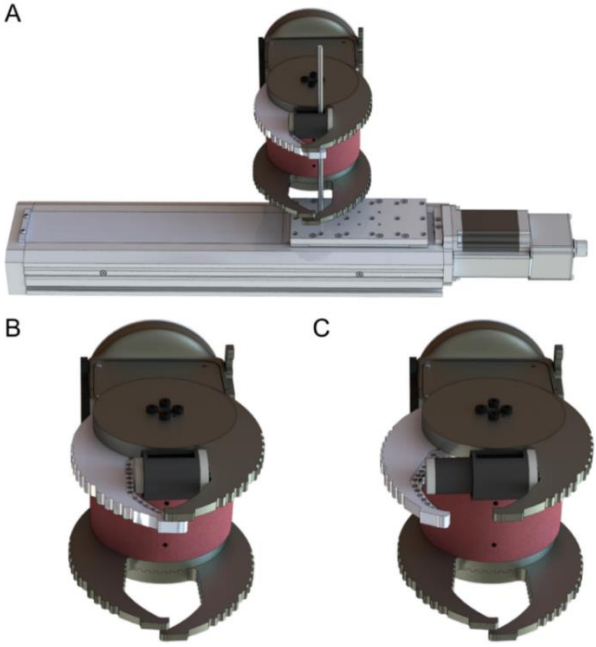

Figure 14: (A) Experimental setup for the dynamic task. (B) Cam-Hand with mechanical jack at minimum extension. (C) Cam-Hand with mechanical jack at maximum extension

DATA ANALYSIS

The Neural Network Pattern Recognition App, developed within the Neural Network Toolbox in Matlab (MathWorks, Inc., MA, USA) was employed, to predict the diameter and the rigidity, respectively in the Size Task and in the Material Task, of the grasped objects from the FBGs wavelength variation. In the Size Task The proposed classifier comprised 12 input neurons, namely all the FBGs reflected wavelength exerted during the grab, while in the Material Task there was 1 input neuron, namely the slope of the wavelength variation function of time ($\Delta\lambda/\Delta t$) tracked during the grab. Both the neural network comprised 10 hidden neurons and 1 output neuron which was the cylinder diameter value in mm in the first task and the material rigidity in the second task. The neural networks were trained using conjugate gradient backpropagation method. The experimental data were divided in three complementary subsets: *i)* training set, *ii)* validation set and *iii)* testing set. For each class (*i.e.,* diameter) 10 repetitions were performed and 8 trials were used for training, 1 trial for validation and 1 trial for test. To reduce variability multiple rounds of cross-validation, using different partitions, were performed. The "Leave-one-out cross-validation" method was adopted, that used one observation as test set (and one as validation set) and the remaining as training set. Such partition was repeated, each time changing the test set and consequentially the other two subsets, until all the 10 trials were considered one time as test set. The results of the different cross-validation were combined (*i.e.,* averaged) to assess the neural networks predictive performance by means of a confusion matrix. For the Material Task, we were interested in tracking the temporal wavelength variation among all the different materials. Within the Fragile Task the ability of the Cam-Hand to deal with fragile objects was assessed, by calculating the number of broken samples during grasps. To assess the performance of the Cam-Hand to follow the changes in the grasped objects (Dynamic Task). The Root Mean Square Error (RMSE), the Normalized RMSE (NRMSE) and the NMRSE calculated for the data included in the interquartile range ($NRMSE_{(IQR)}$) were calculated as expressed in Equation 4-6.

$$RMSE = \sqrt{\frac{\sum_{n=1}^{N} \left(x_{1,n} - x_{2,n}\right)^2}{N}} \quad (4)$$

$$NRMSE = RMSE / \bar{x} \quad (5)$$

$$NRMSE_{(IQR)} = RMSE_{(IQR)} / \bar{x}_{(IQR)} \quad (6)$$

1.2.3 Results & Discussion

Through different tasks the capability of the proposed FBGs-based robotic hand to provide tactile feedback was assessed. By evaluating the performance of the proposed classifier for size recognition of different grasped objects, an overall accuracy of 99.36% was achieved. Individual accuracy values were calculated for each diameter: 99.3% for 10 mm, 99.4% for 20 mm, 99.6% for 30 mm, 98.5% for 40 mm and 99.9% for 50 mm. Moreover, it is relevant to observe that misclassification, within the different classes, happened mainly with their relative neighbours (Figure 15).

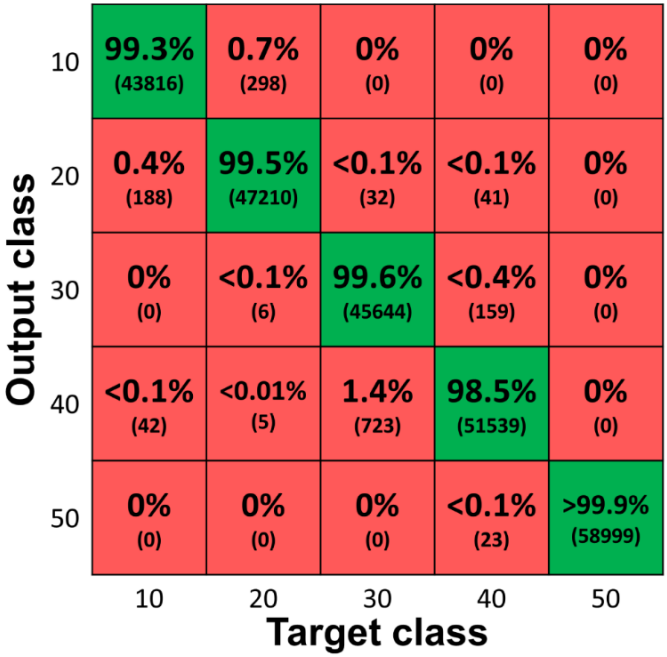

Figure 15: Confusion matrix showing the accuracy (99.36%) of a classifier for size discrimination of the grabbed sample. 5 cylinders with different size were tested. 10 trials were performed per each sample. 8 out of 10 trials were used for training, 1 out of 10 for validation and 1 out of 10 for testing. To improve generalization we applied the «leave one out cross validation» method. The numbers in brackets represent the experimental data processed by the classifier.

Physical properties of grasped objects strongly affected the FBGs wavelength variation. The slope of the wavelength variation function of time (Δλ/Δt) increased monotonically with increasing Young Modulus across the different materials (Figure 16A). High repeatability was achieved across all trials: the median value of the slope was 0.87 ± 0.02 nm/s for Dragon Skin 20, 1.61 ± 0.04 nm/s for Vytaflex, 2.48 ± 0.05 nm/s for ABS and 3.54 ± 0.12 nm/s for Aluminium (Figure 16).

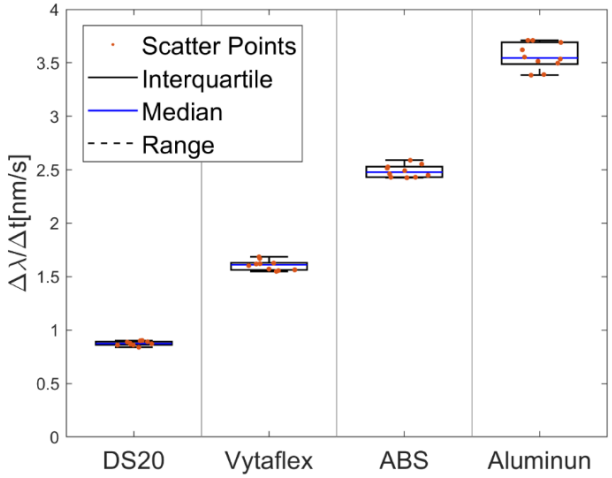

Figure 16: Box plot of the FBGs Δλ/Δt (slope of the signal) for the different materials. From left to right the Young Modulus is increasing. Boxes represent interquartile ranges; blue lines show the median value and black dashed lines show the complete range across samples.

Furthermore, the classifier used to predict the rigidity showed an accuracy of 100% for all the classes Within the Fragile Task, when performing a grasp on the nachos, only one sample among the 20 executed trials was broken (Figure 17).

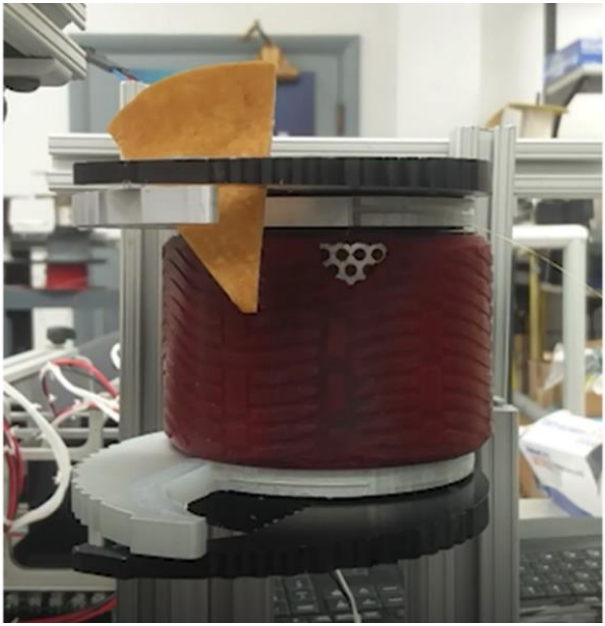

Figure 17: Picture showing the fragile test performed by grasping a commercial nachos.

The results of the Dynamic Task presented similar performances in the two experimental conditions, both in the experiments with constant velocity (Figure 18) and in those where velocity increased from one position to the next (Figure 19). Error values were: RMSE = 0.019 nm, NRMSE = 12% and NMRSE(IQR) = 1.2% for the first condition and RMSE = 0.014 nm, NMRSE = 9% and NMRSE(IQR) = 2.2% for the second condition. The mean force value needed to break the sample was experimentally estimated to be 9.49 N ± 3.13 N. Combining this result with the FBG wavelength variations recorded in the fragile task turns out in a sensitivity estimation of at least 139 pm/N.

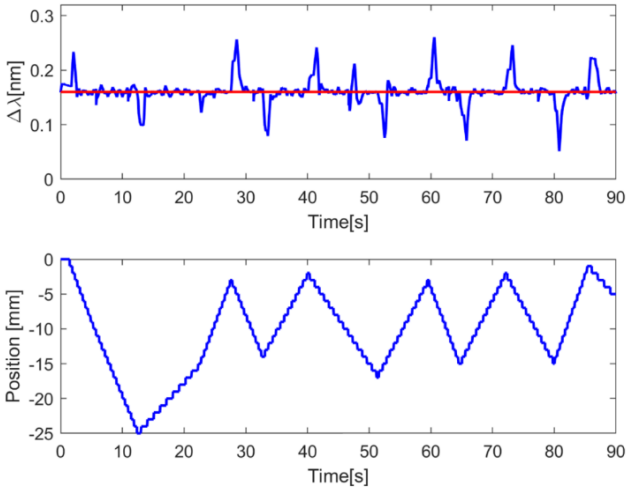

Figure 18: Graph showing the dynamic task results. In the upper plot, the red line represents the set point value equal to 0.16 nm, the blue line represents the process variable, namely the wavelength variation of the mean of the FBGs. In the bottom plot the blue line represents the position of the motorized translational stage.

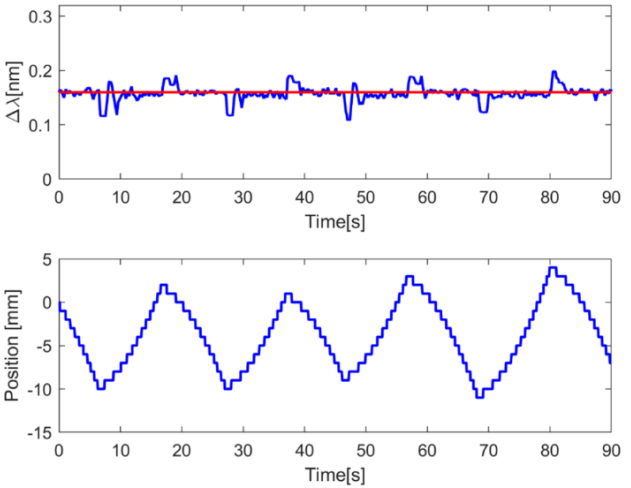

Figure 19: Graph showing the dynamic task results. In the upper plot, the red line represents the set point value equal to 0.16 nm, the blue line represents the process variable, namely the wavelength variation of the mean of the FBGs. In the bottom plot the blue line represents the position of the motorized translational stage.

The results obtained through the different tasks turned out in very high precision in identifying relevant properties of grasped objects (Size Task, Material Task and Fragile Task) as well as the contact conditions (Dynamic Task). Within the Size Task the sensorized hand allowed recognizing the diameters of the cylinders from Bragg wavelength variations, using the proposed neural network for pattern recognition (99.36% accuracy). Since the trials of the Material Task were performed using the static controller, thus selecting a constant velocity for fingers movements, such condition also allowed estimating the hardness of the different materials via the temporal variation of the Bragg wavelength (100% accuracy using the proposed classifier). Our hypothesis relied on the evidence that, at constant speed, harder material involved faster Bragg wavelength signal variation. Within the Fragile task, from observation made on several grabbed samples (nachos) the reliability of the sensorized finger was evaluated in handling such kind of fragile objects. The achieved experimental results are quite generalized, since each nacho had a different shape and size. The scope of the task was to understand qualitatively the sensitivity of the sensor. The results of the Dynamic Task provided evidence of the capability of the sensorized finger to adapt its position based on the variation of the length of a mechanical jack. Furthermore, it is clear that in both the performed conditions and during the entire travel range the difference between the set point and the process variable was very low as demonstrated from the $NRMSE_{(IQR)}$ values. However, the results presented some peaks related to the phase of inversion of the motion of the stage as highlighted from the NRMSE values, which were based on the entire raw dataset and not only the interquartile range. When the stage reached a position, it moved immediately into another position and therefore direction. Consequentially, the robotic finger passed from the action of closing to the action of opening (or vice versa) that caused an error of the controller in maintaining constant grasp conditions. Although the PID controller was not always accurate, the maximum and minimum values of wavelength variation were acceptable for keeping a good grasp without breaking or slipping the object. We believe that the peaks encountered in the task are not related on the sensor performance but on the used motor drivers (relays circuit). The scope of the work was mainly centred around the evaluation of the proposed tactile

sensorization and not in the realization of a perfect controller. Furthermore, the mechanical jack linked to the motorized stage through a long steel bar could have influenced the presented results. Future work will address the integration of the sensorized Cam-Hand in a robotic arm, thus bypassing the issues of the controller, since the actuation part will be managed by the motor controllers of the arm. Moreover, next investigations will carry out experimental tasks with either other shapes (not only cylinders) but will also evaluate wider ranges of diameters and rigidity to increase the variety of the grasped samples. Besides, next studies will deal with the calibration of the system in order to estimate the relationship between the wavelength variation and the applied pressure to the robotic finger. A limitation of the present study is related to temperature compensation ability. FBGs directly respond to strain and temperature changes. Such intrinsic sensitivity to both physical variables require a compensation method in order to split the contribution due to mechanical actions from the one due to possible temperature changes. Considering that the environmental conditions of the laboratory were stable within the performed experiments, the temperature contribution was not considered. Future studies will aim at introducing temperature compensation solutions, for example by means of dummy FBGs being not affected by strain but by temperature changes only.

The present work introduced a robotic hand sensorized with optical fibers, embedding FBGs transducers, to convey tactile feedback in robotic manipulative tasks. To the best of our knowledge this is the first study that demonstrates the application of FBG technology in a robotic hand in order to achieve fine object manipulation and features extraction based on closed-loop control. The choice to sensorize such a gripper with optical fibers is based on their flexibility in the integration process, but also on their high sensitivity in strain measurements. Thanks to this integration of tactile sensors, the new Cam-Hand design targeted the following abilities: *i)* estimation of the grasped object size, *ii)* detection of a value related to the Young modulus of the grasped objects *iii)* grasping of objects with different mechanical properties (*i.e.* fragile, deformable, stiff) without their slippage or breakage, and *iv)* dynamic adaptation of the fingers in order to maintain constant the wavelength variation, independently from the shape of the objects. We believe that the multiple advantages of FBG technology can move forward the current state of the art. Beyond the aforementioned advantages, optical fibers

ensure light weight solutions and distributed sensor capabilities. Another interesting advantage of using such a technology is the multiplexing capability. Multiple FBGs can be housed along one single optical fiber by means of just minor arrangements, hence improving the sensing capabilities without drawbacks in terms of complexity and bulkiness. Finally, FBGs pave the way for RoboSimian to operate in those application scenarios that require electromagnetic immunity, where most of the conventional sensors are unsuitable.

1.3 Design and Development of Large-Area FBG-Based Sensing Skin for Collaborative Robotics[3]

1.3.1 Framework

During the last decades, the interest in the field of robotics and the development of related technologies have led to a closer and closer cooperation between men and machines. A new generation of robots has been introduced to help humans in performing several tasks, ranging from industrial production, transportation, and delivery of goods, up to medical assistance and rehabilitation. As robots and humans move towards sharing the same environment, is expected that equipping them with a tactile sensory experience would increase their intelligence, permitting to establish safe and collaborative human-robot interactions, even in an unfamiliar scenario, [97]. A harmless behaviour and interplay with the real world intimately depend on the availability of some form of tactile feedback, [25], since this is the sensory modality enabling humans to explore object properties, develop body awareness and interact with the surrounding environment through contact and manipulation. Since Lumelsky's first elucidation about the development of a robotic sense of touch, [16], [97], a variety of tactile systems, suitable for mimicking the activity of both low (*i.e.,* large-area skin) and high (*i.e.,* fingertips) sensor density human body sites, have been proposed, by exploring different approaches and transduction principles. The integration of force and torque transducers inside the mechanical structure of robotic solutions has represented one of the first attempts aiming at gathering information by preventing a direct contact between sensors and external objects, [15]. By seeking to embed the outer surface of robots with tactile sensors, prototypes of large-area integrated skins have been introduced. A robust, low-cost, low-noise capacitive force sensing array is reported in, [57]. Each sensing element of this system is a three-plate capacitive sensor equipped with a multi-vibrator circuit having a pulse train output, inspired to human mechanoreceptors. Such a design allows minimizing stray capacitance and noise coupling, as well as a robust signal

[3] This section has been excerpted from the paper, [282], that has been published in an international conference: 2019 IEEE International Workshop on Metrology for Industry 4.0 and IoT, with the PhD candidate being co-author of the study.

transmission in noisy electrical environments. A force transduction capacitive system has been proposed by Hoshi et al., [67]. The "Skin by Touch Area Receptor," or STAR, is a high-density element array, in which each sensor is linked through communication chips, to avoid long wires encumbrance. Another design of integrated skin has been investigated by Ohmura et al., [25], consisting of a 32-element light-weight, conformable and scalable skin based on optical mode of transduction. The so-called "cut-and-paste" tactile sensor consists of a photo-reflector covered by urethane foam. The light scattered by this foam upon deformation gives a measure of the intensity of the applied force. A highly compliant artificial skin, capable of simultaneously detecting multi-axis strains and contact pressures has been introduced by Park et al., [98]. This system consists of an elastomer matrix hosting multi-layered micro-channels filled with a conductive liquid. "HEX-O-SKIN" is the attempt made by Mittendorfer et al., [99]. The basic transducer of this tactile system consists of a hexagonal PCB holding an electronic board to pre-process data and deliver information, and a bunch of custom and off-the-shelf sensors (e.g., proximity, pressure, vibration, and temperature). HEX-O-SKIN can be modularly disposed to create a skin-like coverage on a robot backbone.

In recent years, the interest in fiber optic-based sensors (FOSs) has gained momentum especially for applications in robotics and medicine, [43], [100]–[102], being a viable alternative to traditional sensors to investigate several mechanical and thermal parameters, [96], [103]. In particular, the use of FBG-based technology for force measurement adds remarkable advantages to those solely offered by the FOSs, [2], [104], such as immunity to drifts, linear and additive response to both strain and temperature, and inherent self-referencing capability. Furthermore, FBGs allow reducing cabling requirements and issues about installation: by taking advantage of the intrinsic capability of the FBG transduction principle, [35], a wavelength-separated array able to simultaneously read a large number of outputs from the same fiber has been the choice that best fitted the proposed system design. In, [96] two different designs for FBG-based tactile systems have been presented for both low and high spatial resolution applications, respectively. The 3x3 array mimicking human body skin consists of a diaphragm type transducer, that is deformed by an external force. When this force concentrates on the contact mesa of the transducer, the membrane is deflected

and determines an elongation of the embedded FBG sensor with a subsequent shift of its output (*i.e.,* Bragg wavelength). Like human insensitive skin, this transducer is able to sense a maximum force range of 5 N, with a spatial resolution of about 20 mm. The sensing array mimicking the skin of a finger consists of 9 transducers resembling a bridge, being arranged along three optical fibers. This array shows a spatial resolution better than the previous one (5 mm), due to a shorter length of Bragg gratings. Both systems show a non-linear calibration curve. However, developing an effective and efficient application of an artificial skin in the form of a large-area highly distributed tactile sensor system, instead of a high-density sensor matrix, is still an open challenge, [103]. In this work, the design and development of a polymeric FBG-based artificial sensing skin, mimicking the human sense of touch in perceiving pressure, and its integration on a custom human-like robotic forearm is presented (Figure 20). A preliminary assessment of the tactile sensor system performance has been performed to evaluate the sensitivity, in terms of the relationship between the applied load and the occurred shift of the gratings Bragg wavelengths.

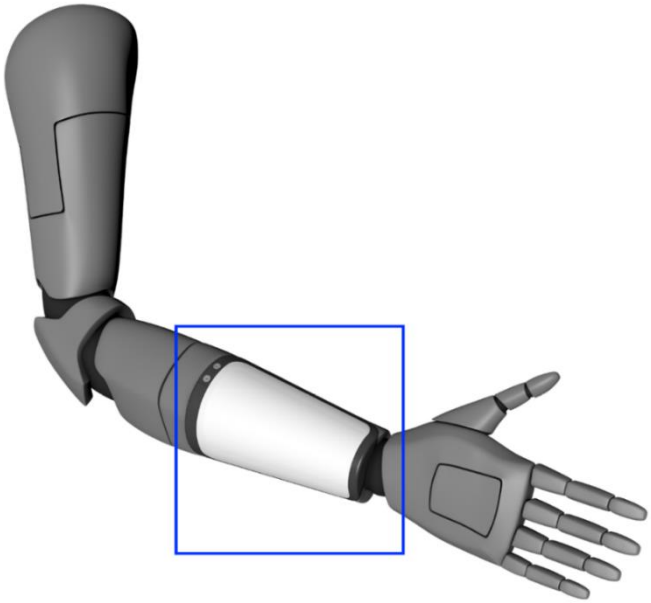

Figure 20: Large-Area FBG-based sensing skin on a human-like robotic forearm

1.3.2 Materials & Methods

We designed and developed a polymeric large-area artificial skin integrating optical sensors to enable the perception of external force in a 3D-printed human-like forearm of a robotic manipulator. Specifically, we followed the requirements and expectations concerning the realization of a tactile sensing system for a robotic sense touch proposed in, [97], also taking into account the features of human touch, [2], [104]. The system consists of an 8 mm thick polymeric layer (Dragon Skin 10 Medium; Smooth-on Inc, PA, USA) equipped with an 80 µm in diameter and 430 mm in length engineered optical fiber (FEMTOPlus Grating; FemtoFiberTec GmbH, Berlin, Germany). Such optical fibers were chosen since small diameters allowed low bending radius configurations. The silicone rubber allowed the fabrication of a thin, light-weight and flexible substrate, that offered compensating features, such as the capability to stretch or wrinkle, preserving both the integrity of wires and sensors and the stability of the coverage. In comparison with previous works, [105], the novelty of the proposed silicone coating lies in its shape. Specifically, such a coating offers a curved surface (15500 mm^2 in area), that allows covering three-dimensional objects and prevents the embedded sensors from any pre-strain. The polymeric frame is endowed with 16 FBGs of 4 mm in length, whose centre-to-centre distances and Bragg wavelengths (λ_B) are spatially distributed. We customized the sensor distribution along the fiber core in order to achieve a varying spatial FBGs density, matching density of human mechanoreceptors across the forearm skin (i.e., decreasing when moving from elbow to wrist, [3], [66]).

EXPERIMENTAL SET-UP

To assess the capability of the developed artificial skin in perceiving the applied loads in terms of position and intensity, a mechatronic platform was employed (Figure 21). This platform consisted of a 4 degree of freedom system of motorized stages: a Cartesian manipulator made of a precision vertical (Z) positioner (8MVT120-25-4247, STANDA, Vilnius, Lithuania) and X-Y stages (8MTF-102LS05), which guaranteed translational movements, while a rotator (8MR190-2) enabled 360° degrees rotations. The apparatus provided force measurement thanks to a 6-axis miniaturized load cell (Nano-43, ATI Industrial Automation, Apex, USA). Specifically, the load cell acted as a single axis sensor to perform the experiments in force-

control mode of the platform along the loading direction of the skin (z-axis). A customized probe, mechanically linked to the force sensor, was used to exert indentations across the skin outer surface. Such a tool was composed by an aluminium cylinder of 15 mm in length and 13 mm in diameter, equipped with an aluminium sphere of 6.5 mm in radius at the tip level, to mimic the size of a human fingertip. FBGs required an interrogation unit able to illuminate the gratings with a broad spectrum, and detect the reflected wavelength. (SmartScan, Smart Fibres Ltd, United Kingdom). An ad-hoc Graphical User Interface (GUI) was developed in LabVIEW (National Instruments, TX, USA) to control the instrumentation of the setup and enable both data gathering and recording.

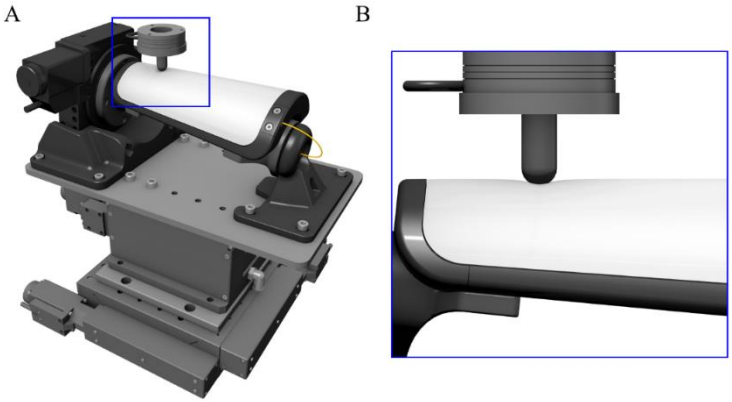

Figure 21: Experimental setup. A) Mechatronic platform for force-controlled indentation. B) Inset of the indentation onto the polymeric matrix

Experimental protocol and Data analysis

The relationship between the applied force (F_Z) and the resulting wavelength shift ($\Delta\lambda$) of each sensor ($k = \Delta\lambda/F_Z$) was evaluated by exerting a 3 N vertical load above each grating, according to the FBGs positions along the optical fiber, by means of the mechatronic platform. During the experimental session, data about the exerted force, its point of application and the readout of the entire FBG array were recorded at a sampling rate of 500 Hz and offline processed through an in-built routine in MATLAB (MathWorks, Natick, USA) in order to compute the mean value of the sensitivity.

1.3.3 Results

The correspondence between the applied force and the wavelength variation of a strained FBG is shown in Figure 22. This graph is an example of the output signal arising during the loading phase on the centre of the FBG sensor. The sensitivity evaluated for each grating is reported in Figure 23. As shown, the median value across the FBGs is 0.26 nm·N^{-1}, while the interquartile range is 0.08 nm·N^{-1}.

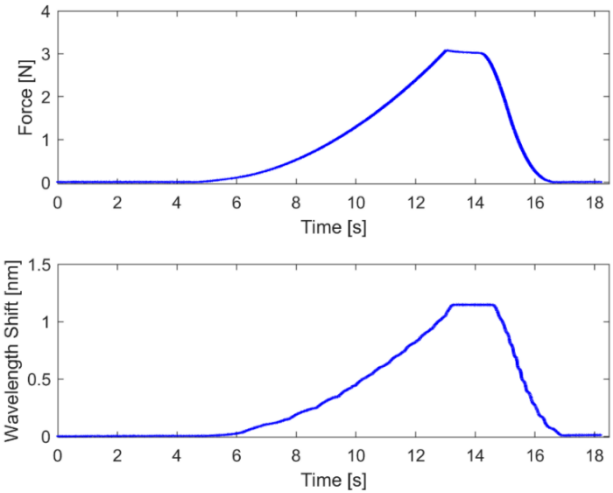

Figure 22: Example of recorded data during an indentation above one of the embedded FBGs. The upper plot shows the exerted force as a function of time; the bottom plot shows the corresponding wavelength shift of the strained FBG.

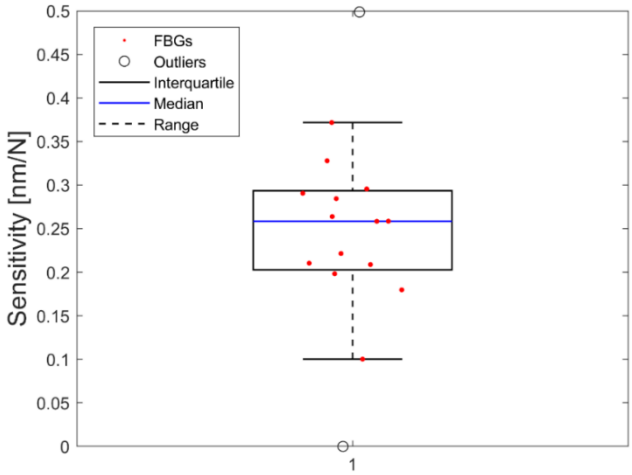

Figure 23: Box plot of the sensitivity. The blue line represents the median value; the bottom and top edges of the box indicate the interquartile range; whiskers represent the whole dataset (excluding outliers); black circles represent outliers values; red scatter points represent the sensitivity across the FBGs.

CONCLUSIONS

In this paper, the design and development of a novel large-area distributed tactile sensor system, in the form of a polymeric FBG-based sensing skin, are presented. A mechanical characterization has been performed to assess the performance of the system in perceiving pressure. Results show that the skin enables repeatable force measurements with a median value of 0.26 $nm \cdot N^{-1}$ in sensitivity. From this exploratory analysis it is also evident the effect of the polymeric encapsulation on the FBGs response. In literature, no FBG-based sensing skins have been yet developed to equip human-shaped robotic arms with a tactile sensory experience. We choose to sensorize the artificial skin with optical fiber sensing systems due to the multiple advantages offered, such as: i) high spatial sensitivity, ii) flexibility in the integration process, and iii) multiplexing capabilities that limit the wire encumbrance. Moreover, with respect to previous studies, we have added an element of novelty by fabricating a curved polymeric frame to house the optical fiber. Future works will involve a deeper analysis regarding the performance of the present artificial skin in terms of spatial

sensitivity and force range, towards the final goal of integrating the tactile sensor onto a robotic arm.

2 Tactile Sensing Through Mechatronic Platform for Medical Applications

2.1 A biomechatronic platform for detection of nodules in anatomopathological analyses via force and ultrasound measurements[4]

2.1.1 Framework

Cancer is an abnormal and uncontrolled cell growth that invades healthy tissues, and that can spread via metastases to other locations in the body, [106]. Various cancer treatments involve chemical and radiation therapies or surgery, [107]–[109]. Following surgical intervention, biopsy is performed on the lymph nodes excised from the tissue to properly characterize cancer spread and examine whether it has developed the ability to spread to other lymph nodules or organs too. The accuracy in estimating the amount of spread of cancer is extremely important to avoid complications caused by an extensive resection of healthy lymph nodes and tissues. Accurate localization of tumours in tissues resected during surgery can also allow the surgeon to decide and modify unanticipated the planned intervention so to remove malignant tissues missed in pre-operative imaging and planning. Stiffness of human tissue is higher for tumour nodules with respect to healthy tissues, [110]–[115]. Hence, inspecting the mechanical properties of cancerous tissues can contribute to the detection of nodules. Intraoperative palpations of the resected malignant tissue provide essential information about the presence of abnormalities, [116]. Indeed, such investigation is part of the general practice performed by a specialist through manual palpation to retrieve several information about cancer nodules, [117]. The reliable confidence of medical practitioners to detect tumour is achieved with rigorous training before they reach proper expertise in examining various organs and detecting abnormalities, [118]. The human capability to detect lumps in the tissues, however, degrades with increasing lump depth, decreased compliance of the tissue, deformation of the finger pad induced by the lump itself, and

[4] This section has been excerpted from the paper, [283], that is under review in an international scientific journal, with the PhD candidate being first author of the study. A preprint of the submitted paper is available online: Link

the finger indentation velocity, [119], [120]. Ultrasound analysis, [121], can complement stiffness data because of the different acoustic properties of cancer nodules, as demonstrated by intraoperative ultrasonography recordings having reported influence (varying from 2.7% up to 73%) on the surgical procedures that were preoperatively planned, [122]–[125]. In this study, we combined stiffness and ultrasound data to aid the intraoperative histological exams performed on tissues excised during surgery. Such an examination is crucially essential in case of misdiagnosis or unforeseeable diagnostic queries that arise during surgery. Results from the examination may be used as a guide for surgical resection and decision-making to modify the surgical procedure (Figure 24).

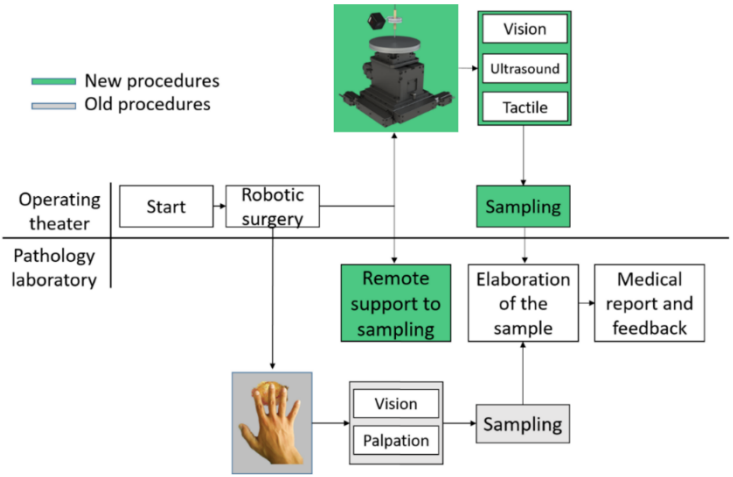

Figure 24:Block diagram of the histological procedure. Grey: traditional manual procedure. Green: semi-automatic procedure as modified by the introduction of the developed platform.

With instrumented tools, automatic classification of tumours in tissues can be addressed by machine learning techniques: supervised-unsupervised classification, clustering and learnt neural networks, [126], [127]. The proposed system aims at reproducing the activity of anatomopathologists in intra-operative tumour identification using feedback from vision, stiffness, [128], and ultrasound measurements, [129]. Using a robotic platform and machine learning techniques for classification, the focus of this work is to detect and localize nodules buried in phantoms mimicking the

elastic and ultrasound properties of excised human tissues. Specifically, the experimental evaluation was carried out by means of Agar-based phantoms that can be fabricated to mimic the liver, cardiac, brain and soft tissues, [130]–[132], either in their acoustic and mechanical properties and temperature dependency, [133], [134]. This study is organized as follows: Section 2.1.2 describes the experimental setup, the technical specifications of the used phantoms, the experimental protocol and data analysis methods. Results are presented in Section 2.2.3, showing data analyses based on stiffness and ultrasound measures separately, as well as by merging the two measurement systems. The last part of Section 2.2.3 concludes with the discussion of the entire work and presents potential future investigations.

2.1.2 Materials & Methods

PLATFORM DESIGN

A platform was developed to detect embedded rigid inclusions surrounded by a soft matrix. The automated system consists of the following components (Figure 25):

i) Three motorized translational stages and one rotational stage allowing to move the sample. A commercial stage (8MTF-102LS05, STANDA, Vilnius, Lithuania) with 10 cm of travel range and a resolution of 2.5 µm was used for the X and Y axes, while another translational stage (8MVT120-25-4247) was used to indent the sample along the Z axis, having a travel range of 2.5 cm and a resolution of 5 µm. Additionally, a fourth stage was mounted on the mechatronic platform (8MR190-2-28) in order to enable the rotation of the sample. Such stage had 360° rotation range with 0.01° resolution.

ii) An ultrasound probe (Sonomed 16 MHz mod. 2014059, Warsaw, Poland), with fractional bandwidth equal to 0.25 at -6 dB, used in pulse-echo mode. This needle-type probe, 3 mm in diameter, was selected also for directly contacting and indenting the sample. A 30 Vpp pulsed excitation was delivered to the probe via a transmitter (US-Key, Lecoeur-Electronique, Chuelles, France) connected to a PC via USB2. The experimental setup was completed with the ultrasound data acquisition device, NI FlexRIO (National

Instruments Corp., Austin, TX, USA), for acquisitions at high frequency (1.6 GHz).

iii) A load cell (Nano 43, ATI Industrial Automation, Apex, NC, USA) to collect interaction forces, up to 18N with 0.004N resolution along normal axis, arising at the interface between the ultrasound probe and the sample, also used in the control loop of the translation stages in order to operate force-controlled indentations. The developed software used this force data to calculate the stiffness and to trigger the high frequency US imaging at the threshold point of contact (0.2 N).

iv) A waterproof HD-camera (Hero5 Session, GoPro, San Mateo, California, U.S.) with 10 MP and 4K resolution, integrated to perform the sample shape recognition and to create a matrix of points to be indented.

v) A stainless-steel disk fixed on the top of the motorized stages for the positioning of the sample, but also to permit the reflection of the ultrasound signal back to the probe. The disk had 16 cm diameter and 1 cm thickness.

The software routines for controlling the platform and the automatic scan of the samples, data acquisition, and the graphical user interfaces were developed in LabVIEW, LabVIEW Real-Time and LabVIEW FPGA (National Instruments Corp., Austin, TX, USA), while the data analysis were performed using MATLAB (The MathWorks, Inc., Natick, Massachusetts, United States).

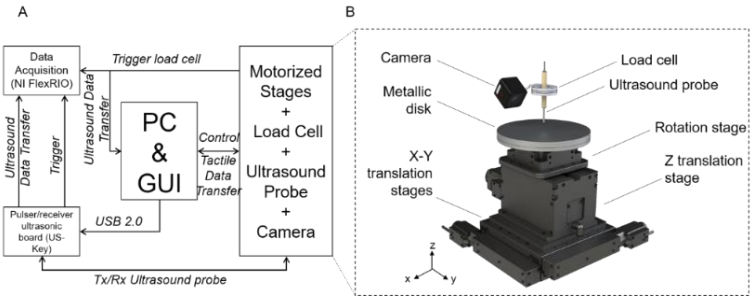

Figure 25: A. Block diagram of the experimental setup. B. Experimental setup showing the different components.

PHANTOM OF HEALTHY TISSUE AND INCLUSIONS

Tests were performed on four Agar block-shaped phantoms, realized to mimic both the mechanical and the acoustic properties of diseased human tissues. Each phantom had a soft surrounding matrix to represent human healthy tissues and hard inclusions embedded inside to represent tumour nodules. Each fabricated phantom was nominally 60 mm wide, 100 mm long and 15 mm thick, while the buried spherical inclusions had different diameters ranging from 3 mm to 12 mm. The volume of the phantom was large enough to introduce up to 8 inclusions, 2 per each diameter, in different X-Y positions with adequate separation distance (Figure 26) in order to execute computer-aided detection trials.

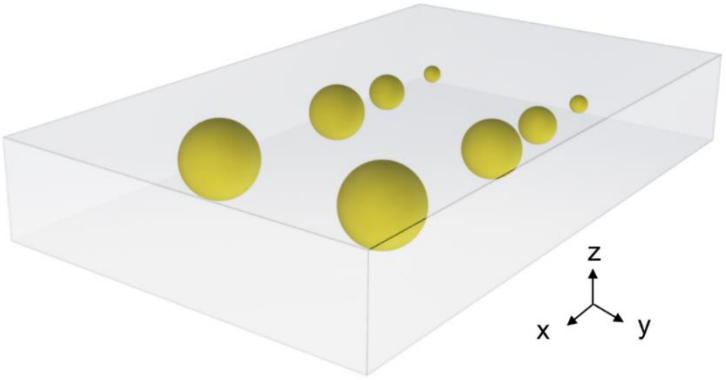

Figure 26: Rendering of the Agar phantom used during the experimental acquisition. The spherical inclusions are marked in yellow (Ø 12-9-6-3 mm). Dimensions of the phantom are 100x60x15 mm^3.

Agar-based phantoms were prepared using a predefined concentration of Agar in distilled water. Changing the concentration of Agar resulted in a variation of both the mechanical and acoustic properties. A concentration of 2 g of Agar in 100 ml of water was used to represent a healthy human tissue (fabricating a phantom entirely with this concentration results in 1.59 MRayl acoustic impedance, 1457 m/s speed of sound and 0.33 N/mm mechanical impedance). A concentration of 8 g of Agar in 100 ml of water was used for simulating a tumour tissue (fabricating a phantom entirely with this concentration results in 1.92 MRayl acoustic impedance, 1534 m/s speed of sound and 4.6 N/mm mechanical impedance).

EXPERIMENTAL PROTOCOL

The experimental protocol consisted in an automatic scan of the sample. The procedure was divided in two steps:

i) visual analysis;
ii) stiffness and ultrasound analysis.

The purpose of the visual analysis was to recognize the shape of the sample by acquiring its boundaries and to create the indentation matrix, namely the points to be analysed. Such analysis is crucial when dealing with real tissues, where the shape and size is unknown or irregular, so that the scan can be defined automatically. The visual part (Figure 27) consisted in subtracting the background image from the sample image, thus obtaining the shape, the size and the orientation. Starting from this new image (Figure 27C), a set of indentation points was created with a 2 mm step along the X-Y axes.

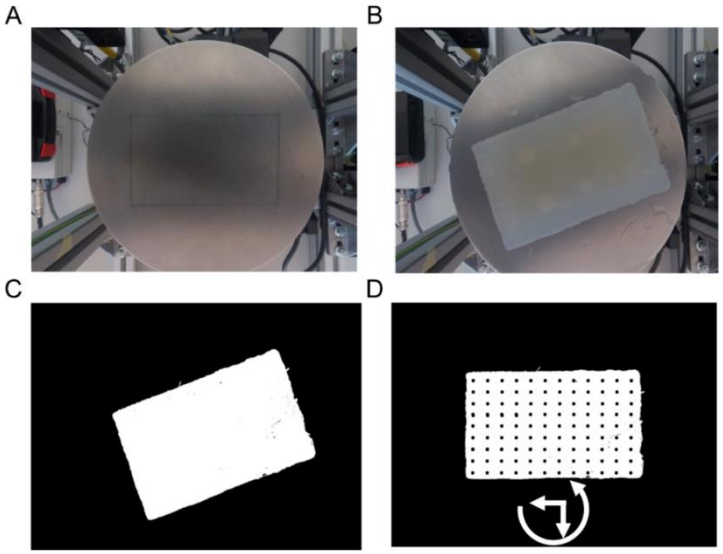

Figure 27: Visual part: positioning of the sample, boundary detection and creation of the indentation matrix. A. Background. B. Sample in its original position. C. Boundary detection. D. Positioning, rotation and creation of the indentation matrix.

Once the visual analysis was completed, it was possible to start the acquisition of force and ultrasound data. Per each X-Y point of the indentation matrix, the phantom was indented along the Z axis at

constant speed (0.5 mm/s). The compression force was recorded and at a low threshold (0.2 N, to avoid damaging the tissues) a trigger signal was generated for ultrasonic pulse transmission and to record the reflected signal (Figure 28).

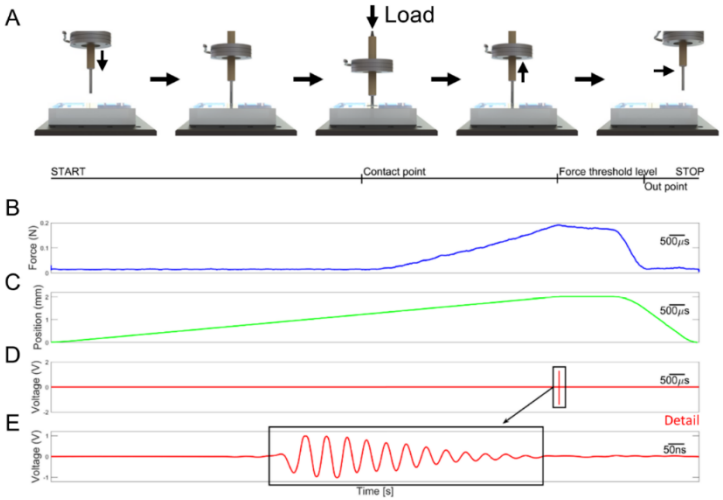

Figure 28: A. Experimental protocol involving indentation of an ultrasound probe at regulated contact force. B. Normal force. C. Z position. D. Ultrasound signal reflected from the steel metal plate. E. Zoom of ultrasonic scan shown in D.

Data analysis

The detection and localization of the different inclusions was were based on the elaboration of indentation force (FZ), vertical position (Z) and ultrasound data. The stiffness k for each indentation was calculated according to Equation (7).

$$k = (\Delta F_Z) / \Delta Z \qquad (7)$$

The ultrasound technique used for the detection of the inclusions was based on the reflectometric method that varied the reflection signal for tissue-like matrix and inclusions. In practice here, we considered more reliable to work with the variation of the signal reflected from the reference steel plate, interfaced with the bottom of the phantom, at the interface with the reference steel plate to be more reliable rather than processing considering the very low-amplitude signal reflected from the inclusion (the reflection coefficient was less than 1%). The ultrasonic analysis consisted in

processing the signal reflected in each point, using the Correlation Index Amplitude (CIA) parameter, [135], defined in Equation (8).

$$CIA = 1 - \left(\frac{min\left(\sqrt{\sum S_{ref}^2}, \sqrt{\sum S_i^2} \right)}{max\left(\sqrt{\sum S_{ref}^2}, \sqrt{\sum S_i^2} \right)} \right) \quad (8)$$

In this equation S_i and S_{ref} denote the signal acquired in each point and the reference signal, respectively. The reference signal was acquired in a position outside the inclusions but inside the tissue-like matrix. The CIA assumed values between 0 and 1 and a high CIA indicates the detection of an inclusion as the two signals become poorly correlated. Per each indented point, a colour map was created both for stiffness and correlation index amplitude. An unsupervised classifier, called Fuzzy C-mean (FCM) clustering, was used to classify each indentation of the scan on the phantom. Such unsupervised classification system, starting from the elaborated data, enabled the diversification categorization of the point and the subsequently organization into different clusters. In this way, it was possible to divide the data into: *(a)* tumour prediction class, which were the sites classified as inclusions, and *(b)* healthy prediction class, which were the sites classified as non-inclusions. From the wrong classification prediction points, we obtained the number of false positive number, *i.e.,* soft matrix points classified as inclusions, and the false negative number, *i.e.,* inclusions classified as soft matrix. Furthermore, new datasets results were obtained and classified by merging the stiffness and the ultrasound data using AND-OR logics. In the AND case, we considered tumour only the points identified as inclusion in both the datasets simultaneously, thus we expected an increase in the total number of false negatives. In the OR case, we considered tumour all the points classified as inclusion in either the stiffness dataset or the ultrasound dataset, thus we expected an increase of the number of false positives and reduced false negatives, as it is crucial to include all of the cancerous tissue even with a larger healthy parts. Through a confusion matrix, the accuracy and the misclassification rate were calculated for all the datasets and methods

2.1.3 Results & Discussion

All the experimental results presented in this paragraph have been repeated over 4 replicas of the developed phantoms.

RESULTS FROM STIFFNESS MEASUREMENTS

An example elaboration of the stiffness analysis for one of the 4 phantoms is shown in the top parts of Figure 29. The bottom part of Figure 29A shows the positions of the inclusions inside the indentation matrix. Since the inclusions were embedded in a soft matrix, their stiffness was depending not only on the materials properties, but also on the dimensions of the buried inclusions. The stiffness values indeed increased with the dimension of the inclusions. Stiffness analysis was clearly capable to detect the bigger inclusions, namely 12 mm and 9 mm. Figure 29B, showing the results for the whole indentation matrix, confirmed this trend. A visual inspection of the image allows discriminating big inclusions compared to the soft surrounding matrix.

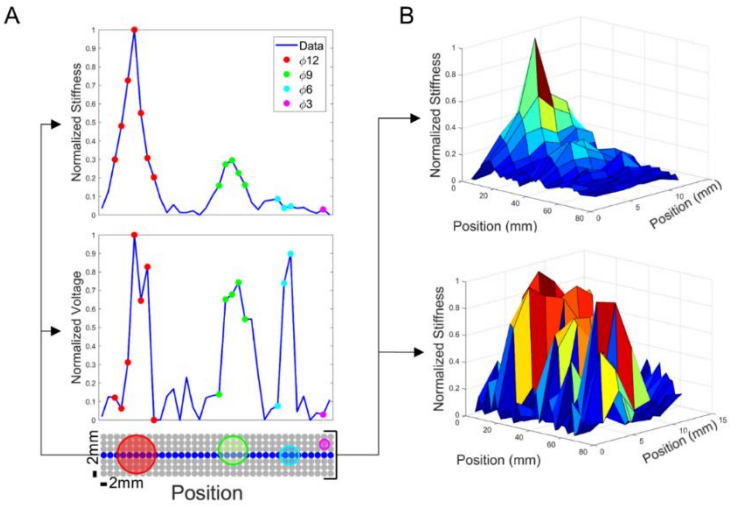

Figure 29: A. (Top) Graph showing stiffness as a function of position, calculated as ΔFz/ΔZ, for the central row. (Bottom) Graph showing ultrasound signal processing (CIA). B. (Top) 3D graph showing stiffness across the whole indentation matrix. (Bottom) 3D graph showing ultrasound signal processing (CIA).

The results of the identification based on stiffness measures are shown in Figure 30A, as a result of the Fuzzy C-mean (FCM) clustering. The results of this unsupervised classification system confirmed the ability of the stiffness measurement system to recognize all the points belonging to the big inclusions, thus without false negatives. Such performances were evident from the high number of true positive (green points) for 12 mm and 9 mm inclusions. However,

stiffness analysis was not able to reliably identify the smallest inclusions, as pointed out by the high number of false negatives (red points) for 6 mm and 3 mm inclusions (Figure 30A).

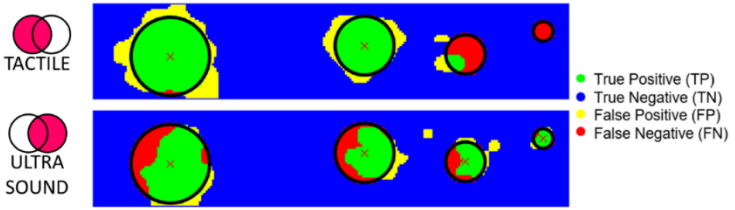

Figure 30: Classification (TP-TN-FP-FN) of all the points of the indentation matrix for the analyses with stiffness (A) and ultrasound (B) measurements.

Results from ultrasound measurements

Ultrasound data analysis is shown in Figure 29 (bottom part). In Figure 29A, the intensity of the CIA signal is shown to increase consistently above the inclusions. But, unlike the stiffness measurements, higher CIA values were observed also for the smaller inclusions. Thanks to the high CIA peak recorded for each inclusion, this approach led to detecting all the inclusions buried in the phantom (Figure 29B), showing the results for the whole indentation matrix confirmed this trend. As for the stiffness measurement part, Figure 30B shows the results of the FCM clustering, highlighting the ability of the ultrasound system to systematically detect the inclusions. This trend is visible in Figure 30B where there are true positives (in green) in each of the inclusion. Remarkably, false positives (in yellow) and false negatives (in red) were obtained in the area at the boundary between the inclusion and the soft matrix, confirming high specificity in identifying the sites to focus on for histological analyses.

AND-OR logics to merge stiffness and ultrasound measurements

New datasets were obtained and classified by merging stiffness and ultrasound measurements using AND-OR logics. Figure 31 shows the results for both the combinations. The AND logics (Figure 31A) turned out in an increase of false negatives and decrease of false positives. The growth of false negative predictions can lead to the worst-case scenario, since might mean loss of identified tumours. Instead, the OR logics demonstrated to be a safer approach since it turned out in an acceptable increase of false positives and a very good decrease of

false negatives. As shown in Figure 31B, the OR logics between stiffness and ultrasound measurements was able to correctly discriminate all the inclusions, even the smaller ones. Such results were achieved thanks to the complementarity of the two systems. The stiffness analysis was better in localizing bigger inclusions, whereas the ultrasound analysis was better for smaller ones (compare Figure 30A and Figure 30B).

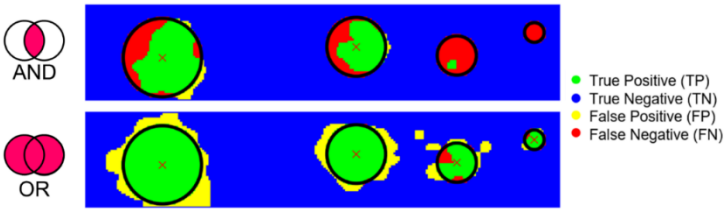

Figure 31: Classification (TP-TN-FP-FN) for all the points of the indentation matrix following the AND-OR logics of stiffness- and ultrasound-based classifications shown in Figure 7.

This is further confirmed by looking at the confusion matrices obtained with the 4 experimented phantoms and with all the identification techniques, *i.e.,* based on just stiffness measurements, just ultrasound, and with the AND-OR logics (Figure 32)

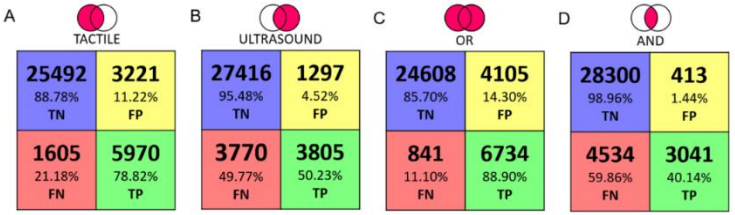

Figure 32: A. Confusion Matrix with classification based on stiffness measurements. B. Confusion matrix with ultrasound measurements. C. Confusion Matrix with classification based on inclusions as recognized by stiffness OR ultrasound measurements. D. Confusion Matrix with classification based on inclusions as recognized by stiffness AND ultrasound measurements.

Discussions

In this work we presented a platform for identification of cancer nodules in ex-vivo tissues. Such tool, oriented towards automation of diagnostic procedures during surgery has the scope to increase the effectiveness of histopathological evaluations. Such exams need to

be performed as correctly as possible because the report may lead in a modification of the surgical procedure. The human capability to detect these lumps depends on the physician expertise and tactile capabilities. The presented platform combines three different measurements, such as camera vision, stiffness calculations via force-position sensing and ultrasound recordings to perform an automatic scan and evaluation of the indented tissue. In this work, the tests were performed in laboratory environment using 4 Agar phantoms that mimicked the mechanical and acoustic properties of human ex-vivo tissues. The phantoms integrated 8 spherical inclusions with different diameters (3 mm up to 12 mm) to reproduce tumors inside healthy tissues. The results, summarized in the confusion matrices, demonstrated the ability of the platform to automatically identify the inclusions, particularly when complementing stiffness with ultrasound measurements via OR logics. In particular, as reported in the confusion matrix, the tactile presents valuable classification results in detecting the inclusions as reflected from the 78.82% of TP and 88.78% of TN. Moreover, it shows a low percentage of FP and FN, 11.22% and 21.18% respectively. We observe that the tactile analysis provides satisfactory shape recognition and tumor detection for inclusions up to 6 mm in diameter. On the other hand, it missed the smaller inclusions that are buried deeper into the softer matrix. The ultrasound can be a very good guiding tool for localization and detection of tumors, including the smaller ones, because the amplitude of reflected signals from the surface of the inclusions remains independent of the size. The ultrasound data presents high amount of TN of 95.48% and a low FP of 4.52%. However, the ultrasound alone shows limitations that are reflected in high number of FN of 49.77%. To improve the performance, the classified datasets were logically merged using the OR and AND. As expected, the results of OR logic gave evidence of higher rate of inclusion recognition, 88.90% of TP and 85.70% TN, maintaining low error rates, 11.10% FN and 14.30% FP. Interestingly, the AND logic localizes the bigger inclusions with increased TN of 98.96% and reduced the FP to 1.44%, but the TP of 40.14% and FN of 59.86% misses the correct shape and smaller tumors entirely. Moreover, we found that the ultrasound is also sensitive to the air bubbles formed in the agar inclusions and detects early reflections from the surface of the these bubbles. Tactile data, however, covers these air bubbles inside the inclusion,

giving the true shape of the inclusion in the OR logic. Within the present work, we adopted a scan resolution inspired by the probe diameter (3 mm). To keep a balance between the scan speed and area, we decided to scan with step of 2 mm. Lesser resolution values (*i.e.,* 3 mm) lead to insufficient data points in the scanned area, while higher values (*i.e.,* 1 mm) would introduce unaffordable scan time and oversampling. The phantoms are the simplistic versions of the biological tissues, hence, further developments will address the experimentation of the robotic platform on ex-vivo human tissues in clinical environment. In the future, when placed in the operating theatre, the developed system will enable the anatomopathologist to access data remotely with the purpose to assist the surgeon in adapting the procedures during surgery. Information obtained from the platform can also be used to provide haptic feedback to the anatomopathologist by means of wearable interfaces, [11], [12], [136]. The analysis of vision data, now used only for detecting the boundary of the tissue and thus to define the indentation matrix, will be improved to provide a visual report too. Such a new procedure will target the extraction of several features from the pictures of both healthy and tumorous tissues to learn their differences via artificial intelligence methods and thus complement stiffness and ultrasound measurements. Moreover, the results will be translated in an electronic report and integrated with the management software (*e.g.,* HL7) of the healthcare system. It is our opinion that the presented robotic platform is able to obtain and replicate the perfomance also with *ex-vivo* tissues. We foresee our device in a real operating condition (*i.e.,* anatomopathological laboratory). Such considerations are supported by preliminary studies performed on animal ex-vivo tissues. Further studies will deal with deeper examination on such samples.

2.2 A Neuromorphic Model to Match the Spiking Activity of Merkel Mechanoreceptors with Biomimetic Tactile Sensors for Bioengineering Applications[5]

2.2.1 Introduction

The objective of reproducing the dynamics of the human somatosensory system is typically pursued for two main bioengineering applications: neuroprosthetics and neurorobotics. Regarding the neuroprosthetics field, users of current artificial hand prostheses report the complete absence of sensory feedback as a relevant drawback of those systems, [137], [138]. Tactile feedback restoration would then lead to an improved capability of manipulation, and possibly to a better embodiment of the prosthesis; such restoration could be possible thanks to a signal closely mimicking the physiological way in which the tactile peripheral system encodes information. In the neurorobotics field, the interest in mimicking tactile systems lies on the idea of building models which reproduce the advantageous features of natural sensory systems, as the reduction of the computational cost, [139]. The developed artefacts, in turn, can be integrated for use in application domains such as surgical, industrial or field robotics, as well as used to test scientific hypotheses, [140], [141]. In order to mimic touch perception, the capability to reproduce mechanoreceptors dynamics is necessary. Mechanoreceptors are subcutaneous cells deputed to the detection of mechanical interaction with the skin: those sensory receptors respond to mechanical stimuli, as pressure and vibration, and convert them into an electrical signal that is conveyed to the central nervous system through afferent pathways. Mechanoreceptors are characterized by the type of stimulation the receptors respond to, the size of their receptive field and their rate of adaptation. Here we will focus on Merkel nerve endings, labelled as Slowing-Adapting type 1 (SA1), [104]. SA1 units detect sustained pressure, low frequency stimulations and precisely localized spatial deformation. The objective of this study is to define a function which

[5] This section has been excerpted from the paper, [284], that has been published in an international scientific journal: IEEE Transactions on Medical Robotics and Bionics, with the PhD candidate being co-author of the study.

allows the matching between the activation of an artificial spiking neuron and the sustained firing characteristics of Merkel mechanoreceptors. In particular, we proposed a function with few parameters to tune. It works with the raw sensor signal, without additional online processing, such as differentiation and filtering of the collected signals. Following such approach, the real-world input space can be mapped properly into a set of artificial neuron outputs, mimicking the naturalistic encoding of sensory stimuli via spikes patterns that can be injected into the human nervous system. When a transducer is integrated upstream of the sensory chain, the designed block in the neuromorphic tactile system receives the sensor measured-estimate as input and conveys this signal as modulating input signal into the Izhikevich model, [142], known for being able to emulate a wide range of neuronal dynamics when its parameters are properly tuned; the output then can be relayed either to a human neural interface or to a neuro-robotic system. In order to emulate the sustained firing of Merkel receptors, in this work we refer to the seminal study by Knibestöl and colleagues that systematically described the receptors properties, [143]. Models attempting to reproduce human mechanoreceptors firing are on the rise and the recent state of the art includes several works. Arleo's group implemented a leaky integrate-and-fire model with threshold fatigue for braille stimulation encoding, [144], [145]. Our group used the Izhikevich model to encode surface properties, [146] and to categorize naturalistic stimuli, [147], and demonstrated applications in both neuroprosthetics, [86] and neurophysiology, [148]. The Izhikevich neuronal model was also used by Thakor's group with the aim to emulate the spiking activity of human mechanoreceptors, [149]. Recently, the Izhikevich model was used to reproduce the dynamics of regular spiking and fast spiking mechanoreceptors in order to elicit the sensory perception of touch and pain in amputees; the neuron voltage was computed according to the signal coming from the sensorized fingertip of a robotic arm prosthesis, [150]. Yi and Zhang mimicked the response of Fast Adapting type I mechanoreceptors with piezoelectric sensors elicited by sinusoidal stimuli; not knowing the relation between external stimuli and the corresponding mechanoreceptor currents, they adopted a simplified mechanotransduction model based on two parameters: intercept constant and gain, [151]. The generated continuous analogue electric signal was converted in spike trains by an Integrate-and-Fire neuron

model. The average inter-spike interval and the first spike latency were compared with the response at the same set of stimuli of macaque monkeys, obtaining a reasonable matching. Our approach aims at preserving the computational simplicity pursued by Yi and Zhang, while still relying on experimental observations. In a series of studies, Bensmaia and colleagues, [152]–[156] ,accurately reproduced the temporal dynamics of different kind of mechanoreceptors by proposing a transfer function between the time evolution of the pressure and its derivatives, and the input to different kinds of integrate-and-fire neurons. To this aim, they found model parameters, tested on a set of combinations of periodic functions, that predicted the timing of individual spikes in response to novel stimuli. In their latest work, they compared the model responses with the measured ones when the same stimulus is applied, showing a level of precision of the order of *ms*. This model was compared by Valle and colleagues with nerve stimulation techniques based on amplitude modulation, to restore sensory feedback and assess the stimulation performance in real-life grasping tasks, [157]. They found that a hybrid strategy, accounting for biomimetic frequency and amplitude modulation, improved manual dexterity and prosthesis embodiment. In a real scenario, the prosthesis control board should include the motors control, sensors reading and processing, user intention decoding algorithms and models for sensory feedback. Therefore, it is important that each module is computationally efficient to meet the control requirements. To this aim, the model we propose is lean, computationally very light, and not requiring derivatives of sensor data. The parameters of the proposed model are openly available to be easily reproducible by third parts. In comparison to some of previous works, [152], [154]–[156], in this study we focus specifically on emulating the spiking activity of a single class of mechanoreceptors (SA1) during sustained stimulation. In this study, we introduce and characterize a general porting function block (Figure 33) to be tuned to properly convert the sensor output to the input current to the artificial neuron.

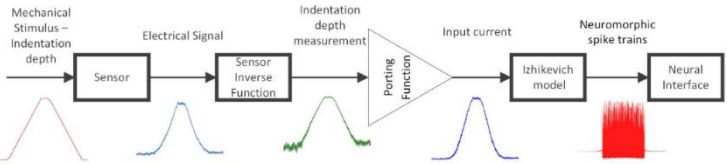

Figure 33: Schematic representation of the implemented mechano-neuro transduction. Block diagram describing the different steps of the transduction from mechanical stimulus to neuromorphic spike trains, with samples of signal evolution. From left to right: the electrical signal generated by the mechanical stimulus in the sensor is used to reconstruct the stimulus indentation by means of a tailored calibration inverse function. The indentation is converted into a virtual current by means of a suited porting function (see Results). The virtual current is finally injected in the Izhikevich model to generate the neuromorphic spike trains mimicking the firing activity of Merkel mechanoreceptors.

This tuning operation aims at ensuring that the output of the Izhikevich model emulates the sustained firing behavior of natural human mechanoreceptors. Thus, the block proposed in this study can be intended as a generalized interface to tactile sensors. For this reason, having modelled the proposed block directly from the applied indentation depth, a calibration inverse function is needed to get back the measurand value from a given transducer output, which has the form of an electrical signal. Doing so, the calibration inverse function serves as a conditioning block in order to perform this conversion prior to application of the proposed model.

2.2.2 Materials & Methods

Implemented Izhikevich artificial neuron model

In the Izhikevich model, the membrane potential v and the adaptation variable u are updated according to the following nonlinear differential equations (9-11):

$$\dot{v} = Av^2 + Bv + C - u + \frac{I_{input}}{C_m} \tag{9}$$

$$\dot{u} = a(bv - u) \tag{10}$$

$$if\ v \geq 30\ mV\ , then \begin{cases} v \leftarrow c \\ u \leftarrow u + d \end{cases} \tag{11}$$

Table 3: Parameters for the implemented regular spiking artificial neuron model

A	B	C
$0.04\ \frac{1}{mVms}$	$5\ \frac{1}{ms}$	$140\ \frac{mV}{ms}$

a	b	c	d
$0.02\ \frac{1}{ms}$	0.2	$65\ mV$	$8\ mV$

In this study, the model is discretized by means of a custom MATLABTM (Natick USA) script implementing the Euler's method with 100 µs integration time. Each simulated recording lasted 1000 ms, during which the signal was converted into temporal sequences of spikes. The regular spiking dynamics is used in this work as evidences have been provided about its reliability to encode tactile information during tasks involving sustained indentation phases, [86], [147]. The model parameters to achieve regular spiking behavior are shown in Table 3.

This kind of neuron model generates a single spike at the onset of the stimulation (Figure 34A) for input currents up to 3.75 nA (Figure 34B). Beyond this threshold point, the neuron is able to generate a sustained activity (Figure 34A) with a monotonous increase in the firing rate (FR), defined as the number of spikes over the simulation time (Figure 34B). We tested input currents ranging from 2.60 to 30.00 nA with a 0.05 nA step. This range was chosen as it allows observing the threshold crossing and results in physiological FR values.

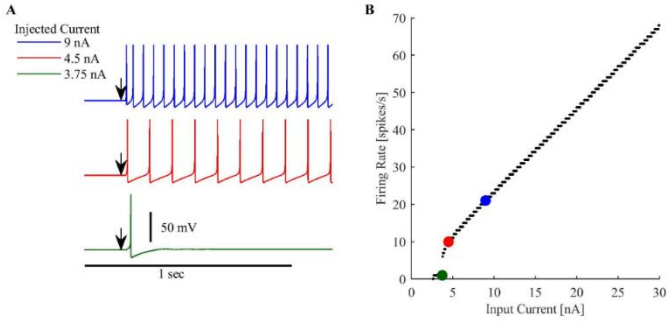

Figure 34: Artificial neuron dynamics. (A) Neuron membrane potential corresponding to three different input currents, i.e. 3.75 nA, 4.5 nA and 9 nA, supplied to the Izhikevich model (the current onset is shown by the arrows). The neuron membrane potential is measured in mV. (B) Firing Rate for input current ranging from 2.60 nA to 30.00 nA for the Izhikevich Neuron Model. Coloured dots represent the FR corresponding to the three current levels depicted in the left panel.

Spiking model benchmarking methods

The firing dynamics of Merkel receptors was characterized in several previous neurophysiological studies, [3]. In particular Knibestöl, [143], analysed the responses to application of sustained indentation stimuli for one second, reporting neural features that can be directly compared with the artificial neuron FR proposed in this study. Briefly, in the neurophysiological investigation that we selected as a benchmarking reference, recordings were acquired percutaneously via microneurography from 101 mechanoreceptor afferents from human median and ulnar nerves; mechanical stimuli were delivered with a 1 mm^2 tip probe attached to a moving coil controlled by a waveform generator. Stimuli were driven by supplying the coil with rectangular pulses of 1 s fixed duration at indentation depths ranging from 0.5 to 4 mm, therefore undergoing a variation of indentation of 3.5 mm. In the aforementioned study by Knibestöl, [143], two different measures were used to evaluate the neural response: the total number of nerve impulses evoked during the stimulus application, [158], and the mean impulse frequency of the sustained discharge during the last 0.5 s of the stimulus. Here, to compare the biological neuron to the artificial model we considered the former measure. The resulting average FR ranged between 1 and 35 spikes/s. The FR values used in this study were extracted directly from the figures in , [143], where a total of 16 samples is available. Then, an analytical relationship between the indentation stimulus applied to

the skin and the biological FR has been obtained based on the point measures. Although in many studies the stimulus-response relationship for cutaneous mechanoreceptors has been described by a simple power function, [158]–[160], we looked for a sigmoid-shaped fitting in the form suggested by Knibestöl, [143] with the addition of an offset term:

$$I = o + \frac{R_m \cdot (x - \alpha)^{\gamma}}{(x - \alpha)^{\gamma} + \beta} \tag{12}$$

where o is an offset (vertical displacement of the function), R_m is an amplitude coefficient, α is a horizontal displacement of the function, γ determines the slope and the speed of convergence to the horizontal asymptote and β determines the position of the inflection point. The coefficients were determined by using the fit MATLABTM function. This allows, in the present work, to have a generalized function that is used to provide a larger set of biological data samples for benchmarking purposes. We used the sigmoid fit and the input-FR relationship computed in Figure 34B to estimate the relationship between the applied indentation and the input current to be injected into the neuron model (Figure 35).

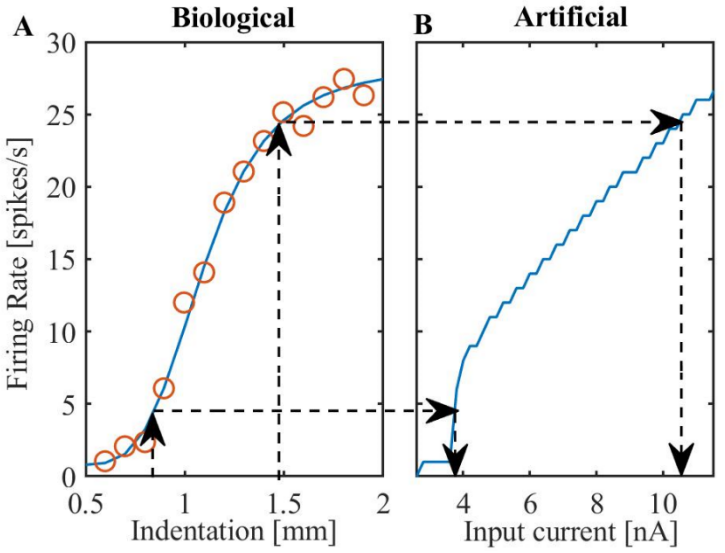

Figure 35: Comparison of biological neuron and artificial neuron dynamics. (A) Circles represent experimental firing rates associated to different indentations collected in the study by Knibestöl, and the continuous blue line shows a sigmoid fit. (B) Given two

example indentations, the procedure for finding the corresponding input current, looking for the FR value of the sigmoid fitting and then passing it to the artificial neuron dynamics is shown.

For this purpose, we evaluated the performance of a set of six functions (1st to 5th order polynomial and sigmoid) in capturing such relationship and adapted the input to the Izhikevich neuron model, so to achieve an output firing that reproduced the benchmark biological characteristics:

(i) Polynomial porting functions:

$$I = \sum_{i=0}^{i=n} w_i x^i \tag{13}$$

with 1≤n≤5;

(ii) Sigmoid porting function

$$I = o + \frac{R_m \cdot (x-\alpha)^6}{(x-\alpha)^6 + \beta} \tag{14}$$

where *I* is the Izhikevich input current and *x* is the variation of indentation. The goodness of fit was evaluated by computing the adjusted residual variance ($Adj\sigma_{res}^2$), defined as the complementary of the adjusted determination coefficient, [161], [162]:

$$Adj\sigma_{res}^2 = 1 - AdjR^2 = \frac{\sum_i^N (\hat{y}_i - y_i)^2}{\sum_i^N (y_i - \bar{y})^2} \cdot \frac{N-1}{N-m} \tag{15}$$

The function with lower $Adj\sigma_{res}^2$ is used to generate the input current leading to the spiking train sequences for each indentation experimental sequence.

EXPERIMENTAL EVALUATION WITH BIOMIMETIC TACTILE SENSOR

To assess the feasibility of the proposed framework, an experimental application was implemented as a final step of the study. In these experiments, an aluminum probe mounted on a mechatronic indentation platform was used to stimulate a biomimetic fingertip with an array of sixteen pressure sensors (2x2 array of four MEMS).

Using biomimetic tactile platforms, aimed at mimicking the mechanical behavior of real fingertips, to build models of the biological skin-receptor complexes, is a widespread method, [163]–

Table 4: Parameters for fitting biological data

R_m	α	β	γ	o
$27.54\ nA$	$0.42\ mm$	$0.21\ mm^4$	4	$0.79\ nA$

[165]. The biomimetic fingertip we used is the hybrid silicon tri-axial force sensing platform described in, [166], [167]. Its polymeric packaging was designed to reproduce the skin response to stimulation, [168]. This device was used in the past years to replicate tactile features such as roughness encoding, [169], naturalistic textures discrimination, [147], and to restore such abilities in amputees, [4]. The probe had a surface of 1 mm^2 and was indented at 5 mm/s along the direction orthogonal to the finger (Figure 36) in order to emulate the experimental conditions described by Knibestöl, [143].

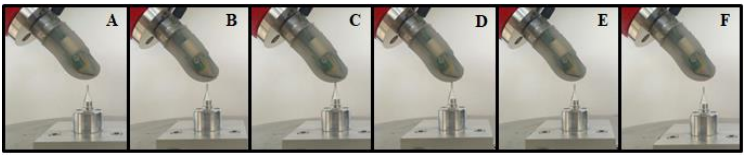

Figure 36: Biomimetic tactile sensor platform. It is composed of an aluminium probe rising to indent the artificial finger. (A) No-contact position. (B) Rising phase. (C) Indentation Phase. (D) 1 second of sustained indentation. (E) Unloading phase. (F) Return to the initial position.

The probe started the indentation from a no-contact position defined as the minimum distance from the finger at which the output sensor voltage did not significantly change. The mechatronic platform was controlled and data were recorded with custom LabVIEW™ (Austin, USA) routines. Experiments were conducted with different protocols: trapezoidal and triangular waves of stimulation, with incremental amplitudes, were applied to the artificial finger by controlling the probe indentation depth. 'Trapezoidal wave' means that, between loading and unloading phase, the finger was held in position for one second, in order to achieve a sustained stimulation. The null-load phase was held for one second before starting with the next

stimulation. 'Triangular wave' means that the loading phase was immediately followed by the unloading phase. The probe started from a non-contact position and was pushed incrementally against the finger, adding 75 µm each repetition to the indentation depth, until reaching 0.75 mm indentation (hence, 10 indentation depths were experimented). This cycle was repeated 5 times. We tested the applicability of our model (Figure 33) as follows. For the calibration of our sensor we used voltage and position values from the triangular wave stimulation experiment: starting from the acquired data, we computed the sensor inverse calibration function. Then the output voltage of the other experiment was used for evaluating the whole model chain (Figure 33). Every sensing channel was linked to one artificial neuron. Among the sixteen channels of the finger, voltage readings from sensor number fifteen were used: this sensor was chosen because it was the one that displayed the highest voltage variation during the experimental protocol since it had the probe fully within its receptive field (this experimental condition resembling the characterization of the so called 'hot spot' of mechanoreceptors in neurophysiology). We removed the offset of the voltage signal measuring the sensor output baseline before the experiments. The inverse calibration function of the sensor was obtained by fitting the relationship between voltage signal variation and indentation depth with a second order polynomial function. We tested the calibration function with the validation dataset obtained via the trapezoidal wave protocol, comparing the final spiking response to its sustained one-second-long plateau of stimulation to Knibestöl's experimental recordings. The indentation tested with the artificial finger had a total range of 0.75 mm. FR values obtained with this experiment were compared with the physiological ones, shown in the left panel of Figure 35. Since the experiment comprised five repetitions of trapezoidal waves, the mean FR among consistent indentation levels in different trials was considered, along with the FR standard deviation.

2.2.3 Results & Discussion

PORTING FUNCTION COMPUTATION

In order to have a broader set of comparison data, we interpolated the biological experimental data, [143], with a sigmoid function, whose parameters are shown in Table 4. In this way, starting from 16 samples, a set of 151 coordinates was obtained to describe the input

current to the artificial neuron model. Figure 37A shows how such current, when injected into the artificial neuron model as a function of the applied indentation, generates the same firing rate obtained in biological data. To derive the analytical approximation of this relationship a set of six functions (Eq. 13 and 14) were tested to fit the data points (Figure 37A) The fitted parameters are shown in Figure 37B.

As we aim for a lean analytic function, we compared the fitting quality with $Adj\sigma^2_{res}$, penalizing higher order fits (see Material and Methods). We observed that, although $Adj\sigma^2_{res}$ penalized higher order fits, a linear fit led to a high $Adj\sigma^2_{res}$ of 0.0522 (Figure 37B).

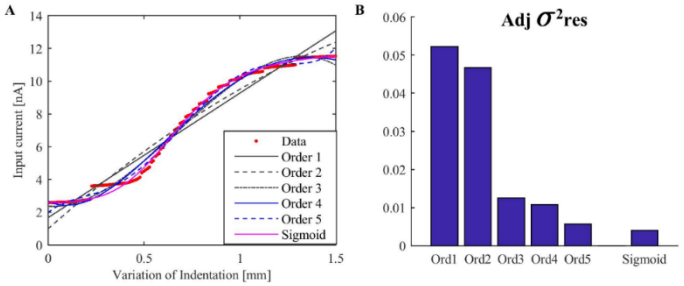

Figure 37: Input current to the Izhikevich neuron model as a function of indentation. (A) Red dots indicate biological data approximation as resulting from the procedure described in Figure 3. The lines superimposed to the data correspond to the different fits tested: 1st to 5th order polynomial and sigmoid functions. (B) Adjusted residual variance of the experimental data fits performed with the functions displayed in panel A.

A third-order fit showed instead an important drop in $Adj\sigma^2_{res}$ to 0.0125, thus appearing to be a proper compromise between error reduction and model complexity. The best $Adj\sigma^2_{res}$ value was obtained for the sigmoid fitting (0.0040); fifth order fitting was also tested to evaluate the outcome with an additional parameter, but led to a greater $Adj\sigma^2_{res}$ value (0.0057), so that, even if with a slight difference, the sigmoid function displayed the best fitting quality (Figure 37B). The spiking train sequences obtained for three indentation samples is depicted in Figure 38.

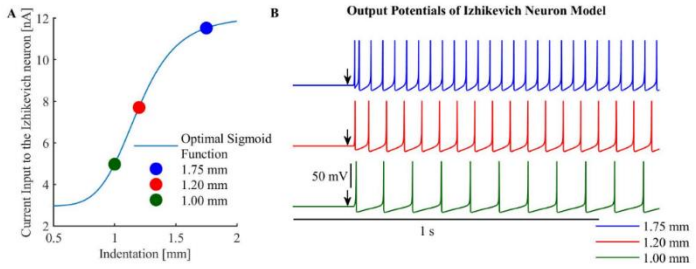

Figure 38: Spike patterns associated to indentation depths. (A) Sigmoid function described in equation (8) (light blue line), associating indentation depths to input currents to the artificial neuron model. Circle markers indicate values for three example stimuli. (B) Membrane potentials of the implemented SA1 artificial mechanoreceptor model, in correspondence to the three input currents associated to the different indentation depths marked in panel (A).

Evaluation of the complete chain of SA1 artificial spiking mechanoreceptor model

The sensor inverse calibration function was computed by data coming from the triangular wave experiments, and the obtained function was able to fit the data with a RMSE of 26 µm by employing a second order polynomial fitting (Figure 39A). The average FR obtained from the artificial finger data via the complete chain of SA1 artificial spiking mechanoreceptor model (Figure 33) reliably reproduced the physiological FR values that had been characterized by Knibestöl with the same indentation depths considered in the present study, achieving a FR RMSE of 1.98 ± 0.21 spikes/s (Figure 39B).

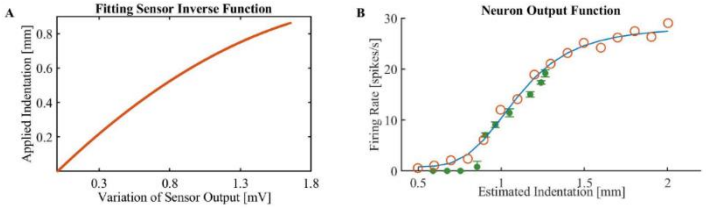

Figure 39: Validation on the proposed SA1 artificial mechanoreceptor model by means of experimental data with a biomimetic tactile sensor. (A) Sensor inverse calibration function, to estimate the applied indentation from the output voltage of the sensor. (B) Firing rate during one second of stimulation for different variations of indentation depth. Red circles are experimental data from Knibestöl fitted with the blue line. Green dots are average FR computed with experimental data from the biomimetic tactile sensor. Green bars indicate ± standard deviation.

DISCUSSION

This study describes a middleware between physical sensors used in bioengineering applications and SA1 mechanoreceptor neuronal models producing spiking outputs. The method was validated by experimenting a sensorized biomimetic finger indented with a 1 mm^2 probe that could apply controlled indentation depths. The output of the artificial neuron achieved good resemblance to the one of human nerves and therefore is deemed applicable to an in vivo implant. Specifically, we defined a function describing the relationship between the sensed indentation depth and the virtual current that should be injected to an Izhikevich Regular Spiking neuron model to make its output consistent with the firing response of a biological SA1 receptor. In order to compare the proposed architecture with human physiological output, we relied on data available on neurophysiological literature, [143]. Our method has been proven to constitute a mean for interfacing the nervous system with the real physical extent of the stimulation, regardless of the type of sensor and nature of the transducer used for collecting the stimulus. Different functions have been tested in fitting our model with data deriving from biological recordings. The linear fit is the simplest one and that with the worst performance. The sigmoid fit is among the most complex ones, but it ensures the best error results. The third order fit is a good compromise between complexity and goodness-of-fit. With respect to similar previous works, [151]–[156], we note that in the study by Saal and colleagues, the authors compared the timing of the spiking train with the one recorded on monkeys, achieving precision up to ms, [156] and the authors stated that the model was computationally efficient enough so that a simplified version of the model could be employed in real time applications. In this perspective, we point out that the model developed in this work is already lean enough to be employed online, since it relies on the Izhikevich model that had already been used in real time by our group with human subjects having peripheral neural implants, [86]. According to the proposed implementation, a calibration of the tactile sensory system is necessary before its usage. Indeed, any given sensor will output an electrical signal that is linked via a function to the real value of the measurand, according to the characteristics of that sensor. A reliable quantitative estimation of the received stimulus is then necessary to achieve the desired neuron dynamics by means of the proposed model: by applying the

calibration inverse function of the sensor to the sensor electrical output, an estimate of the measurand is obtained. The novelty of this study lies in the generalization of the method for feeding any given sustained stimulation to neural interfaces. The porting function uses the measurand estimate to feed the Izhikevich neuron with the proper current magnitudes. So far, a simple proportional coefficient named Gain Factor (GF) had been used to convert raw output signals from sensors into current inputs for the Izhikevich neuron. GF had been tuned to guarantee enough discrimination among stimuli and not-excessive amplification of the noise carried by the signal, [147]. In the aforementioned study, by properly tuning the GF, the generated spike trains demonstrated able to yield to classification of naturalistic textures with the accuracy of 97%, but they did not investigate the physiological plausibility of the generated spike trains. From this perspective, the porting function presented in this study replaces the GF parameter of the model used in, [147]. The resulting spike trains emulate to some extent the biological model, thus paving the way for enhanced future applications in neuro-robotics and bionics. Indeed, biomimetic temporal patterns have been exploited to elicit artificial sensory feedback using a prosthesis in different studies, with the advantage of improving the prosthesis embodiment, [86], [150], [157], [170]. Among these approaches, the Izhikevich model was successfully used to discriminate stimuli and obtain natural sensations, but, to the best of our knowledge, the matching of the generated spike trains with the physiological one has not been investigated, [86], [150]. We believe that the proposed porting function improves the biological plausibility of the spike trains of the Izhikevich model. We select an appropriate input value to obtain the firing rate we would observe in a real mechanoreceptor with equal stimulation. This should lead to a better embodiment of the prosthesis with less training of the amputee. The main differences between our resulting spike trains and the biological ones are (i) the determinism of our model, compared to the stochastic nature of the biological system, [171], and (ii) the long-term behavior, since the adaptation of Merkel cells is slower, [172]. However, this characteristic can be achieved by properly tuning the parameters of the Izhikevich neuron model.

CONCLUSION

Reproducing the dynamics of the human somatosensory system is paramount for neuroprosthetics and neurorobotics applications. In

order to restore tactile feedback, it is convenient to reproduce mechanoreceptors dynamics according to a specific stimulus. In this work, we proposed and validated a method for obtaining the input to the spiking models of mechanoreceptors from the output of physical sensors typically employed in bioengineering applications. When indenting an artificial finger with a probe at different depths, the output voltage of its MEMS sensors was converted into the artificial mechanoreceptor input according to the designed porting function. The resulting spike trains appeared to be coherent with physiological recordings and the firing activity changed with indentation depth according to a physiological curve. Thanks to our study, in future works embedding a physical transducer will not require any change in the mechanoreceptor model, but only to apply the calibration inverse function to the sensor output and then to obtain, by means of the porting function, the proper input to an artificial neuron model in order to generate neuromorphic signals. In the perspective of its application to bionic limb prostheses, the model should be refined by ad hoc acquisition of human physiological data, similar to the approach pursued by other groups with primate subjects, [151]–[156]. We will also test the model with different stimuli, such as sinusoidal vibratory indentations, to unveil its ability to mimic the behavior of SA1 mechanoreceptors at different frequencies. Besides, since each stimulation is neutrally decomposed by different kinds of human mechanoreceptors (SA1, SA2, FA1, FA2), the method proposed in this work could be extended to other kinds of mechanoreceptor, possibly combining other porting functions with accurately selected parameters of the Izhikevich neuron.

3 Haptic Feedback For Medical Telepresence Applications

3.1 Encapsulation of Piezoelectric Transducers for Sensory Augmentation and Substitution with Wearable Haptic Devices[6]

3.1.1 Framework

In recent years, the development of haptic devices for different application purposes has increased. The growing spread of tactile displays is due to the high potential of the tactile sense as a communication channel for the remote transmission of information in a variety of situations. Due to the high number of tactile receptors located on our skin, particularly on the hands, [1], [2], the sense of touch represents a means to deliver information, which can also come from other sensory modalities such as vision and audition in sensory-disabled subjects, [173]–[177]. In this case, the information coming from one sensory channel is conveyed to the tactile sense in an understandable way. Technologies based on different actuation principles were integrated in haptic feedback systems. Polymeric actuators, like electro-active polymers, have been used for the development of tactile displays for rehabilitation or virtual reality applications, [178]. The ability of dielectric polymers to undergo large displacements, [179], [180] and their muscle-like behaviour made them suitable for the integration in haptic devices. Applications include tactile displays for the communication of textual and graphical information for blind persons, where electroactive silicone polymers were used for the development of planar arrays of pins, [180], [181]. These actuators were also integrated into tactile displays for the blind. A relevant example is a finger-tactile display initially designed to stimulate fingertips, made of a soft polymer which includes a matrix of dielectric elastomer dots that expand or compress transmitting information to the fingers, [182]. Arrays of piezo-electrically activated pins were also designed for the development of rewritable Braille cells, where a polydimethylsiloxane (PDMS) membrane encapsulated an

[6] This section has been excerpted from the paper, [11], that has been published in an international scientific journal: Micromachines, with the PhD candidate being co-author of the study.

incompressible fluid, [183], [184]. Electro-active polymers for virtual reality applications were used to develop haptic interfaces, like mice, joysticks, trackballs, gamepads, steering wheels, styluses, tablets, and pressure-sensitive spheres, [185]. The polymers' properties of softness and compliance, together with the easiness of their shaping with dedicated and customizable polymerization processes, make them a useful matrix for the encapsulation of transducers based on other actuation principles. A polymeric encapsulation can also facilitate the integration of the transducers in more complex haptic systems, i.e., wearable tactile displays for sensory substitution and/or augmentation in contexts like manufacturing, virtual reality, and rehabilitation. Anyway, the use of polymers as a soft interface between a transducer and the external environment is more common for the fabrication of sensors, especially tactile sensors based on MEMS, electrodes, or polyvinylidenefluoride (PVDF) sensing technology, [186]–[191]. Largely employed in the development of interfaces for haptic feedback are also vibro-tactile actuators. Vibro-tactile stimulation can be used for sensory substitution in sensory-disabled, or for sensory augmentation in non-disabled, individuals. Haptic stimulation for force feedback can, in fact, improve object manipulation tasks in virtual environments, and can be largely employed for rehabilitation, navigation, rescuing, and robot remote control purposes, [192]–[196]. Haptic displays were also proven useful in robotic surgery and in industrial environments, enhancing human-robot co-working. They can, in fact, allow the development of alerting devices in all those contexts where the interaction with automated machinery can be dangerous. Different vibro-tactile wearables can be found in the literature, designed for the various purposes already mentioned before, and actuated with technologies like pneumatic and piezoelectric actuators, vibrating motors, or solenoids, [197]. Vibro-tactile gloves were designed to allow deaf-blind individuals to communicate with the not-disabled community, [198], or to improve manipulation tasks in virtual reality applications, [199]. Belts and vests were developed to give vibro-tactile feedback in virtual reality (VR) applications, [200], [201], or to assist the navigation of visually impaired individuals, [202], [203], as were vibro-tactile wristbands. Prototypes of head-mounted devices were developed to haptically guide the user in unknown environments via tactors, [204], [205]. In the following, we focus on the development and evaluation of a piezoelectric transducer

encapsulated in a polymeric matrix, and on its integration in wearable haptic displays to deliver information via the tactile sense, starting from the hypothesis that the introduction of a compliant interface between the stiff piezoelectric element and the soft human skin can have an influence at a perceptual level. In previous studies a polymeric layer has usually been introduced to cover an array of active elements, [182], or a tactile sensor, [186], [191]. Our customized fabrication procedure allows to obtain an encapsulated element that enables the development of a single encapsulated actuator, scalable in size, with a very good match between modelled transduction and the actual prototype, and which can be integrated in a straightforward manner in wearable haptic devices for the stimulation of different body areas on single or multiple contact points. We found that the geometry and the material selected for the encapsulation of the transducer resulted in a system capable of reliably delivering vibro-tactile information, where this was confirmed both on the side of electromechano transduction behaviour and on the human somatosensory perception. The Section 3.1.2 of this work presents the design and fabrication procedure for the developed vibro-tactile haptic transducer with polymeric encapsulation, the finite element method (FEM) modelling of its transduction properties, and the procedures for its experimental evaluation; then, the results are provided and discussed with respect to the modelling and its assessment via bench tests, and the transducer is used within a psychophysical protocol involving healthy subjects; finally, the conclusions draw the perspectives for future applications of the system.

3.1.2 Materials & Methods

Piezoelectric Encapsulated Transducer

The implemented solution consists in the integration of a piezoelectric disk (7BB-12-9, MuRata, Kyoto, Japan), 12 mm in diameter and 220 µm in thickness, in a polymeric matrix (polydimethylsiloxane, PDMS, Dow Corning (Midland, MI, USA) 184-Silicone Elastomer). The PDMS encapsulation serves both the mechanical and electrical roles. It allows electric contacts to be encapsulated, providing electrical insulation of the element. In addition, it allows obtaining a system that can be easily inserted in wearable haptic devices, such as gloves and wristbands for the upper-limb stimulation, or ankle bands and insoles for the lower-limb

stimulation. The compliance of the polymeric encapsulation constitutes also an adaptation interface between the stiffness of the transducer (Piezo devices made of lead zirconate titanate (PZT) on a brass mass) and the softness of the human skin The development of the encapsulated transducer is articulated in different steps. The first step is the development of two polymeric (PDMS) elements in the shape of spherical cups with the same diameter of the piezoelectric disk 2 mm in height (Figure 40a). These elements are obtained by a casting process in customized 3D-printed moulds. Elements are also provided with a housing on the flat side, designed to contain the electrical wires connected to the piezoelectric disk. In order to fix the wires on the transducer, the spherical cups are placed on the opposite sides of the piezoelectric disk after the application of a conductive epoxy (CircuitWorks conductive epoxy—Chemtronics (Kennesaw, GA, USA)), (Figure 40b), and the whole resulting system is closed in a further 3D printed customized mould for the final polymeric encapsulation, which will be made of the same material (Figure 40c). The role of the polymeric spherical cups protruding from each side of the external surface is to keep the piezoelectric element centred in the encapsulating polymer (Figure 40d). At the same time, they create two bumps on the external sides of the element in order to focus the transducer deformation, the vibro-tactile stimulus, in a specific contact area on the skin. The choice of a spherical cup as a contact region on the skin is due to heuristic design criteria. On one side, a spherical protrusion simplifies the implementation of some steps of the encapsulation process. Furthermore, protruding edges, [189] or bumps, [182]–[184] showed proper functionality in the design of matrices of tactile actuators, and bumps are the most used in Braille displays. We opted for a spherical-like shape to avoid sharp edges on the actuator surface and to increase the comfort of the wearer. The dimensions were chosen in order to have a perceptible protrusion which could help position the actuator on a specific contact point on the skin, but also to avoid a very large difference in height from the actuator surface. The resulting contact area was about 18.2 mm^2 which, in case of multiple transducers, results in a spatial distribution just higher than the minimal range guaranteeing reliable two-point discrimination on fingertips (0.5 mm [206] –1.6 mm [104]).

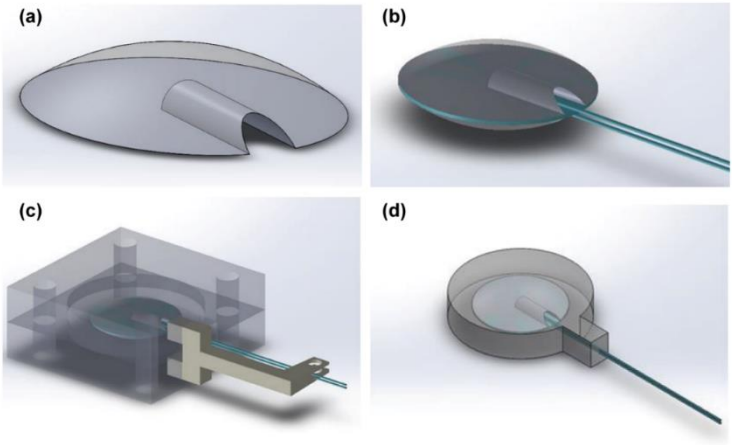

Figure 40: a) Upper view of one of the spherical cups; (b) Encapsulated transducer with the two spherical cups on the opposite sides and the embedded electrical contacts; (c) 3D printed customized mould for the development of the geometry of the transducer with PDMS polymer. In this structure, the piezoelectric element with the spherical cups and the electrical connections will be centred; (d) Upper view of the transducer, with evidence of the internal structure where two spherical cups enclose the piezoelectric disk and the electrical wires.

FEM Model of Transducer's Electro-Mechanical Behaviour

A finite element method (FEM) simulation of the piezoelectric transducer was performed using COMSOL Multiphysics (COMSOL Inc., Palo Alto, CA, USA). We considered the geometry introduced in the previous paragraph. The mechanical properties of PDMS necessary to run the simulations were the Young's modulus, Poisson's ratio, and density. The acoustic properties were not explicitly needed as inputs for the simulation. They were consistently derived by the numerical solver so that no additional characterization was required. The density was verified from the mass/volume ratio of auxiliary samples. The derived value was in agreement with the one available in the adopted library (970 kg/m^3). Regarding the PDMS Poisson's ratio, we adopted 0.5 from the literature, [207], [208] (its dispersion is low, and the same value was provided as the reference PDMS Poisson's ratio in the material library of the chosen solver). Differently, the PDMS Young's modulus sensibly depends on the actual material composition and therefore we assessed the reference value provided in the material library through a complementary calibration experiment described in the following paragraph. Finally,

as for the PZT material properties, we adopted the elastic and piezoelectric coefficients and electric permittivity provided by the material library of the chosen solver (an extensive characterization of this commercial material was beyond the present scope). The purpose of the numerical simulations was to estimate the normal force exerted by the piezoelectric transducer at different frequencies and driving voltages. In particular, we chose 50V, 100V, and 150V as the driving peak-to-peak voltages for the sake of definiteness, and we selected a frequency range between 200 Hz and 700 Hz. The choice of such a frequency interval allows the activation of the transducer within the Pacinian frequency range, centred around 300 Hz, [104], [173], [209], [210] , for which the maximum sensitivity for vibro-tactile stimulation is expected. Furthermore, previous studies, [211] showed that the subjective amplitude perception of the vibro-tactile stimulus is not influenced by the frequency in this specific interval (200–700 Hz). Based on the experimental conditions described below, we imposed a null displacement (u = 0) on the bottom and lateral surface of the PDMS encapsulation material, whereas we imposed a compression load of 1 N on the PDMS upper surface (see Figure 41).

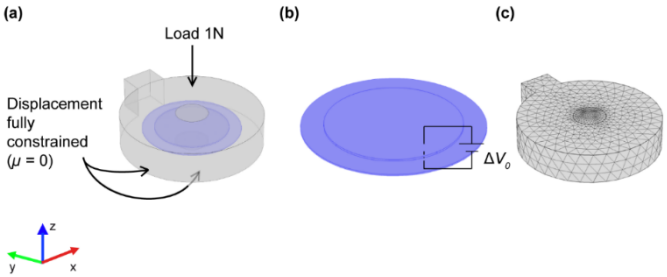

Figure 41: (a) Schematic of the actuator showing the boundary conditions on the PDMS structure; (b) Detail of the piezoelectric disk showing the driving voltage imposed on the element; (c) View of the meshed geometry of the whole encapsulated transducer.

We imposed the driving voltage on the piezoelectric disk (ΔV_0), and we gathered via a load cell (Nano43, ATI Industrial Automation, Apex, NC, USA), the resulting force normal to the PDMS bottom surface. In addition, we preliminarily set up the numerical discretization so as to obtain grid-independent results, which led to a mesh composed of 675,062 tetrahedral elements (160,731 volume elements, 23,068 surface elements, and 843 edge elements). We also considered an

axisymmetric model, derived from the three-dimensional one through minor geometrical simplifications, to assess the adopted numerical technology. For all the runs, we considered the fully-coupled (*i.e.,* electro-mechanical) problem by exploiting the corresponding modules natively provided with the FEM simulation environment.

Preliminary Mechanical Characterization of the PDMS

A mechanical characterization of the PDMS was performed in order to assess the Young's modulus. A cylindrical probe (ϕ 6 mm) moving along the Z-axis through a motorized translational stage was used to indent a PDMS sample (30 mm × 30 mm × 3 mm). The probe was mechanically linked with a load cell (Nano 43, ATI Industrial Automation) in order to apply a predefined value of force and, thus, establish a relationship between the applied force and the corresponding polymer displacement (indentation; set to be null when contact was first established). The resulting experimental trend was then compared to the one obtained from a numerical simulation of the considered indentation test, exploiting, in particular, the Young's modulus provided by default by the adopted numerical solver.

Experimental Setup

In order to perform the mechanical characterization, the transducers were actuated by means of a piezo haptic driver (DRV2667 Evaluation module, Texas Instruments, Dallas, TX, USA) using a graphical user interface (GUI) (LabVIEW, National Instruments, Austin, TX, USA) that activated the driver through an electronic board (sbRIO 9636, National Instruments). Before human evaluation of the system, we assessed the ability of the haptic interface to deliver perceptible and discriminable stimuli using a load cell (Nano 43, ATI Industrial Automation), in order to provide input stimuli and record the resultant vibrations (Figure 42), [212]. Such measurements were then compared with the FEM simulations described in previous paragraph.

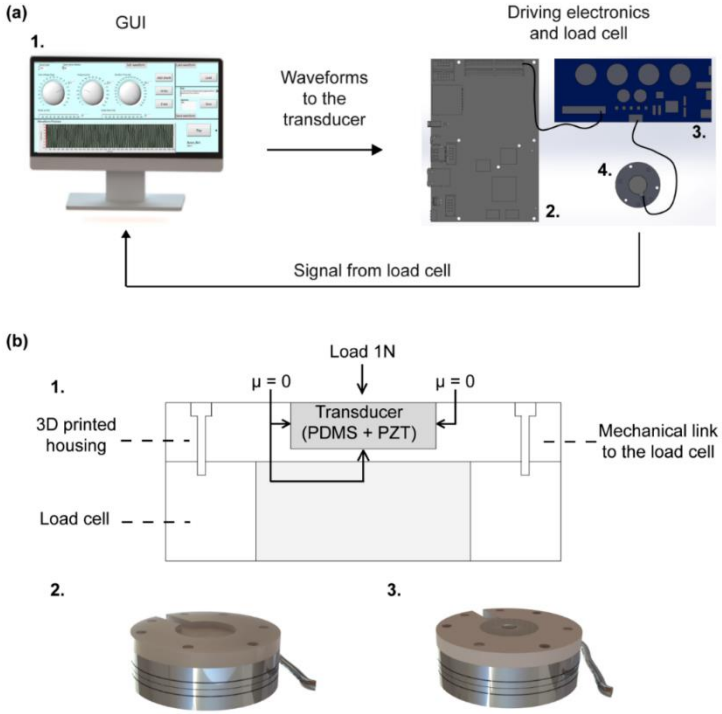

Figure 42: Experimental setup for the evaluation of the normal force. (a) Schematic drawing of the experimental setup. 1. PC running a GUI to send selected waveforms to the piezoelectric transducer via a driving electronics; 2. Electronic board for the communication between the GUI and the piezo haptic driver; 3. Piezo haptic driver for the activation of the piezoelectric transducer; 4. Load cell for force measurement: the measured forces are saved for post-processing. (b) Detail of the measurement system, where the encapsulated transducer is fixed on the load cell. 1. Section of the measurement system, in which the encapsulated transducer in fixed in a 3D printed housing linked to the load cell, with detail of the experimental boundary conditions; 2. CAD representing the measurement system, with a 3D printed housing linked on the upper part of the load cell; 3. CAD representing the whole measurement system, in which the encapsulated transducer is inserted.

Experimental Procedure

The experimental mechanical characterization of the encapsulated transducer was performed in order to evaluate the element behaviour with the variation of the driving voltage (measured in peak-to-peak-Vpp) and the frequency. In order to do so, we measured the amplitude of the normal force (F_Z) exerted by the piezoelectric element on a load cell. To stabilize the transducer

during the experimental tests, a 3D-printed housing was fixed on the load cell (Figure 42). Furthermore, a load of 1 N was placed on the upper surface of the encapsulated transducer in order to keep it stable during the measurements and to emulate a typical pre-load that can be exerted on the device during its use. Such an offset load was then subtracted from the dynamic measurements of the load cell. piezoelectric element was driven with stimuli lasting 1 s. The stimulation signals were characterized by three values of amplitude (50, 100, and 150 Vpp), kept constant across each stimulation, and 21 values of frequency varying between 200 Hz and 700 Hz, with 25 Hz steps. These settings were consistent with those adopted for the model. The values of the normal force (F_Z) exerted on the load cell during the excitation were acquired across 10 repetitions for each vibration frequency and each peak-to-peak voltage.

Data Analysis for the Electromechanical Characterization of the Encapsulated Transducer

The waveforms obtained from the measurements of the load cell were then analysed with the calculation of the signal power (standard deviation of the amplitude of F_Z). The data analysis was performed across 750 samples for each frequency value, where the sampling window was selected in the central part of the signal to focus on the steady state of the dynamic activation of the piezoelectric transducer. Spectral analysis was performed on F_Z using the MATLAB (R2016b, MathWorks, Natick, MA, USA) wavelet coherence package, [213], for each peak-to-peak voltage and each frequency value in the range between 200 Hz and 700 Hz, with 25 Hz steps and 50 Hz steps.

System Integration for Psychophysical Evaluation

The described encapsulated transducer was used for the development of a wearable vibro-tactile device for the stimulation of the hand, *i.e.,* a haptic glove (Figure 43a-d). For the psychophysical evaluation of the tactile display, we designed three experimental configurations: two single-finger, with the stimulation of the index (SF-I) or thumb (SF-T) fingertip; and one bi-finger (BF-S), with the simultaneous stimulation of the index and thumb fingertips. In the SF-I and SF-T configurations, one transducer was integrated, respectively, on the tip of the index finger (Figure 43c) or thumb (Figure 43d) of a spandex glove; for the BF-S configuration two transducers were integrated on the tips of the index finger and

thumb of the same spandex glove (Figure 43b). In all configurations, the glove allowed a secure positioning of the vibrating element on the participant's fingers. The transducers provided a contact area with the finger pad of approximately 250 mm^2. The electrical actuation was delivered to the transducers via the electronics, *i.e.,* a piezo haptic driver controlled using a GUI and interfaced with the driver through an electronic board, [212].

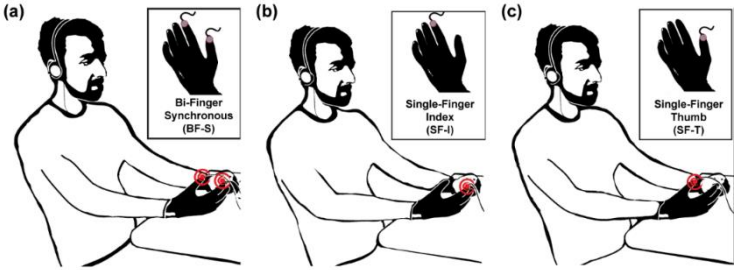

Figure 43: Experimental setup with the three experimental configurations. (a) Bi-Finger Synchronous (BF-S) configuration: two piezoelectric transducers, embedded in a spandex glove, stimulate synchronously the tips of the index and thumb finger; (b) Single-Finger Index (SF-I) configuration: single-finger stimulation on index fingertip with one piezoelectric transducer embedded in a spandex glove; (c) Single-Finger Thumb (SF-T) configuration: stimulation on thumb fingertip with one piezoelectric transducer embedded in a spandex glove.

Psychophysical Evaluation

We evaluated the ability of the integrated wearable haptic system to deliver accurate tactile feedback using a two-alternative forced choice (2-AFC) psychophysical protocol. According to previous studies, we chose to use frequency modulation as a mean to deliver haptic information. Even if the exact number of discriminated levels is not clear yet, it can increase when stimuli differing in frequency are relatively compared, [210]. Studies regarding the amplitude modulation showed instead that, for constant frequencies, when the vibration amplitude increases, the perceived frequency also increases, [214]. According to these studies, and to the experimental data from our measurements, we decided to select a fixed driving voltage of 150 Vpp for the psychophysical experiments. This value corresponds to the higher value of normal force exerted on the actuators' sides and, according to preliminary psychophysical tests, was the one which showed the best performance across 10 participants, [212]. The frequency modulation was then performed

in the range between 200 Hz and 700 Hz, that guarantees a proper functioning of the transducer according to the FEM analyses. Thirty-three healthy participants (15 females and 18 males), aged between 25 and 37, participated in psychophysical experiments. Haptic stimulation was performed on the dominant hand which, for 31 participants, was the right hand. No participant had previously performed any activity presumably compromising finger tactile sensitivity. All participants provided written informed consent for inclusion before they took part in the study. The study was conducted in accordance with the Declaration of Helsinki, and the protocol was approved by the Ethics Committee for non-clinical experimentation of Scuola Superiore Sant'Anna of Pisa.

Experimental Procedure

A tactile discrimination task with the 2-AFC procedure, [215] was designed, and was performed by each participant. Periodic vibro-tactile stimulation was delivered using the haptic glove described in the previous paragraph. The experimental session consisted of the presentation of 150 pairs of stimuli divided into 15 sequences, as described in the following. Each participant was presented with paired vibro-tactile stimuli (Figure 44a-b) and was asked to identify which stimulus of the pair had the higher frequency content (Figure 44c).

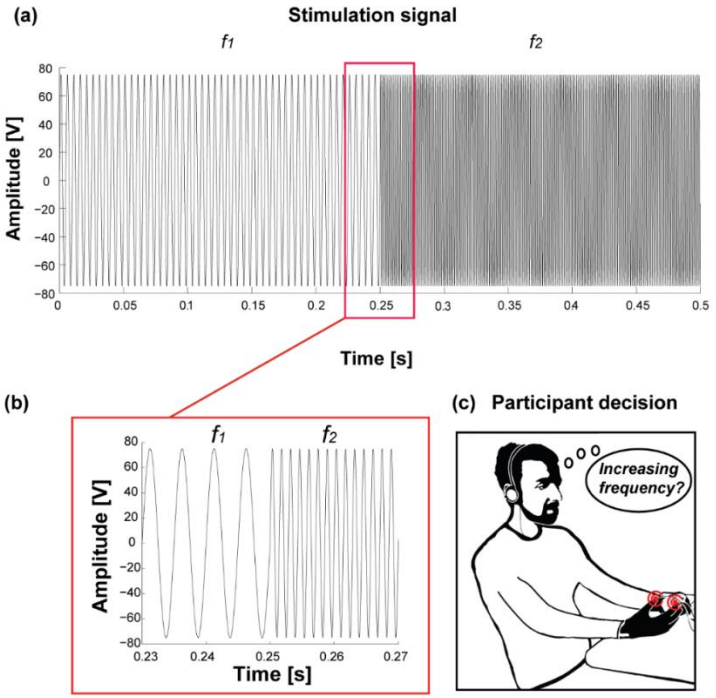

Figure 44: Stimulation and task. (a) An example of a pair of stimuli: 250 ms of sinusoidal oscillations with a frequency of 200 Hz followed by 250 ms sinusoidal oscillation with a frequency of 700 Hz. The peak-to-peak amplitude activating the transducer was fixed at 150 V; (b) A 0.04 s slice of the vibro-tactile stimulation shown in panel (a), depicting the frequency transition at 0.25 s; (c) Participant decision phase: after perceiving the vibro-tactile stimuli pair, the participant was asked to determine whether the first or the second had higher frequency content.

A stimulation sequence included a single presentation of each of the 10 pairs of stimuli described in Table 5 in random order. An 8 s interval was introduced to separate each subsequent stimuli pair, leading to a sequence duration of about 2 min. A rest period of about 1 min spaced the 15 sequences, for a total average duration of 45 min. Two randomized sequences were used for training purposes. These sequences were not included in the statistical analyses and were sufficient for the participants to familiarize with the stimuli. As briefly explained in the introduction, we delivered vibro-tactile stimuli following three experimental configurations. In this way, we were allowed to test the human hand tactile sensitivity to frequency

variations under different perceptual conditions. Each configuration was tested with 11 participants. Each participant was comfortably seated on a chair for the duration of the experiment for all tested configurations, and he/she was acoustically isolated from the environment with white noise provided by headphones.

Table 5: Experimental stimulation parameters. Ten pairs of vibro-tactile stimuli. First vibro-tactile stimulus f_1, second vibro-tactile stimulus f_2 and related frequency variation $\Delta f = f_2 - f_1$.

f_1 [Hz]	700	650	600	550	500	400	350	300	250	200
f_2 [Hz]	200	250	300	350	400	500	550	600	650	700
Δf [Hz]	-500	-400	-300	-200	-100	100	200	300	400	500

DATA ANALYSIS FOR PSYCHOPHYSICAL EXPERIMENTS

Data analysis was performed using the Statistics Toolbox in MATLAB. To compare the performance of different configurations, the Kruskal-Wallis test was used. For each configuration and frequency variation, the vibro-tactile perception of a population of participants was evaluated by the median and the 95% confidence interval of the rates of identification of stimuli having an increasing frequency ($\Delta f > 0$), calculated with *binofit* test. A logistic fit of the resulting psychometric curves was computed for each configuration across presented frequency variations. To analyse the significance of participants responses for each frequency variation Δf and experimental configuration, the *binofit* test was used.

3.1.3 Results & Discussion

ENCAPSULATED PIEZOELECTRIC TRANSDUCER

We developed an encapsulated transducer, 18 mm in diameter and 4 mm in thickness (Figure 45) (see methods for details). Its shape is characterized by two spherical cups which protrude out 250 µm from the upper and lower levels of the polymeric matrix (upper part of Figure 45a-b). These elements allow skin stimulation at a specific contact point. The presence of the spherical cups allows to centre the piezoelectric element in the polymeric shell, as shown in the lower part of Figure 45.

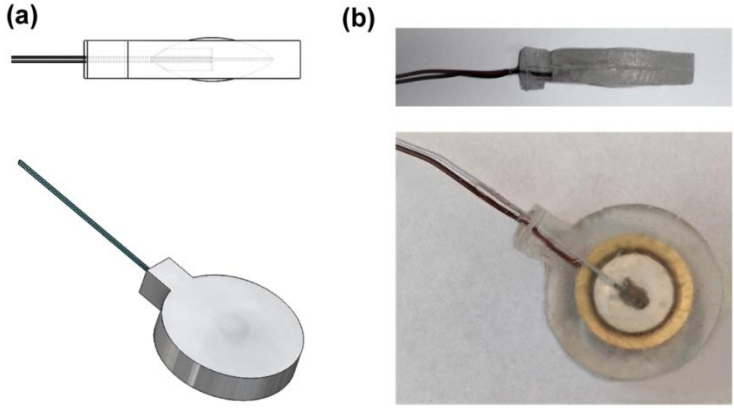

Figure 45: Embedded piezoelectric transducer. (a, upper part) Drawing of the lateral view of the piezoelectric transducer embedded in the polymeric matrix, with evidence of the two protrusions on the external opposite faces of the geometry; (a, lower part) Drawing of the upper view of the piezoelectric transducer embedded in the polymeric matrix; (b, upper part) Lateral picture of the developed prototype showing the side of the actuator; (b, lower part) Upper picture of the developed prototype showing the whole surface of the actuator.

Results of the Preliminary Experimental Mechanical Characterization of the PDMS

Results from the experimental characterization of PDMS validated the stiffness of PDMS test blocks, maintaining the mechanical parameters of the material as available in the software library. In particular, the trend of the obtained force vs. displacement was compared with the one obtained from the model of the considered indentation test. The simulation outcomes appear to match the experimental data, to consider the library parameters of the material accurate enough to describe the PDMS used in our study (Figure 46). As a consequence, we could safely exploit the parameters available in the COMSOL material library to run the FEM dynamic simulations presented in the next paragraph.

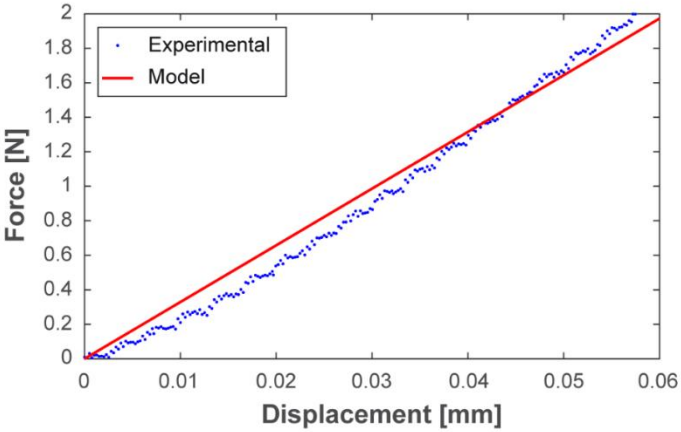

Figure 46: Characterization of the PDMS Young modulus and corresponding model calibration, based on complementary indentation experiment. The close agreement between experimental (blue dots) and simulated data (red line) confirmed the suitability of the chosen parameter.

Transducer FEM Model and Experimental Characterization

The results of the FEM model are shown in Figure 47 (solid lines with circles), together with the corresponding experimental measures (dots). The model was able to accurately predict the observed experimental response. For each driving voltage and each frequency, the mean value and the standard deviation of the normal force (over the 10 repetitions) are represented in Figure 47. In most cases, the vertical bars representative of the standard deviation are hardly visible thanks to the high repeatability of the experimental conditions. From Figure 47 we can conclude that, as expected, the amplitude of the vibrational component of the normal force increases with the increase of the transducer driving voltage. Figure 47 also show the vibration amplitude is weakly varying over the analysed frequency range for each driving voltage (for 150 Vpp driving voltage, the variation of the normal force amplitude is about 0.025 N across the selected frequency range). These results demonstrated that the variation of the normal force is mainly related to the driving voltage amplitude.

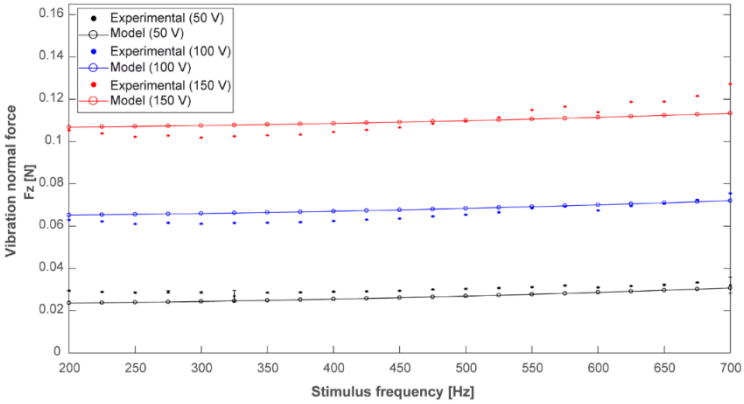

Figure 47: Normal force exerted during transducers actuation. Predicted trend (solid lines with circles) and experimental measures (dots) of the normal force for the considered driving voltages. For each experimental point, the standard deviation is represented by vertical bars.

Increasing the voltage value (from 50 V to 150 V) three times leads to a fractional variation of the recorded force of about 300% ± 25% over the whole range of frequencies. Increasing the frequency value three times (from 200 Hz to 600 Hz) leads, instead, to a force variation always lower than 10% for all of the driving voltage conditions (50 V, 100 V, and 150 V). The weak relationship from the value of frequency within the selected range allows a straightforward application of the transducer in haptic displays for the stimulation of the human hand. Spectral analysis showed coherence with the nominal stimulation parameters. For each stimulation amplitude (50, 100, and 150 Vpp, see Figure 48a-c) the encapsulated transducer showed coherency in the stimulus presentation within the whole examined frequency range, with evident vibratory changes across the analysed peak-to-peak amplitudes and frequencies. The same is visible in Figure 48d–f showing the frequency values selected for the psychophysical testing (range 200Hz–700Hz, with 50 Hz steps). These experimental results allow to conclude that the vibro-tactile stimuli delivered to the participants were coherent with the frequency values selected for the experimental testing and, thus, the transducers embedded in the polymeric matrix can deliver vibro-tactile information in a reliable manner

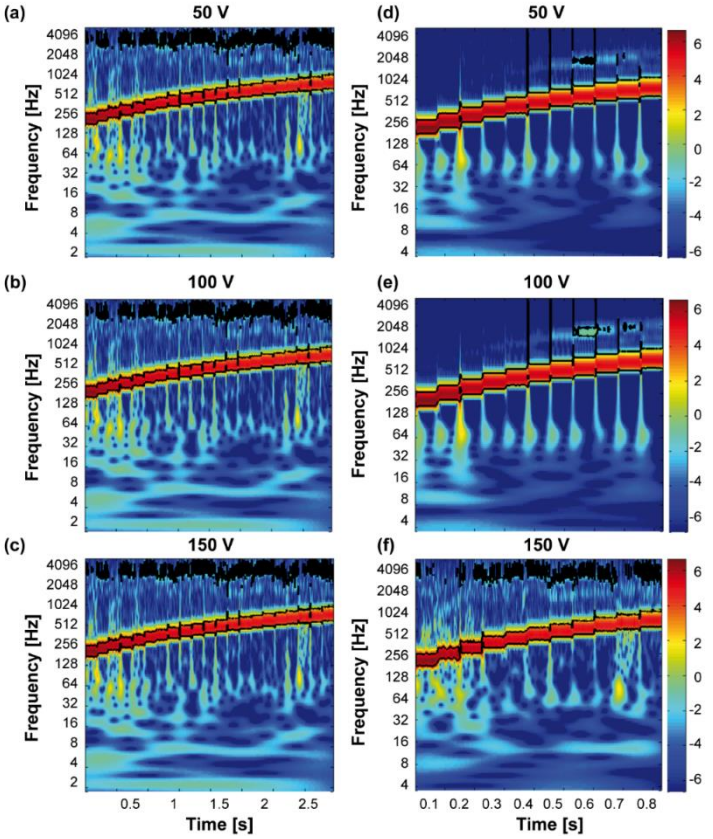

Figure 48: Frequency power spectrum of the normal force. Spectral analysis of the normal force recorded by the load cell while activating the piezoelectric actuator/polymer system. (a) Results for 50 Vpp and 200-700 Hz, with 25 Hz steps (mechanical characterization); (b) Results for 100 Vpp and 200-700 Hz, with 25 Hz steps (mechanical characterization); (c) Results for 150 Vpp and 200-700 Hz, with 25 Hz steps (mechanical characterization); (d) Results for 50 Vpp and 200-700 Hz, with 50 Hz steps (psychophysical experiments); (e) Results for 100 Vpp and 200-700 Hz, with 50 Hz steps (psychophysical experiments); (f) Results for 150 Vpp and 200-700 Hz, with 50 Hz steps (psychophysical experiments).

Psychophysics Results

Results from psychophysical testing for all the experimental configurations are shown in Figure 43 and are reported hereafter. The average performance over all the 10 frequency variations was significantly above chance for both bi- and single-finger configurations, with non-significant differences between the mean

discrimination performances achieved under different stimulation configurations (as shown in Figure 49a: n = 11 for every group; 77 ± 11% for BF-S vs. 70 ± 8% for SF-I vs. 66 ± 12% for SF-T; p=0.51, Kruskal-Wallistest). In particular, frequency differences larger than 100 Hz were reliably identified in all configurations (Figure 49b-c-d) developed integrated haptic system was thus effective in delivering vibro-tactile information for both single-finger and bi-finger configurations when the frequency delivered to the skin was within the 200–700 Hz range and the stimulus variation was larger than 100 Hz. Furthermore, in the explored frequency variation range (Δf = −500 –500 Hz) the psychometric curves obtained from experimental data for single-finger configurations, as well as the one for bi-finger configuration, were accurately fitted by logistic curves over the whole range of frequency variations (Figure 49b–d), χ^2 = 0.43 for BF-S, χ^2 = 0.68 for SF-I and χ^2 = 1.02 for SF-T). When calculating the psychometric curves to evaluate performance as a function of frequency variation, the differences between bi-finger and single-finger configurations showed that two-digit perception has a frequency sensitivity to vibro-tactile stimulation comparable to the one relative to single-finger perception (compare Figure 49b with Figure 49c,d).

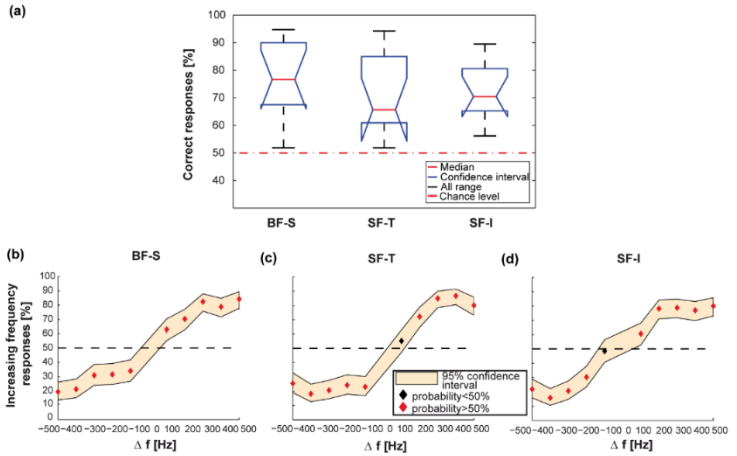

Figure 49: Stimuli perception with single-finger configuration. (a) Comparison between the fraction of correct responses (i.e., increasing frequency variations identified as increasing or decreasing frequency variations identified as decreasing) in all the three configurations. Boxes represent the interquartile range and black dashed lines show the complete range across participants; (b) Psychometric curve for BF-S stimulation

configuration. Each dot represents the fraction of times each stimulus was classified as having an increasing frequency (median across participants). If the identification rate is significantly different (average>50%, binofit test) from chance the dot is red, otherwise, it is black. The filled area indicates the 95% confidence interval (binofit test) across participants and the black horizontal dashed line represents chance; (c) Same as (b) for SF-T stimulation configuration; (d) Same as (b) for SF-I stimulation configuration.

For all configurations, Figure 50 shows the comparison between logistic fits of frequency variations identified as increasing. Over the full range of frequency variation, the two single-finger configurations and the bi-finger configuration had similar logistic fit curves.

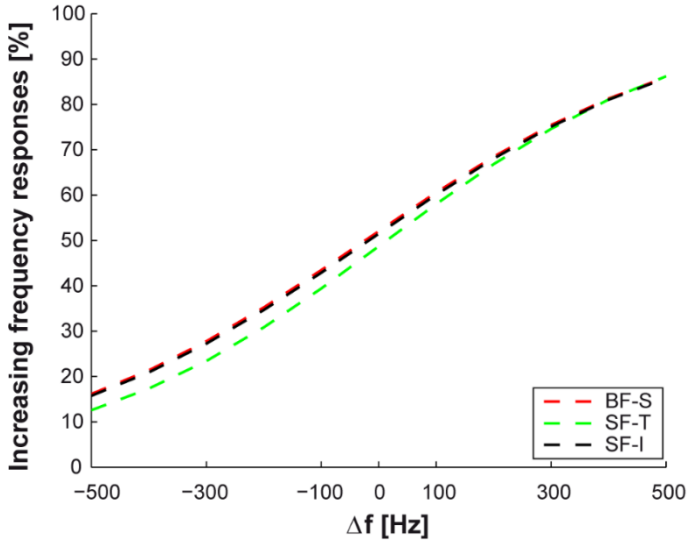

Figure 50: Comparison of logistic fit of psychometric curves for all configurations. Comparison of logistic fit curves over the whole range of frequency variation. The curves are similar for all the three experimented configurations.

Conclusions

In this work we *i)* described the mechanical behaviour of a piezoelectric disk encapsulated in a polymeric matrix, specifically designed for the integration in wearable haptic displays, and *ii)* characterized the behavioural performance in sensory discrimination of healthy human subjects wearing such displays. The FEM modelling showed that the normal force exerted by the encapsulated element

presents a constrained variation across the experimented frequency range for the three selected driving voltages. This modelled behaviour was confirmed by the experimental testing. The psychophysical testing of an integrated haptic system, a vibro-tactile glove for the stimulation of the index and/or thumb fingertips of the human hand, demonstrated that the developed haptic transducer is effective in delivering vibro-tactile information. The transducer described herein presents some advantages with respect to the recent technological solutions for wearable tactile displays, such as: *i)* the piezoelectric actuator enables the selection of a wide range of stimulation frequencies in the perceptual frequency range with a fine selection of frequency steps. This is true especially when piezoelectric elements are compared to polymeric actuators, like dielectric elastomers. The former allows selecting frequencies in both low and high frequency ranges. They can be used for the stimulation of both slowly-adapting and fast-adapting tactile receptors, in particular Pacinian corpuscles more sensitive to vibro-tactile stimuli; *ii)* piezoelectric disks also limit the space required by the actuator, enabling a straightforward integration in wearable systems like gloves, and provide appropriate spatial resolution for being placed on different areas of the skin. These advantages are evident when our solution is compar the block proposed in this study ed to tactile actuators like pneumatics, vibrating motors, solenoids and to exoskeletons. In fact, a wearable device should fit the wearer's body and allow the natural movements of the body part on which it is applied. When worn on the hands, tactile actuators must be lightweight and have limited dimensions, [197]. The introduction of a polymeric shell to encapsulate the active element allows obtaining an integrated actuator which can easily fit in a wearable system for the stimulation of different body areas. The polymeric encapsulation also behaves as an interfacing layer between the piezoelectric element and the user's skin, and our particular geometry allows the selection of a precise contact site to stimulate the insulation of the electrical connections increasing the actuator safety, and obtain an easy-fitting element. The transducer presented herein, thanks to its particularly shaped polymeric encapsulation and its broad range of actuation frequencies, can be effectively employed for the development of tactile displays suitable to different application scenarios. This encapsulated piezoelectric transducer can be integrated within tactile displays for sensory substitution to assist the

blind or visually-impaired, deaf or hearing-impaired, and combined sensory impaired (deaf-blind) individuals. Several examples can be found in the literature about tactile aids used to convey the information coming from one sensory channel to the tactile sense in a perceptible manner, [173], [174], [177], [216]. Other applications can involve the integration of our encapsulated actuator in devices providing non-invasive tactile feedback to amputees. It can be also integrated in sensory augmentation technologies for healthy subjects in applications such as virtual reality, gaming, rehabilitation, navigation, rescuing, and remote control of robots, where vibro-tactile stimulation is already widely used, [192]–[196]. Haptic feedback also has significant advantages in robotic surgery and industrial environments for human-robot co-working activities. We are also considering the possibility to integrate this encapsulated actuator in haptic wearable systems for alerting purposes, in environments where the interaction with automated machinery can be dangerous for operators. This solution may improve safety in dangerous workplaces and the adoption of collaborative robotics in common applications. Towards deployment in such scenarios, this study will be complemented with future experiments where these novel vibro-tactile transducers can be integrated into different wearables, according to the particular application they will be involved in.

3.2 Neuromorphic Vibro-tactile Stimulation of Fingertips for Encoding Object Stiffness in Telepresence Sensory Substitution and Augmentation Applications[7]

3.2.1 Framework

The use of haptic technologies to deliver tactile information in real-time has grown in recent years, because of the effectiveness of the human tactile sense as a communication channel for different kinds of object information. We use the sense of touch to interact with the surrounding world, especially through the hands, which represent the most somato-sensitive part of our body, [59], [217]. Individuals who have experienced the loss of this sense cannot properly perform actions, such as using tools or holding objects. For these persons, motor control tasks can also become extremely difficult or impossible to perform, [218], [219]. The possibility to deliver tactile information directly onto the users' skin, and especially on the hands, via tactile feedback can enhance the performance of tasks executed in different scenarios. This could contribute, amongst others, to rehabilitation procedures, as well as to the development of tactile aids for visual and audition sensory disabled persons since the seminal works of Bach-y-Rita, [220]–[224], as it has been discussed in perspective and review papers on the topic, [225], [226]. These individuals could improve their communication and navigation abilities through the use of wearable or hand-held haptic aids, particularly those which deliver information related to another sense via the tactile channel, [227]. The delivery of tactile information is also fundamental in contexts where fine control of mechanical tools or robotic hands is required. More generally, the real-time representation of tactile information is highly important in virtual reality and telepresence contexts, where a user is allowed to perceive his/her presence in a virtual or remote real environment. Therefore, in order to reach a higher level of realism in these situations, visual and auditory stimuli shall be accompanied by haptic sensations with tactile feedback, [13]. The stimulation of the tactile sense facilitates direct contact with virtually or remotely explored objects, providing the perception

[7] This section has been excerpted from the paper, [136], that has been published in an international scientific journal: Sensors, with the PhD candidate being co-author of the study.

of characteristics such as weight, stiffness, thermal and geometric properties. In the last decades, a variety of research has focused on the development of devices for the provision of tactile information in telepresence, mainly with sensory augmentation or substitution purposes, [228]–[231]. However, there is still a significant gap between the wealth of research prototypes and the limited number of wearable haptic technologies that have reached a proper readiness level to turn into commercial devices. Tactile information presented on the skin is collected by all the mechanoreceptors distributed in the stimulated areas and the dedicated receptors can then provide information about the characteristics of an object, [19]. In general, the hand is the most selected area to be stimulated because receptors within the skin of human hands have the highest body density and are able to encode a relatively wide range of stimulation frequencies, [104], [173], [209], [210], with a concurrent role of the different receptor types, [66], [232]. Slowly adapting (SA) fibers (Merkel and Ruffini mechanoreceptors) respond dominantly to sustained stimuli with main frequencies up to 100 Hz, [233], while rapidly adapting (RA) fibers (Meissner and Pacinian mechanoreceptors) are involved in the representation of vibrations and tickle, with activation frequencies reaching 200–300 Hz for Pacinian receptors, [232]. The maximum spatial sensitivity is achieved on the index phalanx, where the location of the presented tactile stimulation is precisely encoded, [234]. The delivery of tactile feedback in telepresence operations, [192], [193], [195], [196] is fundamental to augmenting users' perception capabilities in scenarios such as industrial manufacturing. When robotic end-effectors are highly involved in both force and precision gripping tasks, there could be the possibility to improve high-precision manipulation activities with the development of human–robot control systems. Another important application is robotic surgery, where tactile feedback on a surgeon's hand can transmit the characteristics of the inspected tissues, [194], [235], [236]. In the last few years, much effort has been devoted to this field, for the development of systems for biomedical applications such as telemedicine and tele-robotics, and for the development of tactile sensors and actuators for non-structured environments, [7]. In the last ten years, the advantages offered by medical robots for different procedures became clearer to the medical community, [237]. A telling example is minimal invasive surgery (MIS), where the surgeon

works out of the operating table and the manipulations are transmitted to the operation site by means of instruments, [238]. In all these situations, a major drawback on performance is the absence of direct tactile feedback on the surgeon's hands. In fact, tactile information is indicative of the condition of the operated tissues, but is also useful to ensure the correct manipulation of instruments, [239]. An instrumented palpation would help to characterize tissues according to their elasticity and stiffness, to precisely localize tumours and lesions. For these purposes, some devices were developed in order to detect tumorous tissues, [7], or to manipulate and characterize the properties of organs during robotics-assisted surgical interventions, [240]. Some feedback mechanisms are being evaluated in laboratory environments in robotic surgery, like in the "Da Vinci" system (Intuitive Surgical Inc., Sunnyvale, CA, USA), where a force feedback system partially compensates for the absence of direct tactile feedback, [7], or in which some tactile sensors were integrated in order to deliver tactile feedback on the surgeon's hands via a pneumatic tactile display, [7], [241]. Force feedback devices such as the "Phantom" were also integrated in the "Zeus" surgical system, [237]. Despite all these initial efforts, we are still far from a satisfactory delivery of tactile sensation in surgical environments. In the present study, we tested the reliability of a tactile telepresence system in delivering feedback information about the stiffness, *i.e.,* the ratio between a compression force and the resulting deformation of the tissue, of selected polymeric samples to the hand of an operator placed remotely with respect to the inspecting system. The study was designed with possible applications in the field of industrial and surgical robotics. Our approach is based on the conversion of information about the stiffness of rubber surfaces in vibro-tactile stimuli by means of neuronal spiking models. This encoding strategy enables the real-time conversion of force information in neuronal spikes, which are delivered directly on the skin of the fingertips of the hand of a remote human subject. In our novel approach, the spikes, usually delivered via neuronal electric stimulation directly on nerves to restore tactile sensation in amputees, [86] or to investigate how tactile information is encoded in the brain, [148], are presented mechanically on the surface of the skin. The developed feedback strategy is based on a spiking neuron model and thus allows a discrete-events encoding of tactile information: the proposed approach aims at merging together the simplification mechanisms of

the discrete event-driven sensory feedback control (DESC) policy, [174] with the possibility of delivering qualitatively-rich haptic information. Technically, the advantages of the proposed solution are the elegant and adaptable formulation via the differential equations that govern the Izhikevich artificial neuron, in place of the case-based programming that typically occurs with state machines in traditional systems. Another major technical advantage of the developed system is in its capability to reduce the bandwidth required to transfer and store information, as demonstrated in previous studies, [147], with the potential advantages in enabling the streaming of data from large networks of tactile sensors in haptic telepresence applications. The main purpose of the present study is thus to investigate the mechanisms of tactile perception and the feasibility of the proposed feedback strategy, according to which vibro-tactile information is delivered to the skin with an encoding strategy resembling the tactile receptor language, with the adaptation of models recently presented by our group, [86], [147], [148]. The assumptions made in proposing this experimental paradigm are quite strong, because the temporal characteristics of the code delivered to the skin resemble the output—not the input—language of the receptors: this approach somehow resembles the contingency–mimetic strategy, [242]–[244]. The scientific question addressed is then whether this language can be effectively understood even if delivered onto the skin surface rather than into the nerve (the approach typically pursued in prosthetics, [86]). The telepresence device is constituted of a mechatronic platform for the automatized indentation of rubber samples and of a haptic display (a vibro-tactile glove) for the remote transmission of vibro-tactile information, [11]. Using a two-alternative forced-choice (2-AFC) psychophysical protocol, we evaluated the reliability of this wearable haptic system in delivering stiffness information about remote objects in real-time.

3.2.2 Materials & Methods

Experimental Setup

The experimental setup was composed of two main subsystems, which allowed for the execution of the experiments in telepresence. The first sub system was a mechatronic platform for the indentation of samples of different rubber surfaces. It consisted of a Cartesian manipulator with three translational degrees of freedom, a load cell

for the measurement of the normal force during the indentation of the samples (Nano 43, ATI Industrial Automation, Apex, NC, USA), a probe mounted on the load cell and a Graphical User Interface (GUI) made in LabView (National Instruments Corp., Austin, TX, USA) in order to control the movement of the sliders and acquire data from the load cell (Figure 51A). This first subsystem was located in a laboratory of The BioRobotics Institute of Sant'Anna School of Advanced Studies—Pisa, Italy. The second sub-setup was located in a remote environment with respect to the indentation platform, i.e., a laboratory within the Trinity College Institute of Neuroscience in Dublin, Ireland. The apparatus comprised a textile glove equipped with two vibro-tactile piezoelectric elements which were placed on the index and thumb fingertips respectively, a control electronics and a GUI made in LabView, which allowed the transmission of data from the mechatronic platform to the haptic glove (Figure 51B). The communication between the two blocks of the experimental setup was performed via a User Datagram Protocol (UDP) channel. The mechatronic platform for the automatic indentation of the rubber samples (Figure 51A) allowed for the investigation of the participants' discrimination thresholds in the experimental condition of passive touch, with the purpose of characterizing relevant psychophysical parameters. The platform allowed for the measurement of the normal force (F_Z) generated during the rubber compression stage. In particular, it executed indentation protocols with controlled testing velocities and positions, and selectable force targets. The vertical element of the slider mechanism was a precision positioner, and could ensure the vertical application of loads up to 10 kg along the z-axis. The couple of sliders along the x- and y-axes had the same performance as the vertical positioner. The probe was fixed to the load cell: it was a cylindrical tip made of aluminium with a diameter of 6 mm. During the indentation of the rubber samples, the vertical slider was driven with a constant velocity of 0.5 mm/s, which was always the same for each investigated specimen. The choice of a constant indentation velocity allowed us to characterize the stiffness of the samples without taking into account variations due to the viscoelastic behaviour of the materials. In each experimental trial, the rubber pair, the force and the duration used to indent each rubber sample were randomized, in order to guarantee a very challenging task for the participants during the experimental protocol. The tactile feedback system allowed for the vibro-tactile

stimulation on the remote user's hand, giving information regarding the stiffness of the indented rubber samples (Figure 51B). It was composed of an electronic board (sbRIO 9636, National Instruments Corp., National Instruments, Austin, TX, USA) for the communication between the received force signal and the piezoelectric elements in the glove; a piezoelectric evaluation module (DRV2667 Evaluation module, Texas Instruments, Dallas, TX, USA) for the activation of the piezoelectric transducers; a vibro-tactile interface for bi-digital stimulation, made of a textile glove embedding two piezoelectric disks (7BB-12-9, MuRata, Kyoto Prefecture, Japan) encapsulated in a polymeric matrix with a customized process, [11], [212]. The mechatronic platform moved the rubber samples in order to indent those selected for the current experimental session. The six rubber samples were placed on a Delrin support (170 × 130 × 17 mm^3) provided with six housings (30 × 30 × 3 mm^3). The position of the centre of each sample was represented by a couple of coordinates (x-y). These coordinates were randomized with a GUI made in LabView, which allowed for the movement of the horizontal sliders along the x-y axes. Once the target x-y position was reached, the translation mechanism allowed indenting the rubber via the probe along the z-axis. The rubber compression lasted until the measured F_Z on the load cell reached a random threshold level, that was varied in the 4 to 8 N range during the experimental protocol. Once the threshold was reached, the loading phase was interrupted, and the support returned to the reference position (x = 0; y = 0; z = 0).

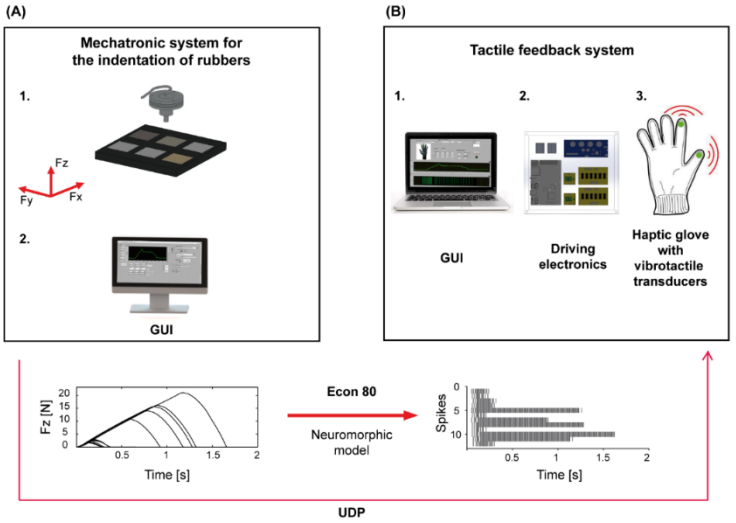

Figure 51: Experimental setup. (A) Subsystem I: 1. Sliders system with load cell and probe for the indentation of the rubber samples at controlled velocity; 2. Interface for the control of the platform operation and for sending data from the load cell to the second environment (remote laboratory); (B) Subsystem II: 1. GUI for the activation of the glove; 2. Driving electronics; 3. Haptic glove for the bi-digital stimulation of the hand. The two sub-setups were spatially separated, since the former was located in Italy and the latter in Ireland. The plots at the bottom of the figure depict how the normal force readings are converted into spikes by means of the implemented Izhikevich artificial neuron model.

Spike-Based Encoding of Cutaneous Feedback Information via the Izhikevich Model

The activation of the piezoelectric transducers on subsystem II was triggered by a spiking neuron model which converted the normal force measured by the load cell on subsystem I (Figure 51) into spike trains. The implemented neuromorphic feedback strategy was based on a regular Izhikevich spiking model, where and represent the neuron membrane potential and recovery variable, [245] (see (16)–(19) of the model). The Izhikevich spiking model was implemented via a GUI made in LabView (National Instruments). The parameters of the model were selected with a pilot evaluation to define a set of coefficients able to convert the measurements of the load cell into a train of spikes reflecting the magnitude and rate of change of the interaction force F_Z arising between the probe and the rubber samples $F_{th} = 0.08\ \mathrm{N}$; $A = 0.04\ \mathrm{mS^{-1}mV^{-1}}$; $B = 5\ \mathrm{ms^{-1}}$; $C =$

$140\ \mathrm{mVms^{-1}}$; $a = 0.02\ \mathrm{ms^{-1}}$; $b = 0.2\ \mathrm{ms^{-1}}$; $c = 65\ \mathrm{mV}$; $d = 8\ \mathrm{mV}$; $V_{th} = 30\ \mathrm{mV}$; $k = 10\ \mathrm{mVms^{-1}N^{-1}}$).

$$\text{If } (F_z - F_{th}) > 0, \text{ then } F_{in} = (F_z - F_{th}), \text{ else } F_{in} = 0 \quad (16)$$

$$\frac{dv}{dt} = Av^2 + Bv + C - u + kF_{in} \quad (17)$$

$$\frac{du}{dt} = a(bv - u) \quad (18)$$

and the after-spike resetting conditions:

$$\text{if } v \geq V_{th}, \text{ then } \begin{cases} v \leftarrow c \\ u \leftarrow u + d \end{cases} \quad (19)$$

Figure 52 shows some examples of how rubber samples were combined during the psychophysical testing (see Table 6 for selected combinations).

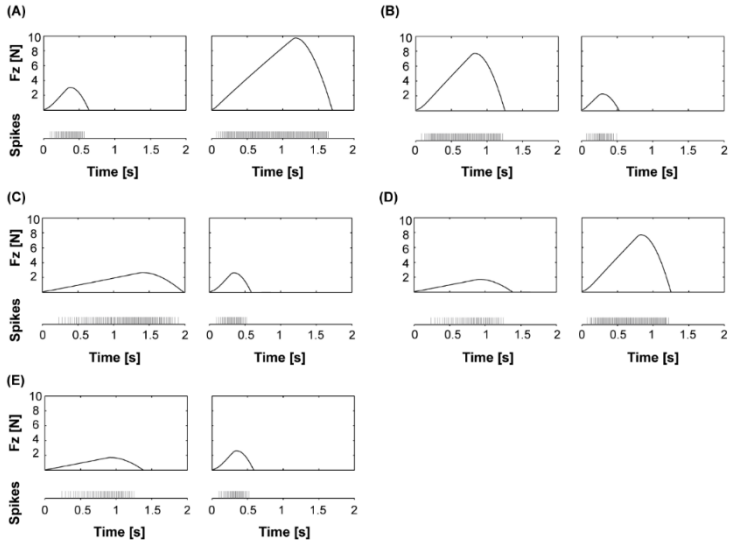

Figure 52: Example combinations of stimulus pairs presented in the experimental protocol. In each experimental trial, the rubber pair, the force and the duration used to indent each rubber sample were randomized, in order to guarantee a very challenging evaluation condition. The panels of this figure show some selected stimulation conditions. (A) Material 1 slightly stiffer than material 2: softer rubber sample indented with higher force (resulting in longer stimulation duration for the softer rubber sample); (B) Material 1 slightly stiffer than material 2: stiffer rubber sample indented with higher force (resulting in longer stimulation duration for the stiffer rubber

sample); (C) Material 2 stiffer than material 1: both rubber samples indented with the same force (resulting in longer stimulation duration for the softer rubber sample); (D) Material 2 stiffer than material 1: indentation duration kept constant (resulting in stiffer rubber sample being indented with a higher force); (E) Material 2 stiffer than material 1: softer rubber sample indented with longer duration (resulting in lower level of indentation force for the softer rubber sample).

Table 6: Normalized stiffness variations of the selected pairs of stimuli.

	Stimulus 1	Stimulus 2	Normalized Δstiffness $\frac{2(\text{Stiffness2} - \text{Stiffness1})}{(\text{Stiffness1} + \text{Stiffness2})}$
1	Econ 80	Ecoflex 30	−1.88
2	Pdms	Dragon Skin FX	−1.61
3	Pdms	Dragon Skin 10	−1.28
4	Smooth Sil 950	Dragon Skin 10	−1.04
5	Dragon Skin 10	Dragon Skin FX	−0.67
6	Pdms	Smooth Sil 950	−0.37
7	Smooth Sil 950	Pdms	0.37
8	Dragon Skin FX	Dragon Skin 10	0.67
9	Dragon Skin 10	Smooth Sil 950	1.04
10	Dragon Skin 10	Pdms	1.28
11	Dragon Skin FX	Pdms	1.61
12	Ecoflex 30	Econ 80	1.88

The obtained spikes were then delivered to the glove by means of a piezoelectric driver (DRV2667, Texas Instruments), working in analogue mode, so that the on–off activity of the transducers was regulated by the neuromorphic model, proportional to the

magnitude of the normal force measured by subsystem I. The actuation parameters for the piezoelectric driver in analogue mode were a 40.7 dB gain, a peak-to-peak voltage amplitude of 200 V and a Boost voltage of 105 V. Figure 53 shows example spike train patterns obtained for the rubber samples and indentation forces experimented during the psychophysical protocol.

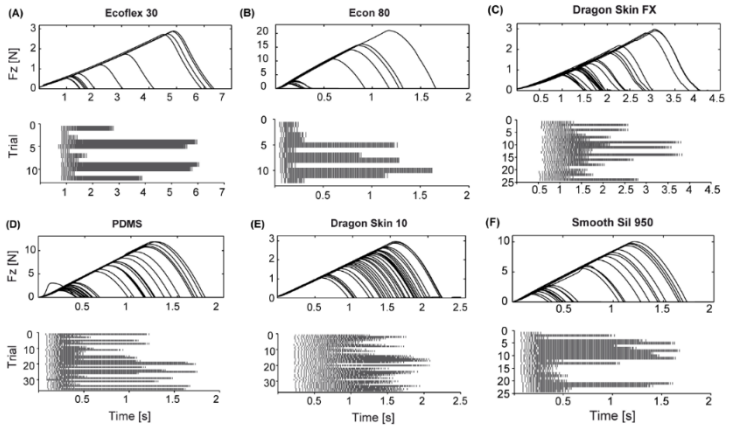

Figure 53: Conversion of the acquired normal forces in spike trains, per each selected rubber. The spikes were then delivered to the wearer of the haptic glove by means of encapsulated piezoelectric transducers. (A) Different indentations of the same rubber (Ecoflex 30) with different force threshold levels (upper panel), and corresponding spike trains per each rubber indentation (lower panel); (B) same of panel (A), for rubber Econ 80; (C) same of panel (A), for rubber Dragon Skin FX; (D) same of panel (A), for rubber PDMS; (E) same of panel (A), for rubber Dragon Skin 10; (F) same of panel (A), for rubber Smooth Sil 950. Spike activity was higher in the middle of the indentation, when the force level reached the threshold. The stimulation patterns shown in this figure were paired and presented to the participant according to the combination possibilities discussed in Figure 3. Note how the spike activity changed passing from a softer rubber (i.e. Ecoflex 30, in panel (A)) to a harder rubber (i.e. Econ 80, in panel (B)). Please note that in panel D (upper panel) there is a single non-coherent slope, probably an outlier of the measured Fz during the automatized indentation protocol.

Psychophysical Experiments

We evaluated the efficacy of the telepresence system in delivering reliable information regarding rubber stiffness using a two-alternative forced-choice (2-AFC) psychophysical protocol. Specifically, a control test was performed investigating an active touch condition naturally with the own hand, while the actual experimental protocol was focused on the investigation of the

communication of stiffness information with neuromorphic tactile telepresence. The two protocols are detailed in the following. An active touch experiment was performed in order to evaluate the benchmark performance of a cohort of participants who actively judged, via their own hand, the stiffness of the same rubber samples used in the telepresence experiment. This experimental protocol regarding active touch involved 10 participants, (five females and five males aged between 23 and 32, recruited from university students and staff of the BioRobotics Institute of the Sant'Anna School of Advanced Studies—Pisa). Participants self-reported having no pathologies regarding the tactile sense, nor was their tactile sensitivity compromised by previous activities. The tactile task involved the index fingertip of the dominant hand (one left-handed and nine right-handed). During the active touch experiment, participants were invited to take a seat and to place their dominant arm on a table. To avoid seeing the stimuli during the experiment, participants were also invited to insert their arm in a box where a cushion was placed for positioning the arm in a comfortable manner, with their palm facing down. During the task, the experimenter inserted in the box the holder containing the selected rubber stimuli, and guided the index fingertip of the participant's dominant hand onto the two selected rubber samples, sequentially. The tactile telepresence experiment involved ten participants (seven females and three males aged between 20 and 31, recruited from university students and staff of the Institute of Neuroscience Trinity College—Dublin). Participants self-reported having no pathologies regarding the tactile sense, nor was their tactile sensitivity compromised by previous activities. The tactile stimulation was performed on the participants reported dominant hand (one left-handed and nine right-handed). The experiment was conducted in accordance with the Declaration of Helsinki, and the protocol was approved by the Ethics Committee for non-clinical experimentation of Sant'Anna School of Advanced Studies Pisa and by the Research Ethics Committee of the School of Psychology, Trinity College Dublin. All participants gave written informed consent. During the telepresence experiment, each participant was invited to take a seat in a remote laboratory (Ireland) with respect to the one where the indentation platform was placed (Italy), and was invited to wear the vibro-tactile glove on the dominant hand. Each participant was asked to wear a

headset which provided white noise in order to mask the sound from the activation of the piezoelectric transducers.

Benchmarking Protocol: Evaluation of the Stiffness of the Rubber Samples under Active Touch

The active touch experimental protocol was carried out for benchmarking purposes to evaluate the physiological acuity in discriminating stiffness variations. It consisted of a 2-AFC tactile discrimination task (Figure 53A). In each trial, the participant was provided with a pair of samples of rubber stimuli, characterized by different stiffness. The participant was asked to touch the centre of each polymeric sample with the index fingertip of the dominant hand. In order to perform the task, the experimenter guided the index finger of the participant onto the first stimulus of the selected pair of stimuli, then rotated the lodging of the stimuli, and guided the finger of the participant onto the second stimulus. The participants were allowed to touch the stimuli as long as they needed and with the force they preferred in order to perceive the rubber stiffness. Participants were asked to provide a verbal evaluation of which stimulus of the presented pair was perceived as stiffer.

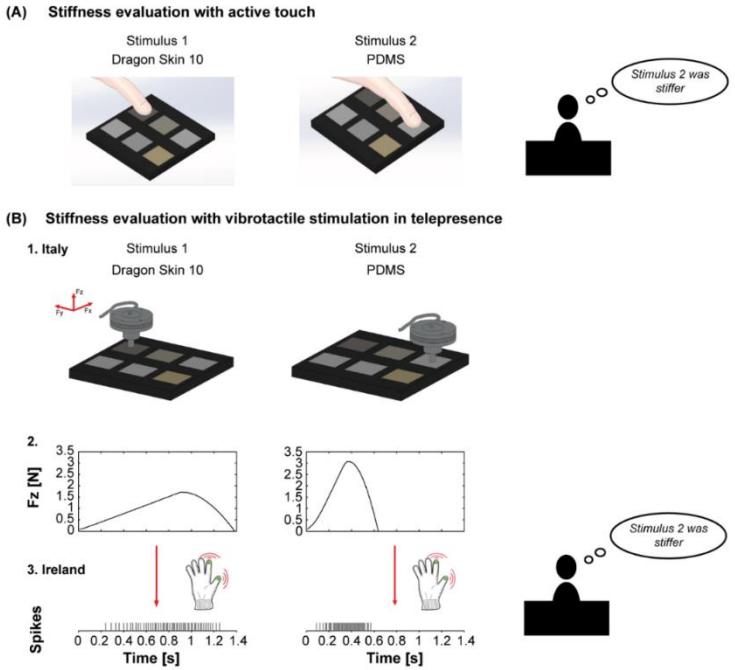

Figure 54: Experimental protocol for psychophysical experiments. (A) Stiffness evaluation with active touch. The participant index was guided towards the selected stimuli of the given couple. After the tactile evaluation, the participant was asked to judge which rubber of the pair was stiffer. (B) Stiffness evaluation with vibro-tactile stimulation in telepresence. 1. The mechanical platform, placed in a laboratory in Italy, indented the selected rubber of the given couple; 2. The measured normal force was converted in spikes using the Izhikevich artificial neuron spiking model; 3. The resulting spikes were delivered to the vibro-tactile glove, placed in a remote laboratory in Ireland, for the haptic bi-digital stimulation of the participants' hand. After the transmission of the spikes representing the second stimulus, the participant was asked to judge which rubber of the pair was stiffer.

For the active touch experiment, seven rubber samples were selected and combined in order to obtain six pairs in which normalized delta stiffness could be equally distributed along the psychophysical axis (see Table 6 for the list and properties of the selected stimuli). In the following analyses, the stiffness variation was normalized according to the mean of the calculated stiffness per each pair (as defined in Table 6), resulting in normalized stiffness variations comprised between 0.37 and 1.88. The experimental protocol consisted in the presentation of the six pairs of stimuli, in

direct and reverse order, for a total of 12 trials (see Table 6). In this way, both the increasing and decreasing stiffness conditions were considered. The whole experiment consisted in the presentation of 72 trials in blocks of 12, with a 5 min break between the third and fourth block. The presentation of 12 trials took about 4 min, for a total duration of the experiment of about 20 min. Before each experimental session, every participant was presented with a training session, in order to familiarize them with the stimuli and the protocol. Each training session was about 5 min long and it consisted of touching all the samples in an increasing order of stiffness. All the participants understood the task with only one training session. A participant's performance during these training sessions was not included in the main statistical analyses since we decided to analyse the data after the candidate was informed about the protocol and the experimental setup.

Experimental Protocol: Evaluation of the Stiffness of the Rubber Samples via Spike-Based Vibrotactile Stimulation in Telepresence

The actual experimental protocol for evaluating the proposed spike-based cutaneous tactile feedback strategy consisted of a 2-AFC tactile discrimination task (Figure 54B). The participant was provided with pairs of vibro-tactile signals in sequence, in which the timing of the vibro-tactile spikes delivered by the glove was linked via the Izhikevich artificial neuron model to the amplitude of the normal force exerted on the load cell during the indentation of the samples, as described in the previous paragraph. The participant was asked to give a verbal description of the perceived vibro-tactile signals, identifying the stiffer rubber of the given pair of stimuli. In the telepresence task the participant received the stimuli fully under the control of the remote mechatronic platform, without the possibility to feel the pair of stimuli again. Before an experimental session, each participant underwent a training session, in order to familiarize them with the stimulation apparatus and procedure. Each training session consisted of the presentation of six randomized trials, also provided in reverse order, for a total of 12 trials (Table 6). The trial session was about 15 min long. The performance of participants during these sessions was not included in the statistical analyses. The whole experiment consisted in the presentation of 72 trials in blocks of 12, with a 5 min break between the third and fourth block in order to ensure concentration and avoid distress. In comparison with the

active touch benchmarking protocol, the speed constraints of the mechatronic platform in the indentation of the stimuli, as well as in the transitions between the stimuli in a pair, enlarged the time required for the presentation of 12 trials, which took about 15 min. The duration of the total experiment was about 1 h and 30 min.

DATA ANALYSIS

Data analysis was performed using the Statistics Toolbox in Matlab (R2016b, MathWorks, Natick, MA, USA). For each stiffness variation, the success rate was evaluated across the population of participants, together with the 95% confidence interval (*binofit* test) of the rates of identification of stimuli with increasing stiffness(normalized Δstiffness> 0). A logistic fit of the resulting psychometric curves was computed for the presented stiffness variations using the Matlab *nlinfit* function, using a custom fitting cumulative distribution function. The significance of participants' responses for each normalized stiffness variation (normalized Δ stiffness) was computed using the Matlab *binofit* test.

3.2.3 Results & Discussion

Psychophysical Tests In the benchmark active touch experiment, we evaluated the capability of the human fingertip to perceive stiffness variations across pairs of rubber stimuli. To do so, experiments were performed according to a 2-AFC experimental protocol, with a sample of 10 volunteers. In the active touch condition, the discrimination performance was above 95% for all the stiffness variations, except for the stimulus closest to the origin, for which the stiffness variation was small (*e.g.,* the pair PDMS/Smooth Sil 950 as showed in Table 6). The discrimination of each rubber stiffness by the active touch volunteers showed an average 90 ± 2% of correct responses over the whole range of stiffness variations (Figure 55A). In the telepresence experiment, we assessed how the spike-based stimulation delivered through the glove enabled a sensory feedback for the stiffness of the rubber samples. A 2-AFC experimental protocol was used with a sample of 10 volunteers. The stimulus stiffness was encoded by the temporal pattern of spikes during the vibro-tactile stimulation delivered to the fingers of the telepresence participants. For the telepresence condition, the discrimination performance was above 85% for large stiffness variations. The performance in discriminating the stiffness of the experimented

rubber samples by the telepresence participants showed an overall average of 74±7% (Figure 55A). In both active- and telepresence-touch conditions, all stiffness variations were identified significantly better than by chance (probability of success > 50% in a *binofit* test of 10 participants), except for the first stimulus of the explored range of stiffness variation, for which the stiffness variation was small (Figure 55B,C and Table 6). In both the experimental conditions, the participant's response was given by chance only when the pair with normalized Δstiffness = 0.37 (stimuli of comparable stiffness) was presented. The experimental data were well-fitted by the symmetric logistic cumulative distribution function (CDF) (20), suggested by Ulrich and Miller, [246], over the whole range of stiffness variations inspected in the test configuration:

$$G(x) = 0.5 + 0.5\left[1 + e^{\frac{-x-a}{b}}\right]^{-1} \quad (20)$$

The fitting function denotes the probability of a correct response at difference x, where a represents the perceptual threshold and b > 0 a scale parameter that affects the steepness of the curve. The experimental data were well fitted by the logistic CDF fit over the whole range of stiffness variations (see the black dashed line in Figure 55B,C). According to this model, the perceptual threshold above which participants could discriminate the difference in normalized stiffness of the rubber stimuli was a = 0.64 for the active touch condition, and a = 1.28 for the telepresence condition. The curve relative to the telepresence experiment displayed lower performance in comparison to the one relative to the active touch condition, for normalized Δstiffness > 0.37. The overall difference in performance between the telepresence and active touch benchmark experimental conditions (Figure 55) corresponded indeed to an effect size of 2.1 (corrected Hedge's). This suggests a better performance when the stiffness discrimination task was performed with the same set of stimuli in the active touch benchmark, naturally with the human hand. However, the two logistic fits showed more similar behaviour when normalized Δstiffness was far from the values close to the origin of the psychometric curve (|*normalized Δstiffness*| > 0.67, see Table 6), with the effect size (corrected Hedge's g) of the difference between the two groups being 1.1 for |normalized Δstiffness| = 1.88. Furthermore, considering that in the telepresence

condition the rubber stiffness was converted to vibro-tactile stimulation while both the indentation force and duration were randomized and not a-priori known by the participants, we can state that the telepresence task was more challenging than the benchmark active touch one.

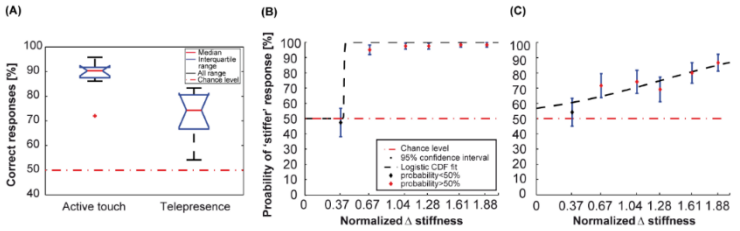

Figure 55: Psychophysics results of telepresence experiments. (A) Boxplot of correct responses for the two experimental conditions. Boxes represent interquartile range and black dashed lines show the complete range across participants. The red dashed line represents chance level; (B) Psychometric curve for the psychophysics experiments with active touch. Each dot represents the fraction of times each stimulus was classified as having increasing stiffness (median across participants). If the identification rate is significantly different (probability of success>50%, binofit test) from chance (50%) the dot is red, otherwise it is black. Errorbars indicates the 95% confidence interval across participants and the red horizontal line represents chance. Black dashed line represents the logistic CDF fit; (C) Same as (B) for the psychophysics experiments in telepresence.

CONCLUSIONS

The goal of the present work was to evaluate the capability of a haptic system, a vibro-tactile glove, in delivering reliable information about rubber stiffness in a telepresence configuration using a neuronal spiking model to trigger the delivery of stimuli. We investigated this topic using customized piezoelectric transducers embedded in a textile glove for the simultaneous stimulation of index and thumb fingertips. In order to do so, we compared the results from the vibro-tactile stimulation of the hand with the benchmark experimental data relative to the active exploration of the rubber stimuli performed with the index fingertip. We analysed the reliability of a telepresence system in delivering, directly on the skin of a remote hand, haptic information about the stiffness of selected polymeric samples. The stimuli were indented by an automated system and their stiffness encoded according to a neuronal spiking model heuristically adapted from our previous implementations that emulate the firing activity of human mechanoreceptors, [86], [147], [148]. This approach has some analogies with what has been termed

contingency-mimetics, that applies biomimicry at the level of the sensory organ instead of the nerve, [242]–[244]. We showed that the application of spike-based vibro-tactile stimuli on the hand enabled the remote discrimination of most of the selected pairs of stimuli characterized by different stiffness. The stiffness discrimination performance was achieved by means of the proposed spike-based encoding of tactile information and was compared with that obtained via direct active touch exploration. During active touch exploration, participants were allowed to directly touch the rubber stimuli with no restrictions to the force and the duration of the contact, that were under human voluntary control. In the very challenging telepresence conditions created according to the indentation protocol, the indentation force and the duration of the contact were completely randomized and not known to the participants. We acknowledge the several differences between the two experimental conditions: the time taken by the task (20 min for the active task vs. 90 for the telepresence task), the active vs. passive approach, the auditory masking (absent in the active task), and the control of the force and indentation velocity for the telepresence vs. no control in the active task. Despite this, with our work we aimed at demonstrating the proof of principle of a telepresence task, where tactile feedback can be representative of object characteristics (*i.e.,* stiffness). Therefore, we preferred to design our experiment so that the proposed method was assessed in more challenging conditions than the natural benchmark. This study will be complemented with future research where participants will actively control a robotic arm in immersive telepresence, mimicking an active industrial task while receiving tactile information about the robot contact forces and displacement, whereas with typical virtual-reality-based human–machine interfaces the human operator can hardly recognize states when the robot has established contact with the objects in its environment. In order to deepen the explanation of the physical determinants of the responses given by the participants, we calculated the average inter-spike interval (ISI) for each rubber stimulus in the initial phase of the stimulation (calculated in a window of 120 ms after the first spike, that guarantee at least three spikes to be considered per each stimulus; see raster plots in Figure 53). Though with non-perfect separation between different rubber samples, the analysis demonstrated an inverse correlation between the ISI and the stiffness (Table 7; Figure 56), meaning that stiffer

stimuli result in lower ISI (or more compliant ones result in higher ISI). This is because the force varies in a steeper manner in a stiffer stimulus while being indented at a constant velocity. A complementary analysis to investigate the psychophysical results was the estimation of the normalized ISI variation (defined as the normalized stiffness variation; see Table 6) as a function of the normalized stiffness variation within each pair of stimuli experimented via the developed neuromorphic haptic interface (Figure 57): a monotonic trend can be appreciated, however very low normalized Δ ISI were achieved at low normalized Δ stiffness. This explains the non-significant discrimination of the developed neuromorphic haptic interface while being used to remotely touch rubber samples with similar stiffness (see Figure 55C). Accordingly, future improvements of the system should aim at tuning the coefficients of the differential Equations (3)–(6) of the developed neuromorphic haptic interface, to amplify the ISI differences particularly with rubber samples of similar stiffness.

Table 7: Correspondence between the stiffness of the experimented stimuli and the inter-spike interval at the onset of the indentation as a result of the implemented neuromorphic haptic encoding strategy.

	Stiffness ± std (N/mm)	Mean ISI ± std (s)
Econ 80	78.9 ± 4.9	0.012 ± 0.001
PDMS	34.5 ± 0.2	0.0179 ± 0.002
Smooth Sil 950	23.8 ± 0.7	0.019 ± 0.002
Dragon Skin 10	7.5 ± 0.1	0.039 ± 0.004
Dragon Skin FX	3.7 ± 0.1	0.041 ± 0.004
EcoFlex 30	2.5 ± 0.1	0.043 ± 0.008

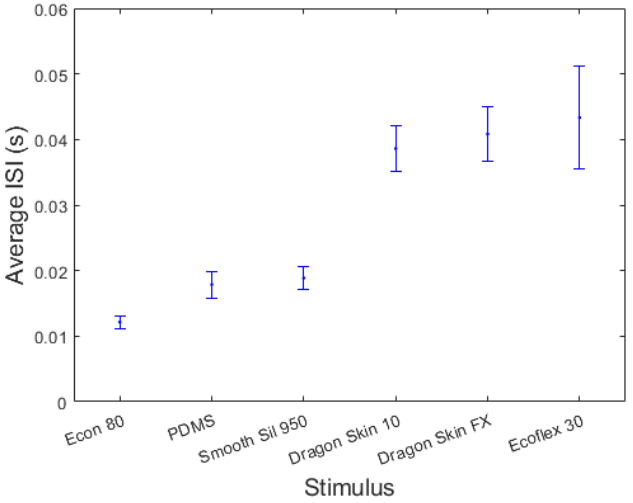

Figure 56: Experimented stimuli sorted from the stiffer to the more compliant, and related inter-spike interval. Error bars show the standard deviation of the inter-spike interval (ISI).

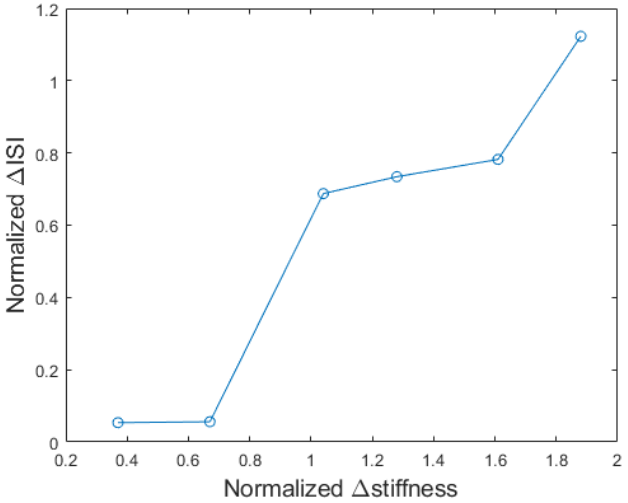

Figure 57: Experimented stimuli sorted from the stiffer to the more compliant, and related inter-spike interval. Error bars show the standard deviation of the inter-spike interval (ISI).

Tactile information provided with haptic devices can partially compensate for a missing sense. Sensory substitution can be fundamental in cases of persons with blindness or visual impairment, deafness or hearing impairment and combined sensory impairment (deaf–blind). In these situations, the information coming from one sensory channel can be conveyed to the tactile sense in a perceptible manner, [173], [174], [177], [216], [224] to allow, as an example, obstacle avoidance in assisted walking or remote communication with vibro-tactile patterns. However, we are also aware of the intrinsic limitations in the possibilities to integrate perceptually (not only cognitively) a substitute sense in the own natural sensory scheme, as discussed in the work of Deroy and Auvray, [225]. Vibro-tactile stimulation can also be widely used in the field of non-invasive feedback in amputees and sensory augmentation for healthy subjects in applications such as virtual reality, gaming, rehabilitation, navigation, rescue and remote control of robots, [192]–[196]. Examples of tactile devices for sensory augmentation providing whisker-type distance information were developed in the shape of head mounted systems, [247]–[249] or belts, [250], [251] to improve navigation, as well as handheld systems for the detection of distances, [251]. Tactile information was proven useful also in industrial environments for human–robot co-working activities. The development of alerting haptic devices, in environments where the interaction with automated machinery can be dangerous for operators, may also improve safety and the adoption of collaborative robotics in common applications. Our tactile device can be classified within state of the art technologies where haptic feedback is used to provide sensory augmentation, with a particular focus on the remote perception of stiffness and potential applications in several fields, including robotic surgery. Our preliminary experimental protocol followed a simplified characterization approach for the rubber samples. Since the stiffness of the specimens was investigated via a constant indentation velocity of the probe, we did not consider variations in dynamic deformation behaviour due to the viscoelastic characteristics of the rubber samples, which is an important aspect for the tactile characterization of a biological tissue. Towards the applicability in robotic surgery scenarios, this study will be complemented with future experiments involving different indentation velocities to investigate the effects of viscoelasticity in

the perception of stiffness. According to the proposed spike-based encoding paradigm, tactile displays installed on robotic manipulators are expected to allow surgeons to feel in real time the stiffness of human tissues, while force information is collected by force sensors installed on the robotic end effectors. The tactile device herein presented is grounded on a novel neuromorphic discrimination mechanism for the recognition of the stiffness of rubber samples. Accordingly, a sequence of vibro-tactile pulses are delivered on the skin surface, resembling the neural spikes produced by the mechano receptive endings underneath. Hence, the proposed strategy for encoding haptic data is non-homologous to physiological perception via the own fingers. The assumptions made in proposing such a strategy for the development of sensory substitution and augmentation devices were very strong. As a matter of fact, tactile devices are based on cognitive discrimination mechanisms, [252] that are slow and require efforts when compared to natural perceptual processes, thus demanding a certain familiarization before allowing the perception of information in a reliable manner, [225]. Physiological perception, achieved with the classical senses, allows the immediate discrimination of sensations, grounded on specialized neuronal architectures and on the training undertaken during the whole past life of a subject, and has important implications for the usability of a device in real-world applications. In this framework, we had evidence that the proposed neuromorphic model enabled the participants in our experiments to perceive the stiffness of materials in an intuitive manner. Further studies are however required to evaluate the degree of embodiment of the provided neuromorphic haptic perception, in comparison to the natural perceptual mechanisms of the somatosensory system. For applications that may encounter some limitations in delivering stimuli to the skin, we envisage the possibility to convert the trains of spikes in audio data. In this respect, a proof of feasibility is provided by electrophysiological experimental set-ups, that typically have loudspeakers or headsets to convert the recorded neural signals into audio data in real-time (with auditory patterns that may help the experimenter in identifying, as an example, a specific neuron type). Moreover, some ongoing initiatives, aiming at converting neural data into pleasant music and rhythms (see, *e.g.,* [253]), provide additional evidence regarding the feasibility of achieving a meaningful auditory representation of spikes, as an alternative to haptic interfaces.

3.3 Haptic glove and platform with gestural control for neuromorphic tactile sensory feedback in medical[8]

3.3.1 Framework

MOTIVATION AND CHALLENGE DEFINITION

The impact of haptic devices has grown tremendously over the last decade, [254]–[256]. These devices connect the user to a virtual object, providing tactile feedback directly to the human skin. Through the sense of touch humans are able to gather a wide range of information about the surrounding environment. Thus, the delivery of tactile information is crucial for sampling objects, in particular when they are occluded from sight. Haptic devices pave the way for most of the telepresence applications based on the sense of touch as a communication channel. However, if compared to the advanced technologies that are available commercially to convey vision and auditory information with a very high level of fidelity, tactile telepresence technologies are still in a pioneering phase. The present study addresses this challenge with specific reference to potential applications in medical robotics, by proposing a marker less gesture-based controller of a mechatronic platform with tactile sensory feedback delivered to a user seeking remote buried nodules. This task is selected as a benchmarking reference of the developed system because palpation is a very important practice in medical diagnosis and surgical intervention.

RELATED WORK AND STATE OF THE ART

The development of technologies inspired by the study of human sense of touch is being contributed to by the integration of several research fields, such as biomedical engineering, robotics and bio-robotics, measurement and instrumentation, computer graphics, cognitive science, neuroscience, and psychophysics. Research on human tactile sensing has characterized the role of functionally diverse skin receptors, [1], [66], [232], [257], densely populating the fingertips (up to hundreds of units per square centimetre). Biologicalmechanoreceptorsallowforahighresolutionofsensedinformation,andencode a wide range of temporal and spatial stimulations,

[8] This section has been excerpted from the paper, [285], that has been published in an international scientific journal: Sensors, with the PhD candidate being first author (with equal contribution) of the study.

[104], [173], [209], [210]. Artificial tactile sensors and haptic interfaces are the two parts (remote and close to the operator, respectively) of a tactile telepresence application. Considering the development of tactile sensors and artificial skins, [57], [258], applications of tactile sensing include tactile-based material recognition, [259], [260], tactile based object manipulation, and slip detection, [261]–[263]. Haptic devices could contribute to the performing of different tasks in various scenarios: in rehabilitation procedures, to develop tactile aids for visual and auditory sensory disabled persons, [175], [221], [264]–[266]; and in telepresence operations, to improve user perception capabilities through vibro-tactile feedback, [192], [193], [195], [196], [267]. Beyond these applications, tactile technologies employed in telepresence and teleoperation scenarios have been widely used in the field of minimally invasive surgery (MIS) and robotic minimally invasive surgery (RMIS), to overcome the absence of both tactile and force feedback conveyed to the physician. Feedback is crucial for helping the surgeon to preserve healthy tissues, as well as for detecting differences in stiffness throughout the palpated sites, [7], [194], [235]–[237], [239], [240]. Despite the growth in recent interest and research, the degree of maturity of touch sensing is still lagging behind that of other perceptive technologies, such as audio or computer vision, [14], [268]–[272][36–41]. A plausible explanation is in the biological complexity of the sense of touch, where the distributed sensitized region covers the entire body, [273], while other human senses have localized sensitive areas. In a previous work, [136], we developed a mechatronic platform interfaced with a vibro-tactile glove for tactile augmentation in telepresence under passive exploration of remote stimuli. The results demonstrated the efficiency of the system in presenting mechanical information about test objects. The stiffness of different materials, converted into spikes with proper frequency through a neural model, was used to drive piezoelectric disks embedded in the index and the thumb of a vibro-tactile glove. The designed psychophysical protocol for discriminating stiffness, tested with 2-Alternative Forced Choice passive touch, unveiled specific perceptual thresholds, derived using the Ulrich–Miller Cumulative Distribution Function. Although passive touch conveys information about the miscellaneous properties of the explored object, an active exploration permits enrichment of the tactile signals, thanks to integration with the proprioceptive inputs,

[274]–[276]. Remote tele-palpation under active touch with gesture-based control and spike-based feedback is the objective of the present study.

Contribution of the Present Study

Building on the findings of the previous study, here we propose a telepresence system with active exploration of a silicon phantom that embeds elements with different stiffness within. In this condition, the user can directly control and move the indenting platform, with an additional optical sensor for tracking the hand movements. We investigated two experimental conditions of telepresence: (*i*) ILS, where the platform was placed In Line of Sight of the user, [12]; (*ii*) NILS, where the platform was Not In Line of Sight, in a different location with respect to the user, for a more challenging task. Hence, the objective of the present study is to investigate the mechanisms of tactile perception under active gestural control and the effectiveness of the proposed spike-based feedback strategy. In particular, the delivered vibro-tactile feedback mimics the language of tactile receptors, generated by a neuromorphic model, [4], [148], [277]. The present work is organized as follows: Section 3.3.2 is partitioned into *(i)* Experimental Setup; *(ii)* Platform and Inclusions Characterization Protocols; and *(iii)* Psychophysical Experiments sub-sections. In these sections, the telepresence system with the related two sub-systems and the used phantom are described and details about the performed characterizations and the performed protocols are given. The results, the discussion and conclusions of the present study are reported in Section 3.1.3

3.3.2 Materials & Methods

Experimental Setup

The experimental apparatus was composed of two essential sub-setups, positioned at a proper distance for achieving telepresence conditions (Figure 58A).

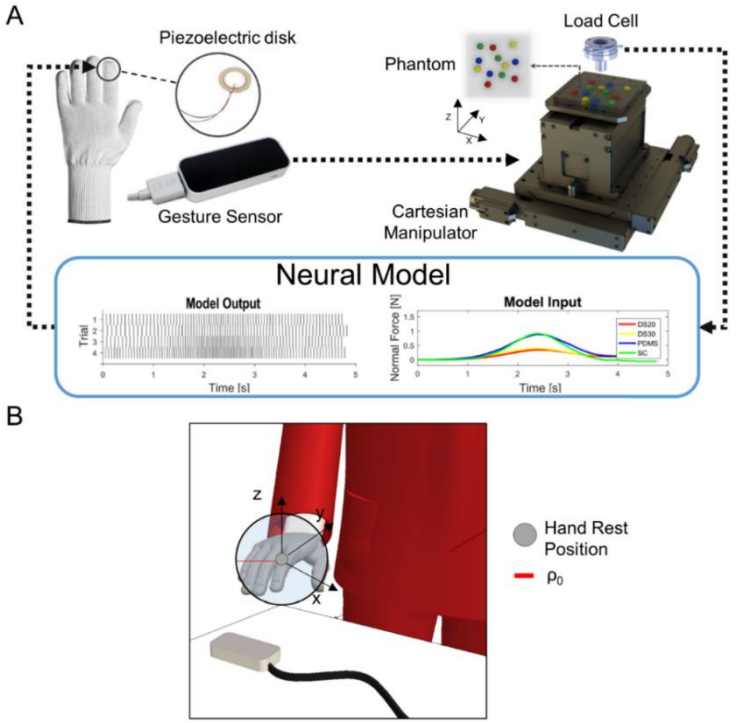

Figure 58: Experimental apparatus. (A) Left: the haptic sub-system comprising a textile glove with a detail of the encapsulated piezoelectric disk for index fingertip vibro-tactile stimulation and optical sensor for hand gesture tracking; right: tactile sub-system comprising a 3-axis Cartesian manipulator with load cell and the indenter, and a detail on the silicon phantom displaying nodules placement. The two sub-setups were spatially separated to achieve Line of Sight (ILS) and Not In Line of Sight (NILS) telepresence conditions. The plots at the bottom of the figure show the neural encoding of the normal force arising during the sliding phase of the phantom into spike trains for all the polymers, from the softest (red) to the hardest (green). (B) Details about the reference coordinates of the gesture

The first sub-setup consisted of a piezoelectric disk (7BB-12-9, MuRata, Kyoto Prefecture, Japan) encapsulated in silicone rubber, with a customized process, which was placed on the index fingertip of a textile glove to deliver the feedback, [11]. An optical sensor (Leap Motion, CA, USA) tracked the user's hand gesture. We defined as haptic sub-system this first sub-setup located in a laboratory of The BioRobotics Institute of Sant'Anna School of Advanced Studies, Pontedera (Pisa, Italy). A graphical user interface (GUI) was

developed using LabVIEW (National Instruments Corp., USA) for acquiring speed and position of the hand's centre of mass, handling communication with the other remote sub-setup, and recording hand position data. We defined as tactile sub-system, the second remote sub-setup used for the exploration of the phantom. This platform included: a Cartesian manipulator (X–Y and Z, 8MTF-102LS05 and 8MVT120-25- 4247, STANDA, Vilnius, Lithuania); a 6-axis load cell (Nano 43, ATI Industrial Automation, Apex, USA) to measure contact forces between a customized indenter with a spherical tip of 3 mm radius, mounted on the load cell; and the phantom during the active sliding. A second GUI was designed for real-time control of the motorized stages and data communication. In the ILS session, the tactile sub-system was placed near the user to perform experiments in stream lined telepresence. In the NILS session, instead, it was located in a remote laboratory in Florence, Italy, which was about 50 km apart from the haptic sub-system, thus increasing the challenge of the proposed task. Data communication between the two sub-setups was provided through the User Datagram Protocol (UDP) that ensured a maximum latency of 15 ms. The adopted communication protocol allowed bidirectional streaming of data: hand gestures from the haptic sub-system to the mechatronic platform, and normal force from the tactile sub-system to the glove to be encoded and then delivered (Figure 59).

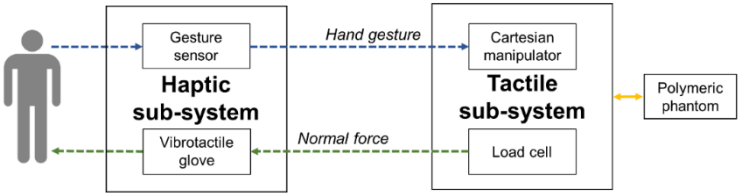

Figure 59: Block diagram: bidirectional data streaming between the haptic and tactile sub-systems provided via UDP: the optical controller conveyed speed and position of the centre of mass of the user's hand from the first environment to the Cartesian manipulator in the remote one (blue arrow) and, while sliding, normal force data collected by the load cell from the platform to the vibro-tactile glove to deliver the spike-based stimulation (green arrow).

During experiments, the user actively explored and searched for stiffer areas in the polymeric phantom. Four different rubber materials were used to cast 12 hemispherical inclusions (3 replicas of each material), of 5 mm radius, randomly inserted across the X–Y

plane in a silicon cuboidal block, 100×100×15 mm3 in size. The chosen polymers for the inclusions were: Sorta Clear 40 (Smooth-on, PA, USA) as the stiffest, polydimethylsiloxane (PDMS) Sylgard 184 (Dow Corning, USA), Dragon Skin 30, and Dragon Skin 20, while Dragon Skin 10, the softest, was used for the cuboidal block. The platform control during the experimental session was based on the user's hand movements, tracked by the 3-D optical sensor. The infrared light-based gesture sensor used had a field of view of about 150 degrees and a range between 25 and 600 mm above the device, and it showed proper performance when it had a high-contrast view of the hand to be detected and tracked. Therefore, the device was placed just below and close to the rest position of the user's hand, and the workspace was set according to the specifications of the gesture sensor. Details about the reference coordinates of the gesture sensor, highlighting the rest position and volume, are shown in Figure 1B. As the user's hand moved out of this volume, the motorized stages followed along the same direction at a speed proportional to the displacement of the user's hand. The assigned speed was calculated using the difference $\rho - \rho_0$, where ρ was the distance between the hand centre of mass and the centre of the sensor, and ρ_0 was the radius of the neutral spherical region, set to 50 mm. The user was provided with visual feedback about the position of the indenter on the phantom in the remote environment, without any information on the location of the inclusions. The contact between the indenter tip and the polymeric test object generated a force. To avoid mechanical damage to the phantom and load cell due to the user's upward movement, a force threshold (0.5N) was introduced. The measured force was sent to the haptic sub-system to been coded into spike patterns, which triggered the piezoelectric actuator. We implemented a neuromorphic feedback strategy based on a regular Izhikevich spiking model discretized using Euler's method at 5 kHz, [245]. The chosen model efficiently encodes the temporal dynamics of a mechanoreceptor including the biological plausibility of the computationally intense Hodgkin–Huxley model, [278] and the computational efficiency of the integrate-and-fire model, [279]. The neuromorphic activation of the transducer was achieved by setting the input to the neuron proportional to the magnitude of the normal force measured by the remote subsystem. Further details about the neural model and a definition of its parameters can be found in our previous works, [136]. Initial

calibrations were also performed to counterbalance the effect of saturation of the neural model, [12]. The spikes generated by the Izhikevich model were sent to the vibro-tactile glove by means of a piezoelectric driver (DRV2667, Texas Instruments). This driver facilitated the setting of the actuation parameters in analog mode to have a gain of 40.7 dB, 200 V peak-to-peak voltage amplitude, and 105 V offset voltage.

Platform and Inclusions Characterization Protocols

A characterization protocol was performed aiming at assessing the uncertainty of the apparatus in tracking and reproducing the user's hand pose. Five subjects (4 men and 1 woman between 28 and 30 years of age), enrolled among the staff of The BioRobotics Institute of Sant'Anna School of Advanced Studies, took part in the experiment. They were asked to drive the stages of the platform in order to perform a set of target trajectories within the X–Y Cartesian plane. The target trajectory and the subject's relative position on this plane were part of the GUI providing visual feedback in the haptic sub-system. The cluster consisted of 2 square-shaped (s1= 60 mm and s2 = 30 mm, in length) and 2 circular (r1 = 30 mm and r2 = 15 mm, in radius) trajectories, which had to be followed 3 times by each subject, starting from their centres. Deviations in the trajectories, used to evaluate the system in terms of performance, were calculated using the area comprised between the perimeter of the target and executed trajectories, by means of the boundary function (MATLAB, The MathWorks, Inc., Natick, Massachusetts, USA). The error rates between the tracked area and target were calculated as their ratio and are reported in Section 3.3.3. Moreover, before involving human subjects, the phantom was mechanically characterized to assess the vertical stiffness ($\Delta F_Z/\Delta z$) of the nodules and the surrounding soft material by means of the proposed platform equipped with a flat indenter. The adopted experimental protocol consisted of 5 trials in which the entire set of inclusions experienced an indentation at a fixed force threshold (F_Z = 0.5 N) and speed (v = 0.125 mms^{-1}). To estimate the stiffness of the investigated polymers, the vertical component of the force collected during each compression was processed through scripts in MATLAB and results of such a characterization are reported in Section 3.3.3.

Inclusions Identification Experimental Methods

Psychophysical experiments were performed to validate the proposed system for delivering stiffness information about the palpated nodules in both ILS and NILS tactile telepresence conditions. The experiments involved 10 participants (7 men and 3 women between 24 and 33 years of age) in ILS, and 15 (9 men and 6 women between 25 and 37 years of age) in NILS, enrolled among the university students or staff of The BioRobotics Institute of Sant'Anna School of Advanced Studies, Pisa, Italy. The participants took a comfortable posture at the control workstation in the laboratory, where the haptic sub-system was located. They wore the vibro-tactile glove on their dominant hand and a headset to eliminate environmental noise. To familiarize participants with the driving of the tactile platform, each participant took part in a fifteen minute training session. Moreover, this preliminary task got the users accustomed to the vibro-tactile signal exerted by the piezoelectric actuator of the glove. Answers provided during the training sessions were not included in the analysed results. Both ILS and NILS psychophysical experiments consisted of a tactile identification task: within six minute time-period of the protocol, the participants unreservedly explored the silicon block and pressed a button on a keyboard on any occasion of perceived frequency variation in the vibro-tactile feedback. The performances of the participants were evaluated in MATLAB in terms of rate of correct identification of the inclusions, using parameters calculated for both ILS and NILS populations and for each participant. Specifically, we evaluated: (a) the number of true positives (TP), (b) the number of false positives (FP), and (c) accuracy (TP/P, with P = collected responses—FP). These parameters were computed as a function of the center-to-center distance between the position of the perceived inclusions and the nearest actual inclusion. If the perceived position was felt to be within a radius of 10 mm from the centre of the nearest inclusion (i.e., the distance was equal to the diameter of the inclusion), the perceived inclusion was classified as TP; otherwise it was classified as FP. The classification of collected responses was also evaluated for a lower tolerance, 5 mm, and two greater ones, 15 mm and 20 mm. A logistic fitting, using a Cumulative Distribution Function (CDF) [56] and the *nlinfit* MATLAB function, was performed for each material to carry out the rate of correct perception and the perceptual thresholds for both the investigated experimental conditions.

3.3.3 Results & Discussion

3.1. Platform and Inclusions Characterization Results In the platform characterization, the trajectories followed by each user for individual tests are shown in Figure 60. The target areas, the tracked areas, their difference, and the error rates for all the presented trajectories are reported in Table 8 in terms of mean and standard deviation amongst subjects. Based on the user's gestures, the platform was able to easily follow square geometries (error rate lower than 5%) as well as circular trajectories (but with higher average errors, comprised between 5% and 13%, being the task more challenging than tracking square geometries). The error rate increased with the area being explored, presumably due to non-constant spatial resolution of the gesture-sensor.

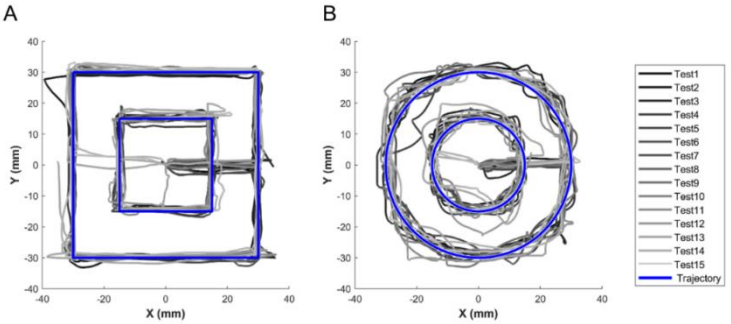

Figure 60: Graph highlighting target trajectories (blue lines) and tracked trajectories (grey lines) within the X–Y Cartesian plane: (A) square shaped; (B) circular shaped. The grey lines starting at the origin represent the path to reach the target trajectories.

Table 8: Results from characterization of the apparatus

n = 15	**Square (s_1 = 60 mm)**	**Square (s_2 = 30 mm)**	**Circle (r_1 = 30 mm)**	**Circle (r_2 = 15 mm)**
Target Area (mm^2)	3600	900	2827.43	706.86
|Tracked Area – Target Area| (mm^2) ($\mu \pm \sigma$)	74.05 ± 65.79	43.27 ± 40.99	143.90 ± 121.28	91.74 ± 89.82
Error Rate (%) ($\mu \pm \sigma$)	2.01 ± 1.83	4.81 ± 4.55	5.09 ± 4.29	12.98 ± 12.71

the phantom characterization, the stiffness of each material was measured by assuming the polymers had a linear response in the range of applied forces. According to the operated characterization, the stiffer materials were Sorta Clear (3.69 $N \cdot mm^{-1}$) and PDMS (3.68 $N \cdot mm^{-1}$), while Dragon Skin 30 (2.88 $N \cdot mm^{1}$), Dragon Skin 20 (2.74 $N \cdot mm^{-1}$), and Dragon Skin 10 (2.14 $N \cdot mm^{-1}$) showed lower values (Figure 61).

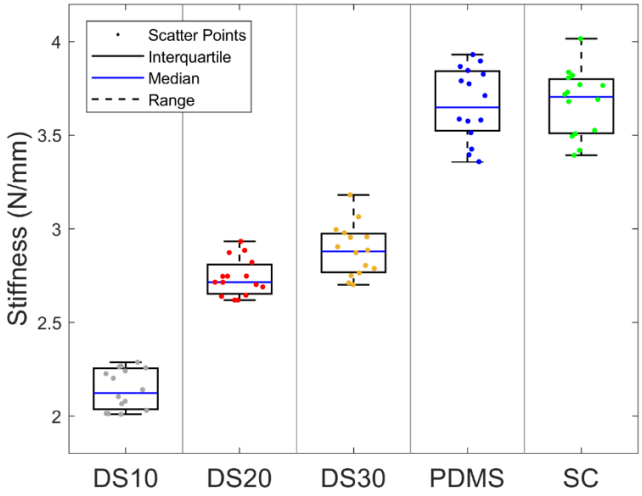

Figure 61: Mechanical characterization of the phantom: scatter points are the stiffness values collected for each material (Dragon Skin 10—DS10; Dragon Skin 20—DS20; Dragon Skin 30—DS30; polydimethylsiloxane—PDMS; Sorta Clear 40—SC) across the five trials of indentation; boxes represent interquartile ranges for the five materials; blue lines show the median values and black dashed lines the full ranges among the measured

Inclusions Identification Experimental Results

In the psychophysical experiments with tactile feedback in ILS and NILS telepresence conditions, we successfully delivered a neuromorphic stimulation encoding the stiffness of the tele-palpated phantom. The inclusions recognized by the user were recorded with a key press. An example of the path followed and the responses are shown in Figure 62.

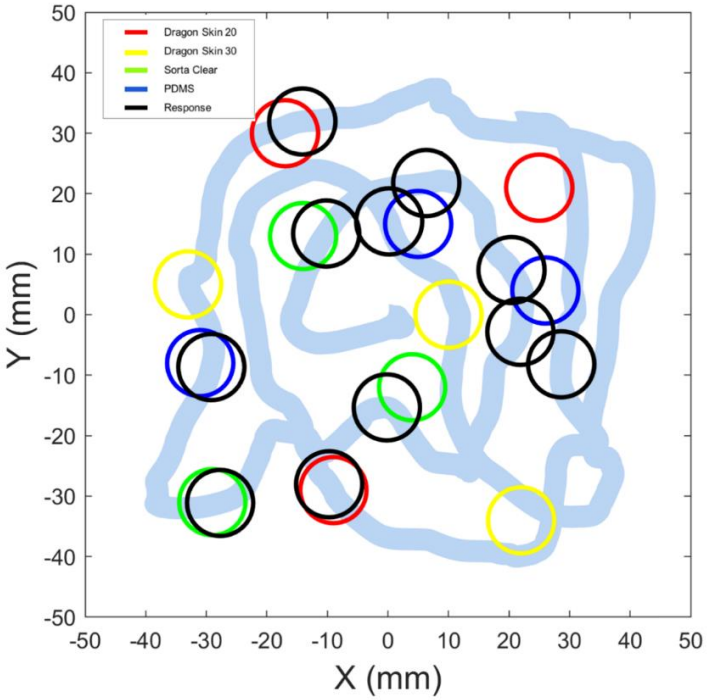

Figure 62: Example of responses given by a participant across an experimental session: coloured circles mark the position of the inclusion set; black represent the position of the indenter when the subject pressed the key, and light blue line represents the trail of the probe on the phantom surface.

Results show that an average of 63% and 60% of the inclusions were correctly perceived and declared within a tolerance of 10 mm to the nearest inclusion, for ILS and NILS experiments, respectively. In both cases, with a tolerance higher than the inclusion diameter (*i.e.,* >10 mm), the rate of identified inclusions was slightly higher (Figure 63).

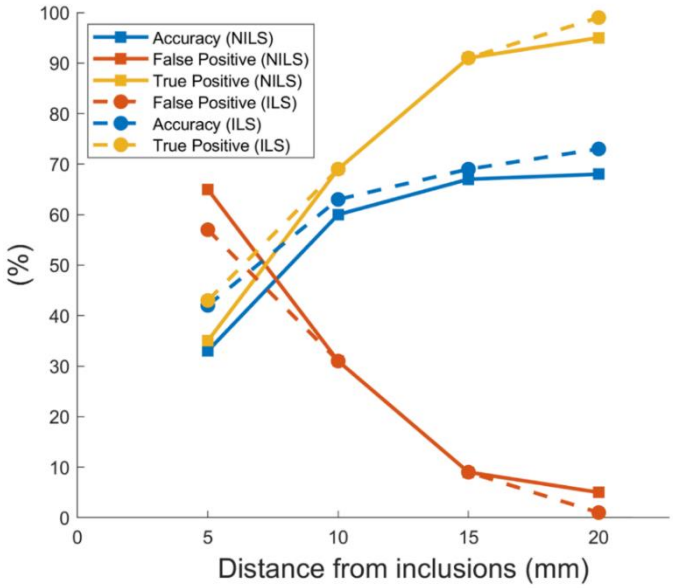

Figure 63: Tolerance of recognized inclusions: each (dots for ILS and squares for NILS) represents the mean accuracy (blue line), mean false positive (red line), and mean true positive (yellow line) responses evaluated through a classification based on the admitted centre-to-centre distance between perceived inclusions and the real ones.

The identification rate for all the participants, across populations, was evaluated for each material and is presented in Figure 64 with increasing stiffness along with the interquartile range (IQR) for the accuracy of declared inclusions. Performance, in terms of correct identification of inclusions, was 65% and 70% for stiffer stimuli including both populations. The minimum accuracy in perceiving the inclusions with lower stiffness was found to be 52%, with the exception of the softest Dragon skin 20 material in NILS condition, whose rate decreased down to 33%. The global performance of identified inclusions, across all materials, showed an average of 63% and 60%, respectively, for ILS and NILS conditions (Figure 64).

$$G(x) = [1 + e^{-x-a/b}]^{-1} \quad (21)$$

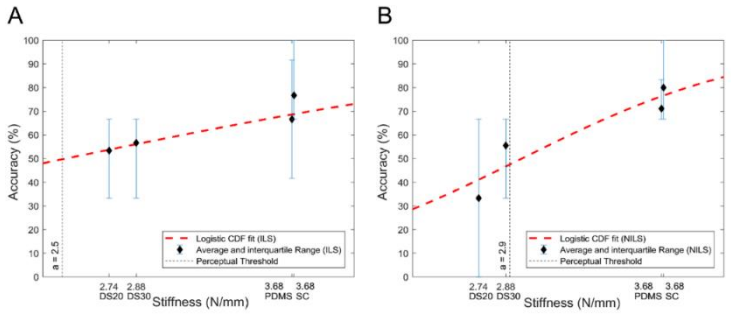

Figure 64: Psychometric curves for the psychophysical experiments: (A) ILS telepresence condition; (B) NILS telepresence condition. Black diamonds show the identification rate for all the encapsulated materials (average across participants); error bars are the interquartile range across participants; red dashed lines represent the logistic cumulative distribution function (CDF) fit.

The CDF fitting function, introduced in Section 3.3.2 and reported in Equation (21), represents the probability of a correct response at a stiffness x, where a denotes the perceptual threshold, and $b > 0$ a scale parameter that affects the curve steepness. With respect to our previous study, [136], the equation has been updated in order to account for an identification task rather than for a two-alternatives forced choice task. The final evaluation of the perception, found by fitting the response datasets into the CDF, demonstrated that the user could distinguish an inclusion with stiffness higher than a = 2.5 $N \cdot mm^{-1}$ and a = 2.9 $N \cdot mm^{-1}$ in ILS and NILS conditions, respectively (Figure 64).

Discussion and Conclusions

This work assesses the usability of the developed tactile system in tele-palpation to localize various stiffer polymeric nodules in the surrounding soft matrix during active exploration. The promising results demonstrate the ease and successful augmentation for navigation in a soft terrain. The four types of inclusions are observed to be paired with respect to their stiffness values (Softer: DS20, DS30; Stiffer: PDMS, SC) that are also reflected in the user's accuracy graph. The present study was conducted within two different telepresence conditions. Initially, in a more controlled environment, the sensing platform was placed near the user (In Line of Sight—ILS), while afterwards, the platform was moved to a remote location (Not In Line of Sight—NILS). Particularly, the latter condition presented two

challenges: remote platform control and stiffness discrimination with the haptic glove. The intrinsic absence of vision of the platform in NILS with respect to ILS is displayed in the perceptual thresholds (a = 2.9 $N \cdot mm^{-1}$ versus a = 2.5 $N \cdot mm^{-1}$). Additionally, the network latency introduced a delay of the order of *ms*, demanding the subject's attention on the active control, to coordinate the proprioceptive information with the moving platform, occasionally compromising attention to the sensory feedback. It was also observed that the subjects mostly took linear exploratory paths in both conditions, which was proven to be the best manoeuvre trajectory in the apparatus characterization (as reported in Table 8). We showed that the presented tactile telepresence system enabled the correct discrimination of the inclusions throughout the polymeric matrix, especially for the stiffer ones, in both ILS and NILS telepresence conditions. This work enriches the findings of our previous works, [12], [136], [148], confirming that the adoption of spike-like stimulation, emulating the firing activity of skin mechanoreceptors, offers a usable language of feedback that can be delivered directly on the skin surface, to provide perceptual augmentation in tele-palpation with gestural active exploration. Future works will be headed towards exploring the recognition of buried nodules along two directions: upgrading the number and realism of phantoms for medical applications, and enriching the mechanical information encoded. We will evaluate higher variations of material stiffness with the aim of discriminating healthy tissues from tumours, which are generally stiffer than the surroundings, [111], [112], [114]. Furthermore, we will also include the evaluation of encoded feedback for both normal and shear components of the contact force through the neuromorphic model. This enrichment is expected to lead to a more detailed appreciation of stiffness in cases of anisotropic mechanical behaviour of biomaterials.

4 Scientific Production

4.1 Paper Published on Scopus/ISI Journals

1) *Francesca Sorgini, Alberto Mazzoni, **Luca Massari**, Renato Caliò, Carmen Galassi, Sunil L Kukreja, Edoardo Sinibaldi, Maria Chiara Carrozza, and Calogero M Oddo. 2017. "Encapsulation of Piezoelectric Transducers for Sensory Augmentation and Substitution with Wearable Haptic Devices". Micromachines 8 (9): 270.*

2) *Francesca Sorgini, **Luca Massari**, Jessica D'Abbraccio, Eduardo Palermo, Arianna Menciassi, Petar Petrovic, Alberto Mazzoni, Maria Chiara Carrozza, Fiona Newell, and Calogero Maria Oddo. 2018. "Neuromorphic Vibrotactile Stimulation of Fingertips for Encoding Object Stiffness in Telepresence Sensory Substitution and Augmentation Applications". Sensors 18 (1).*

3) *Jessica D'Abbraccio*, **Luca Massari***, Sahana Prasanna, Laura Baldini, Francesca Sorgini, Giuseppe Airò Farulla, Andrea Bulletti, Marina Mazzoni, Lorenzo Capineri, and Arianna Menciassi. 2019. "Haptic Glove and Platform with Gestural Control For Neuromorphic Tactile Sensory Feedback In Medical Telepresence". Sensors 19 (3): 641. *equal contribution.*

4) ***Luca Massari**, Calogero Maria Oddo, Edoardo Sinibaldi, Renaud Detry, Joseph Bowkett, and Kalind Carpenter. 2019. "Tactile Sensing and Control of Robotic Manipulator Integrating Fiber Bragg Grating Strain-Sensor". Frontiers in Neurorobotics 13: 8.*

5) *Daniela Lo Presti, Carlo Massaroni, Jessica D'Abbraccio, **Luca Massari**, Michele Arturo Caponero, Giuseppe Longo, Domenico Formica, Calogero Maria Oddo, Emiliano Schena. 2019. "Wearable system based on flexible FBG for respiratory and cardiac monitoring". IEEE Sensors*

4.2 Paper Published on Journals

1) *Davide Esposito, Francesco Lanotte, Chiara Mugnai,* ***Luca Massari****, Domenico Camboni, and Calogero Maria Oddo. 2019 "A Neuromorphic Model to Match the Spiking Activity of Merkel Mechanoreceptors with Biomimetic Tactile Sensors for Bioengineering Applications". IEEE Transactions on Medical Robotics and Bionics.*

4.3 Paper Submitted to Scopus/ISI Journals

1) ***Luca Massari****, Andrea Bulletti, Sahana Prasanna, Marina Mazzoni, and Francesco Frosini. 2019. "A Mechatronic Platform for Computer Aided Detection of Nodules in Anatomopathological Analyses via Stiffness and Ultrasound Measurements," 1–13. (Submitted to Sensor)*.

2) ***Luca Massari****, Emiliano Schena, Carlo Massaroni, Paola Saccomandi, Arianna Menciassi, Edoardo Sinibaldi, and Calogero Maria Oddo. n.d. "A Machine-Learning-Based Approach To Solve Both Contact Location And Force In Soft-Material Tactile Sensors". (Submitted to Soft Robotics).*

3) *Udaya Bhaskar Rongala, Alberto Mazzoni, Marcello Chiurazzi, Domenico Camboni, Mario Milazzo,* ***Luca Massari****, Gastone Ciuti, Stefano Roccella, Paolo Dario, Calogero Maria Oddo. "Tactile Decoding of Edge Orientation with Artificial Cuneate Neurons in Dynamic Conditions," 1–20. (Submitted to Frontiers in NeuroRobotics).*

4) *Calogero Maria Oddo, Alberto Mazzoni, Giacomo Valle, Domenico Camboni, Massimo Barbaro, Gianluca Barabino, Roberto Puddu, Caterina Carboni, Lorenzo Bisoni, Jacopo Carpaneto, Fabrizio Vecchio, Francesco Petrini, Simone Romeni, Tamas Czimmerman,* ***Luca Massari****, Riccardo Di Iorio, Francesca Miraglia, Giuseppe Granata, Danilo Pani, Thomas Sstieglitz, Luigi Raffo, Maria Rossini, Silvestro Micera. "Morphological Neural Computation Restores Perception of Real-Life Textures in Transradial Amputees," no. 3. (*Submitted to Nature Communications).

5) *Renato Caliò, Domenico Camboni,* ***Luca Massari****, Jessica D'Abbraccio, Evangelos Mazomenos, Danail Stoyanov, Arianna Menciassi, Maria Chiara Carrozza, Paolo Dario, Gastone Ciuti, Calogero Maria Oddo. "Endoscopic Tactile Capsule for Non-Polypoid Colorectal Tumor Detection through Hardness and Curvature Classification". (Submitted to IEEEE Transaction on Biomedical Engineering).*

4.4 Paper Published on Conferences

1) ***Luca Massari****, Paola Saccomandi, Francesca Sorgini, Edoardo Sinibaldi, Gastone Ciuti, Arianna Menciassi, Paolo Cappa and Calogero Maria Oddo. 2016. "Tactile Sensor Array Integrating Fiber Bragg Grating Transducers for Biomechanical Measurement," 4–5. In 2016 at the IEEE Computer/robot Assisted Surgery (CRAS) Conference.*

2) *Francesca Sorgini,* ***Luca Massari****, Jessica D'Abbraccio, Eduardo Palermo, Arianna Menciassi, Petar Petrovic, Alberto Mazzoni, Maria Chiara Carrozza, Fiona Newell, Calogero Maria Oddo. 2017 "Vibrotactile stimulation of fingertips via tactile displays affects the perceived surface and shape properties of objects".* In 2017 at the International Multisensory Research Forum (IMRF) Conference.

3) ***Luca Massari****, Jessica D'Abbraccio, Laura Baldini, Francesca Sorgini, Giuseppe Airò Farulla, Petar Petrovic, Eduardo Palermo, and Calogero Maria Oddo. 2018. "Neuromorphic Haptic Glove and Platform with Gestural Control for Tactile Sensory Feedback in Medical Telepresence Applications". In 2018 at the IEEE International Symposium on Medical Measurements and Applications (MeMeA), 1–6. IEEE.*

4) Jessica D'Abbraccio, ***Luca Massari****, Martina Zaltieri, Giuseppe Terruso, Andrea Aliperta, Magdalena Kowalczyk, Emiliano Schena, Edoardo Sinibaldi, Eduardo Palermo, and Calogero Maria Oddo. 2019. "Design and Development of Large-Area FBG-Based Sensing Skin for Collaborative Robotics". In 2019 at the IEEE International Workshop on Metrology for Industry 4.0 and IoT.*

5) *Chiara Romano, Daniela Lo Presti, Emiliano Schena, Domenico Formica, Michele Arturo Caponero, Umile Giuseppe Longo, Alessandra Berton, Calogero Maria Oddo, Jessica D'Abbraccio,* ***Luca Massari****, Carlo Massaroni. 2019. "A wearable system based on fiber Bragg gratings for monitoring respiratory and heart activity of archers". In 2019 at the IEEE International Symposium on Medical Measurements and Applications (MeMeA).*

6) *Daniela Lo Presti, Carlo Massaroni, Domenico Formica, Umile Giuseppe Longo, Rosaria D'Amato, Michele Arturo Caponero, Jessica D'Abbraccio,* ***Luca Massari****, Calogero Maria Oddo, Emiliano Schena. 2019. "Cardiac monitoring with a smart textile based on polymer-encapsulated FBG: influence of sensor position". In 2019 at the IEEE International Symposium on Medical Measurements and Applications (MeMeA)*.

7) *Daniela Lo Presti, Carlo Massaroni, Jessica D'Abbraccio,* ***Luca Massari****, Calogero Maria Oddo, Arianna Carnevale, Umile Giuseppe Longo, Michele Arturo Caponero. 2019. "Single-plane neck movements and respiratory frequency monitoring: a smart system for computer workers". In 2019 at the IEEE International Workshop on Metrology for Industry 4.0 and IoT.*

8) *Sahana Prasanna,* ***Luca Massari****, Edoardo Sinibaldi, Renaud Detry, Joseph Bowkett, Kalind Carpenter, Calogero Maria Oddo"Neuromorphic tactile sensor array based on fiber Bragg gratings to encode object qualities". In 2019 SPIE Optics and Photonics for Information Processing XIII.*

4.5 Patents

1) *Bianchi Marco, Paolo Dario, Calogero Maria Oddo, Gastone Ciuti, Stefano Roccella, Mario Milazzo, Marcello Chiurazzi, Tamas Czimmermann,* ***Luca Massari****, Domenico Camboni, Maria Chiara Carrozza, Cesare Stefanini, Fabio Leoni, Davide*

Bray, Tommaso Rizzo, Francesco Bruni, Lorenzo Collodi, edoardo Farnioli, Minutillo Marco, Josè Manuel Bonilla Jimenez. 2018. "Sistema per l'identificazione di difetti su una superficie di almeno una porzione di una scocca e relativo metodo". Numero deposito 102018000004368.

2) ***Luca Massari**, Jessica D'Abbraccio, Calogero Maria Oddo, Martina Zaltieri, Eduardo Palermo, Edoardo Sinibaldi, Emiliano Schena, Giuseppe Terruso. 2019. "Progettazione e sviluppo di una pelle artificiale basata su tecnologia FBG per applicazioni in robotica collaborativa." Numero deposito: 102019000003657.*

3) ***Luca Massari**, Calogero Maria Oddo, Arianna Menciassi, Gastone Ciuti, Andrea Bulletti, Marina Mazzoni, Francesco Frosini, Lorenzo Capineri. 2018. "Apparato per l'analisi intraoperatoria di campioni di tessuto biologico". Numero deposito: 102018000001108.*

5 References

[1] R. S. Johansson and A. B. Vallbo, “Tactile sensibility in the human hand: relative and absolute densities of four types of mechanoreceptive units in glabrous skin.,” *J. Physiol.*, vol. 286, no. 1, pp. 283–300, 1979.

[2] R. S. Johansson, U. Landstrom, and R. Lundstrom, “Responses of mechanoreceptive afferent units in the glabrous skin of the human hand to sinusoidal skin displacements,” *Brain Res*, vol. 244, no. 1, pp. 17–25, 1982.

[3] R. S. Johansson and J. R. Flanagan, “Coding and use of tactile signals from the fingertips in object manipulation tasks,” *Nat. Rev. Neurosci.*, vol. 10, no. 5, p. 345, 2009.

[4] C. M. Oddo *et al.*, “Intraneural stimulation elicits discrimination of textural features by artificial fingertip in intact and amputee humans,” *Elife*, vol. 5, p. e09148, 2016.

[5] J. Dargahi, M. Parameswaran, and S. Payandeh, “A micromachined piezoelectric tactile sensor for an endoscopic grasper-theory, fabrication and experiments,” *J. microelectromechanical Syst.*, vol. 9, no. 3, pp. 329–335, 2000.

[6] N. Wettels, V. J. Santos, R. S. Johansson, and G. E. Loeb, “Biomimetic tactile sensor array,” *Adv. Robot.*, vol. 22, no. 8, pp. 829–849, 2008.

[7] M. I. Tiwana, S. J. Redmond, and N. H. Lovell, “A review of tactile sensing technologies with applications in biomedical engineering,” *Sensors Actuators A Phys.*, vol. 179, pp. 17–31, 2012.

[8] W. L. Maness, R. F. Golden, M. H. Benjamin, and R. M. Podoloff, “Pressure and contact sensor system for measuring dental occlusion.” Google Patents, 15-Aug-1989.

[9] P. Puangmali, K. Althoefer, L. D. Seneviratne, D. Murphy, and P. Dasgupta, “State-of-the-art in force and tactile sensing for minimally invasive surgery,” *IEEE Sens. J.*, vol. 8, no. 4, pp. 371–381, 2008.

[10] C. J. Jacobus, A. J. Riggs, and M. J. Taylor, “Method and system for providing a tactile virtual reality and manipulator defining an interface device therefor.” Google Patents, 14-Feb-1995.

[11] F. Sorgini *et al.*, “Encapsulation of piezoelectric transducers for sensory augmentation and substitution with wearable

haptic devices," *Micromachines*, vol. 8, no. 9, p. 270, 2017.
[12] L. Massari *et al.*, "Neuromorphic haptic glove and platform with gestural control for tactile sensory feedback in medical telepresence applications," in *2018 IEEE International Symposium on Medical Measurements and Applications (MeMeA)*, 2018, pp. 1–6.
[13] D. G. Caldwell, N. Tsagarakis, and C. Giesler, "An integrated tactile/shear feedback array for stimulation of finger mechanoreceptor," in *Robotics and Automation, 1999. Proceedings. 1999 IEEE International Conference on*, 1999, vol. 1, pp. 287–292.
[14] M. H. Lee and H. R. Nicholls, "Review Article Tactile sensing for mechatronics—a state of the art survey," *mechatronics*, vol. 9, no. 1, pp. 1–31, 1999.
[15] H. R. Nicholls and M. H. Lee, "A survey of robot tactile sensing technology," *Int. J. Rob. Res.*, vol. 8, no. 3, pp. 3–30, 1989.
[16] R. S. Dahiya, G. Metta, M. Valle, and G. Sandini, "From humans to humanoids," *IEEE Trans. Robot.*, vol. 26, no. 1, pp. 1–20, 2009.
[17] L. D. Harmon, "Automated tactile sensing," *Int. J. Rob. Res.*, vol. 1, no. 2, pp. 3–32, 1982.
[18] H. Yousef, M. Boukallel, and K. Althoefer, "Tactile sensing for dexterous in-hand manipulation in robotics—A review," *Sensors Actuators A Phys.*, vol. 167, no. 2, pp. 171–187, 2011.
[19] J. Tegin and J. Wikander, "Tactile sensing in intelligent robotic manipulation–a review," *Ind. Robot An Int. J.*, vol. 32, no. 1, pp. 64–70, 2005.
[20] R. D. Howe, "Tactile sensing and control of robotic manipulation," *Adv. Robot.*, vol. 8, no. 3, pp. 245–261, 1993.
[21] C. Majidi, "Soft robotics: a perspective—current trends and prospects for the future," *Soft Robot.*, vol. 1, no. 1, pp. 5–11, 2014.
[22] D. Trivedi, C. D. Rahn, W. M. Kier, and I. D. Walker, "Soft robotics: Biological inspiration, state of the art, and future research," *Appl. bionics Biomech.*, vol. 5, no. 3, pp. 99–117, 2008.
[23] S. Kim, C. Laschi, and B. Trimmer, "Soft robotics: a bioinspired evolution in robotics," *Trends Biotechnol.*, vol.

31, no. 5, pp. 287–294, 2013.
[24] M. T. Tolley *et al.*, “A resilient, untethered soft robot,” *Soft Robot.*, vol. 1, no. 3, pp. 213–223, 2014.
[25] Y. Ohmura, Y. Kuniyoshi, and A. Nagakubo, “Conformable and scalable tactile sensor skin for curved surfaces,” in *Robotics and Automation, 2006. ICRA 2006. Proceedings 2006 IEEE International Conference on*, 2006, pp. 1348–1353.
[26] F. L. Hammond, R. K. Kramer, Q. Wan, R. D. Howe, and R. J. Wood, “Soft tactile sensor arrays for micromanipulation,” in *Intelligent Robots and Systems (IROS), 2012 IEEE/RSJ International Conference on*, 2012, pp. 25–32.
[27] R. Kageyama, S. Kagami, M. Inaba, and H. Inoue, “Development of soft and distributed tactile sensors and the application to a humanoid robot,” in *Systems, Man, and Cybernetics, 1999. IEEE SMC’99 Conference Proceedings. 1999 IEEE International Conference on*, 1999, vol. 2, pp. 981–986.
[28] L. Jamone, L. Natale, G. Metta, and G. Sandini, “Highly sensitive soft tactile sensors for an anthropomorphic robotic hand,” *IEEE Sens. J.*, vol. 15, no. 8, pp. 4226–4233, 2015.
[29] A. Kadowaki, T. Yoshikai, M. Hayashi, and M. Inaba, “Development of soft sensor exterior embedded with multi-axis deformable tactile sensor system,” in *Robot and Human Interactive Communication, 2009. RO-MAN 2009. The 18th IEEE International Symposium on*, 2009, pp. 1093–1098.
[30] R. Tajima, S. Kagami, M. Inaba, and H. Inoue, “Development of soft and distributed tactile sensors and the application to a humanoid robot,” *Adv. Robot.*, vol. 16, no. 4, pp. 381–397, 2002.
[31] X.-D. Wang and O. S. Wolfbeis, “Fiber-optic chemical sensors and biosensors (2008–2012),” *Anal. Chem.*, vol. 85, no. 2, pp. 487–508, 2012.
[32] E. Udd and W. B. Spillman Jr, *Fiber optic sensors: an introduction for engineers and scientists*. John Wiley & Sons, 2011.
[33] P. Polygerinos, D. Zbyszewski, T. Schaeffter, R. Razavi, L. D. Seneviratne, and K. Althoefer, “MRI-compatible fiber-optic force sensors for catheterization procedures,” *IEEE Sens. J.*, vol. 10, no. 10, pp. 1598–1608, 2010.

[34] A. Barrias, J. R. Casas, and S. Villalba, “A review of distributed optical fiber sensors for civil engineering applications,” *Sensors*, vol. 16, no. 5, p. 748, 2016.
[35] C. Massaroni, P. Saccomandi, and E. Schena, “Medical smart textiles based on fiber optic technology: an overview,” *J. Funct. Biomater.*, vol. 6, no. 2, pp. 204–221, 2015.
[36] A. F. da Silva, A. F. Gonçalves, L. A. de Almeida Ferreira, F. M. M. Araújo, P. M. Mendes, and J. H. Correia, “PVC smart sensing foil for advanced strain measurements,” *IEEE Sens. J.*, vol. 10, no. 6, pp. 1149–1155, 2010.
[37] S. Silvestri and E. Schena, “Optical-fiber measurement systems for medical applications,” in *Optoelectronics-Devices and Applications*, InTech, 2011.
[38] H.-N. Li, D.-S. Li, and G.-B. Song, “Recent applications of fiber optic sensors to health monitoring in civil engineering,” *Eng. Struct.*, vol. 26, no. 11, pp. 1647–1657, 2004.
[39] L. Ascari, P. Corradi, L. Beccai, and C. Laschi, “A miniaturized and flexible optoelectronic sensing system for tactile skin,” *J. Micromechanics Microengineering*, vol. 17, no. 11, p. 2288, 2007.
[40] J.-S. Heo, C.-H. Han, and J.-J. Lee, “System design and evaluation of the robot tactile sensor using the microbending fiber optic sensors,” in *Robot and Human Interactive Communication, 2007. RO-MAN 2007. The 16th IEEE International Symposium on*, 2007, pp. 14–18.
[41] S. Pirozzi, “Multi-point force sensor based on crossed optical fibers,” *Sensors Actuators A Phys.*, vol. 183, pp. 1–10, 2012.
[42] X. Liu, I. I. Iordachita, X. He, R. H. Taylor, and J. U. Kang, “Miniature fiber-optic force sensor based on low-coherence Fabry-Pérot interferometry for vitreoretinal microsurgery,” *Biomed. Opt. Express*, vol. 3, no. 5, pp. 1062–1076, 2012.
[43] Q. Liang *et al.*, “Multi-Component FBG-Based Force Sensing Systems by Comparison With Other Sensing Technologies: A Review,” *IEEE Sens. J.*, vol. 18, no. 18, pp. 7345–7357, 2018.
[44] T. Li, C. Shi, and H. Ren, “A High-Sensitivity Tactile Sensor Array Based on Fiber Bragg Grating Sensing for Tissue Palpation in Minimally Invasive Surgery,” *IEEE/ASME Trans. Mechatronics*, 2018.
[45] P. Saccomandi *et al.*, “Feedforward neural network for force

coding of an MRI-compatible tactile sensor array based on fiber Bragg grating," *J. Sensors*, vol. 2015, 2015.

[46] J. Song *et al.*, "Research on pressure tactile sensing technology based on fiber Bragg grating array," *Photonic Sensors*, vol. 5, no. 3, pp. 263–272, 2015.

[47] L. H. Negri, A. S. Paterno, M. Muller, and J. L. Fabris, "Sparse Force Mapping System Based on Compressive Sensing.," *IEEE Trans. Instrum. Meas.*, vol. 66, no. 4, pp. 830–836, 2017.

[48] M. A. Pedroso, L. H. Negri, M. A. Kamizi, J. L. Fabris, and M. Muller, "Fabrication of a tactile sensor array with fiber Bragg gratings using a 3D printed mold," in *Microwave and Optoelectronics Conference (IMOC), 2017 SBMO/IEEE MTT-S International*, 2017, pp. 1–4.

[49] B. Junjie, L. Jianqing, W. Ying, and W. Jianfeng, "Composite tactile sensor array using fiber Bragg grating sensors and measuring system," 2010.

[50] J.-S. Heo, J.-Y. Kim, and J.-J. Lee, "Tactile sensors using the distributed optical fiber sensors," in *Sensing Technology, 2008. ICST 2008. 3rd International Conference on*, 2008, pp. 486–490.

[51] M. A. Pedroso, L. H. Negri, M. A. Kamizi, J. L. Fabris, and M. Muller, "Tactile Sensor Array with Fiber Bragg Gratings in Quasi-Distributed Sensing," *J. Sensors*, vol. 2018, 2018.

[52] Q. Jiang and L. Xiang, "Design and experimental research on small-structures of tactile sensor array unit based on fiber Bragg grating," *IEEE Sens. J.*, vol. 17, no. 7, pp. 2048–2054, 2017.

[53] C. Massaroni *et al.*, "Smart textile for respiratory monitoring and thoraco-abdominal motion pattern evaluation," *J. Biophotonics*, vol. 11, no. 5, p. e201700263, 2018.

[54] X.-W. Ye, Y.-H. Su, and P.-S. Xi, "Statistical analysis of stress signals from bridge monitoring by FBG system," *Sensors*, vol. 18, no. 2, p. 491, 2018.

[55] J.-S. Heo, J.-H. Chung, and J.-J. Lee, "Tactile sensor arrays using fiber Bragg grating sensors," *Sensors Actuators A Phys.*, vol. 126, no. 2, pp. 312–327, 2006.

[56] M. R. Cutkosky, R. D. Howe, and W. R. Provancher, "Force and tactile sensors," in *Springer Handbook of Robotics*, Springer, 2008, pp. 455–476.

[57] J. Ulmen and M. Cutkosky, “A robust, low-cost and low-noise artificial skin for human-friendly robots,” in *Robotics and Automation (ICRA), 2010 IEEE International Conference on*, 2010, pp. 4836–4841.

[58] B. Heyneman and M. R. Cutkosky, “Biologically inspired tactile classification of object-hand and object-world interactions,” in *Robotics and Biomimetics (ROBIO), 2012 IEEE International Conference on*, 2012, pp. 167–173.

[59] L. A. Jones and S. J. Lederman, *Human hand function*. Oxford University Press, 2006.

[60] T. L. T. Lun, K. Wang, J. D. L. Ho, K.-H. Lee, K. Y. Sze, and K.-W. Kwok, “Real-Time Surface Shape Sensing for Soft and Flexible Structures Using Fiber Bragg Gratings,” *IEEE Robot. Autom. Lett.*, vol. 4, no. 2, pp. 1454–1461, 2019.

[61] L. Cai *et al.*, “Super-stretchable, transparent carbon nanotube-based capacitive strain sensors for human motion detection,” *Sci. Rep.*, vol. 3, p. 3048, 2013.

[62] C. T. Manuel, R. Harb, A. Badran, D. Ho, and B. J. F. Wong, “Finite element model and validation of nasal tip deformation,” *Ann. Biomed. Eng.*, vol. 45, no. 3, pp. 829–838, 2017.

[63] Y. Hao *et al.*, “A Soft Bionic Gripper with Variable Effective Length,” *J. Bionic Eng.*, vol. 15, no. 2, pp. 220–235, 2018.

[64] Z. Wang and S. Hirai, “Chamber dimension optimization of a bellow-type soft actuator for food material handling,” in *2018 IEEE International Conference on Soft Robotics (RoboSoft)*, 2018.

[65] H. Zhang, A. S. Kumar, J. Y. H. Fuh, and M. Y. Wang, “Topology optimized design, fabrication and evaluation of a multimaterial soft gripper,” in *2018 IEEE International Conference on Soft Robotics (RoboSoft)*, 2018.

[66] R. S. Dahiya, G. Metta, M. Valle, and G. Sandini, “Tactile sensing—from humans to humanoids,” *IEEE Trans. Robot.*, vol. 26, no. 1, pp. 1–20, 2010.

[67] T. Hoshi and H. Shinoda, “Robot skin based on touch-area-sensitive tactile element,” in *Proceedings 2006 IEEE International Conference on Robotics and Automation, 2006. ICRA 2006.*, 2006, pp. 3463–3468.

[68] A. Bicchi, “Hands for dexterous manipulation and robust grasping: A difficult road toward simplicity,” *IEEE Trans.*

Robot. Autom., vol. 16, no. 6, pp. 652–662, 2000.
[69] R. M. Murray, *A mathematical introduction to robotic manipulation*. CRC press, 2017.
[70] C. Chi, X. Sun, N. Xue, T. Li, and C. Liu, "Recent Progress in Technologies for Tactile Sensors," *Sensors*, vol. 18, no. 4, p. 948, 2018.
[71] A. T. Golpaygani, S. Najarian, and M. Movahedi, "Tactile sensor for robotic applications," in *World Congress on Medical Physics and Biomedical Engineering, September 7-12, 2009, Munich, Germany*, 2009, pp. 2299–2302.
[72] D. M. Vogt, Y.-L. Park, and R. J. Wood, "Design and characterization of a soft multi-axis force sensor using embedded microfluidic channels," *IEEE Sens. J.*, vol. 13, no. 10, pp. 4056–4064, 2013.
[73] R. D. P. Wong, J. D. Posner, and V. J. Santos, "Flexible microfluidic normal force sensor skin for tactile feedback," *Sensors Actuators A Phys.*, vol. 179, pp. 62–69, 2012.
[74] C. A. Jara, J. Pomares, F. A. Candelas, and F. Torres, "Control framework for dexterous manipulation using dynamic visual servoing and tactile sensors' feedback," *Sensors*, vol. 14, no. 1, pp. 1787–1804, 2014.
[75] A. Schmitz, P. Maiolino, M. Maggiali, L. Natale, G. Cannata, and G. Metta, "Methods and technologies for the implementation of large-scale robot tactile sensors," *IEEE Trans. Robot.*, vol. 27, no. 3, pp. 389–400, 2011.
[76] J. M. Romano, K. Hsiao, G. Niemeyer, S. Chitta, and K. J. Kuchenbecker, "Human-inspired robotic grasp control with tactile sensing," *IEEE Trans. Robot.*, vol. 27, no. 6, pp. 1067–1079, 2011.
[77] G. Canavese *et al.*, "Piezoresistive flexible composite for robotic tactile applications," *Sensors Actuators A Phys.*, vol. 208, pp. 1–9, 2014.
[78] J. Sirohi and I. Chopra, "Fundamental understanding of piezoelectric strain sensors," *J. Intell. Mater. Syst. Struct.*, vol. 11, no. 4, pp. 246–257, 2000.
[79] M. A. Qasaimeh, S. Sokhanvar, J. Dargahi, and M. Kahrizi, "PVDF-based microfabricated tactile sensor for minimally invasive surgery," *J. Microelectromechanical Syst.*, vol. 18, no. 1, pp. 195–207, 2009.
[80] L. Seminara *et al.*, "Piezoelectric polymer transducer arrays

for flexible tactile sensors," *IEEE Sens. J.*, vol. 13, no. 10, pp. 4022–4029, 2013.

[81] M.-S. Kim, H.-R. Ahn, S. Lee, C. Kim, and Y.-J. Kim, "A dome-shaped piezoelectric tactile sensor arrays fabricated by an air inflation technique," *Sensors Actuators A Phys.*, vol. 212, pp. 151–158, 2014.

[82] C.-H. Chuang, M.-S. Wang, Y.-C. Yu, C.-L. Mu, K.-F. Lu, and C.-T. Lin, "Flexible tactile sensor for the grasping control of robot fingers," in *Advanced Robotics and Intelligent Systems (ARIS), 2013 International Conference on*, 2013, pp. 141–146.

[83] M. Acer, M. Salerno, K. Agbeviade, and J. Paik, "Development and characterization of silicone embedded distributed piezoelectric sensors for contact detection," *Smart Mater. Struct.*, vol. 24, no. 7, p. 75030, 2015.

[84] R. S. Dahiya and M. Valle, "Tactile sensing for robotic applications," in *Sensors: Focus on Tactile Force and Stress Sensors*, InTech, 2008.

[85] P. S. Girão, P. M. P. Ramos, O. Postolache, and J. M. D. Pereira, "Tactile sensors for robotic applications," *Measurement*, vol. 46, no. 3, pp. 1257–1271, 2013.

[86] C. M. Oddo *et al.*, "Intraneural stimulation elicits discrimination of textural features by artificial fingertip in intact and amputee humans," *Elife*, pp. 1–27, 2016.

[87] C.-W. Ma, L.-S. Hsu, J.-C. Kuo, and Y.-J. Yang, "A flexible tactile and shear sensing array fabricated using a novel buckypaper patterning technique," *Sensors Actuators A Phys.*, vol. 231, pp. 21–27, 2015.

[88] T. Someya and T. Sekitani, "Bionic skins using flexible organic devices," in *Micro Electro Mechanical Systems (MEMS), 2014 IEEE 27th International Conference on*, 2014, pp. 68–71.

[89] W. Townsend, "The BarrettHand grasper–programmably flexible part handling and assembly," *Ind. Robot an Int. J.*, vol. 27, no. 3, pp. 181–188, 2000.

[90] J. Butterfaß, M. Grebenstein, H. Liu, and G. Hirzinger, "DLR-Hand II: Next generation of a dextrous robot hand," in *Robotics and Automation, 2001. Proceedings 2001 ICRA. IEEE International Conference on*, 2001, vol. 1, pp. 109–114.

[91] A. M. Ramos, I. A. Gravagne, and I. D. Walker, "Goldfinger: A

non-anthropomorphic, dextrous robot hand," in *Robotics and Automation, 1999. Proceedings. 1999 IEEE International Conference on*, 1999, vol. 2, pp. 913–919.

[92] A. Eusebi, C. Fantuzzi, C. Melchiorri, M. Sandri, and A. Tonielli, "The UB hand II control system: Design features and experimental results," in *Industrial Electronics, Control and Instrumentation, 1994. IECON'94., 20th International Conference on*, 1994, vol. 2, pp. 782–787.

[93] P. Hebert *et al.*, "Mobile manipulation and mobility as manipulation—design and algorithms of RoboSimian," *J. F. Robot.*, vol. 32, no. 2, pp. 255–274, 2015.

[94] S. Karumanchi *et al.*, "Team RoboSimian: Semi-autonomous Mobile Manipulation at the 2015 DARPA Robotics Challenge Finals," in *The DARPA Robotics Challenge Finals: Humanoid Robots To The Rescue*, Springer, 2018, pp. 191–235.

[95] Z. Kappassov, J.-A. Corrales, and V. Perdereau, "Tactile sensing in dexterous robot hands," *Rob. Auton. Syst.*, vol. 74, pp. 195–220, 2015.

[96] J. S. Heo, J. H. Chung, and J. J. Lee, "Tactile sensor arrays using fiber Bragg grating sensors," *Sensors Actuators, A Phys.*, 2006.

[97] R. S. Dahiya, P. Mittendorfer, M. Valle, G. Cheng, and V. J. Lumelsky, "Directions toward effective utilization of tactile skin: A review," *IEEE Sens. J.*, vol. 13, no. 11, pp. 4121–4138, 2013.

[98] Y.-L. Park, B. Chen, and R. J. Wood, "Soft artificial skin with multi-modal sensing capability using embedded liquid conductors," in *2011 IEEE SENSORS Proceedings*, 2011.

[99] P. Mittendorfer and G. Cheng, "Humanoid multimodal tactile-sensing modules," *IEEE Trans. Robot.*, 2011.

[100] K. Chethana, A. S. Guru Prasad, S. N. Omkar, and S. Asokan, "Fiber bragg grating sensor based device for simultaneous measurement of respiratory and cardiac activities," *J. Biophotonics*, vol. 10, no. 2, pp. 278–285, 2017.

[101] D. P. Lo, C. Massaroni, P. Saccomandi, M. A. Caponero, D. Formica, and E. Schena, "A wearable textile for respiratory monitoring: Feasibility assessment and analysis of sensors position on system response.," in *Conference proceedings:... Annual International Conference of the IEEE Engineering in Medicine and Biology Society. IEEE Engineering in Medicine*

and Biology Society. Annual Conference, 2017, vol. 2017, pp. 4423–4426.

[102] H. Song, H. Kim, J. Jeong, and J. Lee, "Development of FBG sensor system for force-feedback in minimally invasive robotic surgery," in *Sensing Technology (ICST), 2011 Fifth International Conference on*, 2011, pp. 16–20.

[103] P. Mittendorfer, E. Yoshida, and G. Cheng, "Realizing whole-body tactile interactions with a self-organizing, multi-modal artificial skin on a humanoid robot," *Adv. Robot.*, vol. 29, no. 1, pp. 51–67, 2015.

[104] A. B. Vallbo and R. S. Johansson, "Properties of cutaneous mechanoreceptors in the human hand related to touch sensation," *Hum Neurobiol*, vol. 3, no. 1, pp. 3–14, 1984.

[105] L. Massari *et al.*, "Tactile sensor array integrating fiber Bragg grating transducers for biomechanical measurement," pp. 4–5.

[106] A. Pierangelo *et al.*, "Ex-vivo characterization of human colon cancer by Mueller polarimetric imaging," *Opt Express*, vol. 19, no. February 2016, p. 1582, 2011.

[107] R. Adam, "Chemotherapy and surgery: new perspectives on the treatment of unresectable liver metastases," *Ann. Oncol.*, vol. 14, no. 90002, pp. ii13-ii16, 2003.

[108] T. Nagai *et al.*, "A new diagnostic method for rapid detection of lymph node metastases using a one-step nucleic acid amplification (OSNA) assay in endometrial cancer.," *Ann. Surg. Oncol.*, vol. 22, no. 3, pp. 980–986, 2015.

[109] S. Candefjord, K. Ramser, and O. A. Lindahl, "Technologies for localization and diagnosis of prostate cancer.," *J. Med. Eng. Technol.*, vol. 33, no. 8, pp. 585–603, 2009.

[110] T. A. Krouskop, T. M. Wheeler, F. Kallel, B. S. Garra, and T. Hall, "Elastic moduli of breast and prostate tissues under compression," *Ultrason. Imaging*, vol. 20, no. 4, pp. 260–274, 1998.

[111] A. Samani, J. Zubovits, and D. Plewes, "Elastic moduli of normal and pathological human breast tissues: an inversion-technique-based investigation of 169 samples," *Phys. Med. Biol.*, vol. 52, no. 6, p. 1565, 2007.

[112] M. Zhang *et al.*, "Quantitative characterization of viscoelastic properties of human prostate correlated with

histology," *Ultrasound Med. Biol.*, vol. 34, no. 7, pp. 1033–1042, 2008.

[113] T. Raveh Tilleman, M. M. Tilleman, and H. A. M. Neumann, "The elastic properties of cancerous skin: Poisson's ratio and Young's modulus.," *Optim. Incisions Cutan. Surg. Incl. Mohs' Microgr. Surgery.*, p. 105, 2004.

[114] B. Winstone, C. Melhuish, T. Pipe, M. Callaway, and S. Dogramadzi, "Toward Bio-Inspired Tactile Sensing Capsule Endoscopy for Detection of Submucosal Tumors," *IEEE Sens. J.*, vol. 17, no. 3, pp. 848–857, 2017.

[115] F. J. Carter, T. G. Frank, P. J. Davies, D. McLean, and A. Cuschieri, "Measurements and modelling of the compliance of human and porcine organs," *Med. Image Anal.*, vol. 5, no. 4, pp. 231–236, 2001.

[116] J. Konstantinova, M. Li, G. Mehra, P. Dasgupta, K. Althoefer, and T. Nanayakkara, "Behavioral characteristics of manual palpation to localize hard nodules in soft tissues," *IEEE Trans. Biomed. Eng.*, vol. 61, no. 6, pp. 1651–1659, 2014.

[117] P. N. T. Wells and H.-D. Liang, "Medical ultrasound: imaging of soft tissue strain and elasticity," *J. R. Soc. Interface*, vol. 8, no. 64, pp. 1521–1549, 2011.

[118] W. C. Carson, G. J. Gerling, T. L. Krupski, C. G. Kowalik, J. C. Harper, and C. A. Moskaluk, "Material characterization of ex vivo prostate tissue via spherical indentation in the clinic," *Med. Eng. Phys.*, vol. 33, no. 3, pp. 302–309, 2011.

[119] J. C. Gwilliam, T. Yoshioka, A. M. Okamura, and S. S. Hsiao, "Neural coding of passive lump detection in compliant artificial tissue," *J. Neurophysiol.*, vol. 112, no. 5, pp. 1131–1141, 2014.

[120] J. M. Yau, S. S. Kim, P. H. Thakur, and S. J. Bensmaia, "Feeling form: the neural basis of haptic shape perception," *J. Neurophysiol.*, vol. 115, no. 2, pp. 631–642, 2015.

[121] K. Nam *et al.*, "Ultrasonic attenuation and backscatter coefficient estimates of rodent-tumor-mimicking structures: comparison of results among clinical scanners," *Ultrason. Imaging*, vol. 33, no. 4, pp. 233–250, 2011.

[122] G. Hoch, V. Croise-Laurent, A. Germain, L. Brunaud, L. Bresler, and A. Ayav, "Is intraoperative ultrasound still useful for the detection of colorectal cancer liver metastases?," *HPB*, vol. 17, no. 6, pp. 514–519, 2015.

[123] S. Hata *et al.*, “Value of visual inspection, bimanual palpation, and intraoperative ultrasonography during hepatic resection for liver metastases of colorectal carcinoma,” *World J. Surg.*, vol. 35, no. 12, pp. 2779–2787, 2011.
[124] A. Ferrero *et al.*, “Intraoperative liver ultrasound still affects surgical strategy for patients with colorectal metastases in the modern era,” *World J. Surg.*, vol. 37, no. 11, pp. 2655–2663, 2013.
[125] R. Chou *et al.*, “Imaging techniques for the diagnosis of hepatocellular carcinoma: a systematic review and meta-analysis,” *Ann. Intern. Med.*, vol. 162, no. 10, pp. 697–711, 2015.
[126] A. R. Baker and C. G. Windsor, “The classification of defects from ultrasonic data using neural networks: The Hopfield method,” *NDT Int.*, vol. 22, no. 2, pp. 97–105, 1989.
[127] A. K. Jain, “Data clustering: 50 years beyond K-means,” *Pattern Recognit. Lett.*, vol. 31, no. 8, pp. 651–666, 2010.
[128] B.-M. Ahn, J. Kim, L. Ian, K.-H. Rha, and H.-J. Kim, “Mechanical property characterization of prostate cancer using a minimally motorized indenter in an ex vivo indentation experiment,” *Urology*, vol. 76, no. 4, pp. 1007–1011, 2010.
[129] R. G. Barr *et al.*, “Elastography assessment of liver fibrosis: society of radiologists in ultrasound consensus conference statement,” *Radiology*, vol. 276, no. 3, pp. 845–861, 2015.
[130] W. Li *et al.*, “Polyvinyl chloride as a multimodal tissue-mimicking material with tuned mechanical and medical imaging properties,” *Med. Phys.*, vol. 43, no. 10, pp. 5577–5592, 2016.
[131] M. O. Culjat, D. Goldenberg, P. Tewari, and R. S. Singh, “A review of tissue substitutes for ultrasound imaging,” *Ultrasound Med. Biol.*, vol. 36, no. 6, pp. 861–873, 2010.
[132] A. Cafarelli, A. Verbeni, A. Poliziani, P. Dario, A. Menciassi, and L. Ricotti, “Tuning acoustic and mechanical properties of materials for ultrasound phantoms and smart substrates for cell cultures,” *Acta Biomater.*, vol. 49, pp. 368–378, 2017.
[133] R. Cao, Z. Huang, T. Varghese, and G. Nabi, “Tissue mimicking materials for the detection of prostate cancer

using shear wave elastography: A validation study," *Med. Phys.*, vol. 40, no. 2, 2013.
[134] K. Manickam, R. R. Machireddy, and S. Seshadri, "Study of ultrasound stiffness imaging methods using tissue mimicking phantoms," *Ultrasonics*, vol. 54, no. 2, pp. 621–631, 2014.
[135] A. Bulletti, P. Giannelli, M. Calzolai, and L. Capineri, "An integrated acousto/ultrasonic structural health monitoring system for composite pressure vessels," *IEEE Trans. Ultrason. Ferroelectr. Freq. Control*, vol. 63, no. 6, pp. 864–873, 2016.
[136] F. Sorgini *et al.*, "Neuromorphic vibrotactile stimulation of fingertips for encoding object stiffness in telepresence sensory substitution and augmentation applications," *Sensors (Switzerland)*, vol. 18, no. 1, 2018.
[137] E. Biddiss, D. Beaton, and T. Chau, "Consumer design priorities for upper limb prosthetics," *Disabil. Rehabil. Assist. Technol.*, vol. 2, no. 6, pp. 346–357, 2007.
[138] R. Kwok, "Neuroprosthetics: once more, with feeling," *Nat. News*, vol. 497, no. 7448, p. 176, 2013.
[139] S.-C. Liu and T. Delbruck, "Neuromorphic sensory systems," *Curr. Opin. Neurobiol.*, vol. 20, no. 3, pp. 288–295, 2010.
[140] P. Dario, B. Hannaford, and A. Takanishi, "Guest editorial special issue on biorobotics," *IEEE Trans. Robot.*, vol. 24, no. 1, pp. 3–4, 2008.
[141] Y. Zhengkun and Z. Yilei, "Recognizing tactile surface roughness with a biomimetic fingertip: A soft neuromorphic approach," *Neurocomputing*, vol. 244, pp. 102–111, 2017.
[142] E. M. Izhikevich, "Simple model of spiking neurons," *IEEE Trans. Neural Networks*, vol. 14, no. 6, pp. 1569–1572, 2003.
[143] M. Knibestöl, "Stimulus-response functions of slowly adapting mechanoreceptors in the human glabrous skin area.," *J. Physiol.*, vol. 245, no. 1, pp. 63–80, 1975.
[144] L. L. Bologna, J. Pinoteau, R. Brasselet, M. Maggiali, and A. Arleo, "Encoding/decoding of first and second order tactile afferents in a neurorobotic application," *J. Physiol.*, vol. 105, no. 1–3, pp. 25–35, 2011.
[145] L. L. Bologna *et al.*, "A closed-loop neurobotic system for fine touch sensing," *J. Neural Eng.*, vol. 10, no. 4, p. 46019, 2013.

[146] G. Spigler, C. M. Oddo, and M. C. Carrozza, “Soft-neuromorphic artificial touch for applications in neuro-robotics,” in *2012 4th Ieee Ras & Embs International Conference on Biomedical Robotics and Biomechatronics (Biorob)*, 2012, pp. 1913–1918.

[147] U. B. Rongala, A. Mazzoni, and C. M. Oddo, “Neuromorphic artificial touch for categorization of naturalistic textures,” *IEEE Trans. neural networks Learn. Syst.*, vol. 28, no. 4, pp. 819–829, 2017.

[148] C. M. Oddo *et al.*, “Artificial spatiotemporal touch inputs reveal complementary decoding in neocortical neurons,” *Sci. Rep.*, vol. 7, p. 45898, 2017.

[149] W. W. Lee, J. Cabibihan, and N. V Thakor, “Bio-mimetic strategies for tactile sensing,” in *SENSORS, 2013 IEEE*, 2013, pp. 1–4.

[150] L. E. Osborn *et al.*, “Prosthesis with neuromorphic multilayered e-dermis perceives touch and pain,” *Sci. Robot.*, vol. 3, no. 19, p. eaat3818, 2018.

[151] Z. Yi and Y. Zhang, “Bio-inspired tactile FA-I spiking generation under sinusoidal stimuli,” *J. Bionic Eng.*, vol. 13, no. 4, pp. 612–621, 2016.

[152] Y. Dong, S. Mihalas, S. S. Kim, T. Yoshioka, S. J. Bensmaia, and E. Niebur, “A simple model of mechanotransduction in primate glabrous skin,” *Am. J. Physiol. Circ. Physiol.*, 2012.

[153] S. S. Kim, A. P. Sripati, R. J. Vogelstein, R. S. Armiger, A. F. Russell, and S. J. Bensmaia, “Conveying tactile feedback in sensorized hand neuroprostheses using a biofidelic model of mechanotransduction,” *IEEE Trans. Biomed. Circuits Syst.*, vol. 3, no. 6, pp. 398–404, 2009.

[154] S. S. Kim, A. P. Sripati, and S. J. Bensmaia, “Predicting the timing of spikes evoked by tactile stimulation of the hand,” *Am. J. Physiol. Circ. Physiol.*, 2010.

[155] S. S. Kim, S. Mihalas, A. Russell, Y. Dong, and S. J. Bensmaia, “Does afferent heterogeneity matter in conveying tactile feedback through peripheral nerve stimulation?,” *IEEE Trans. Neural Syst. Rehabil. Eng.*, vol. 19, no. 5, pp. 514–520, 2011.

[156] H. P. Saal, B. P. Delhaye, B. C. Rayhaun, and S. J. Bensmaia, “Simulating tactile signals from the whole hand with millisecond precision,” *Proc. Natl. Acad. Sci.*, vol. 114, no.

28, pp. E5693–E5702, 2017.
[157] G. Valle *et al.*, “Biomimetic intraneural sensory feedback enhances sensation naturalness, tactile sensitivity, and manual dexterity in a bidirectional prosthesis,” *Neuron*, vol. 100, no. 1, pp. 37–45, 2018.
[158] T. Harrington and M. M. Merzenich, “Neural coding in the sense of touch: human sensations of skin indentation compared with the responses of slowly adapting mechanoreceptive afferents innervating the hairy skin of monkeys,” *Exp. Brain Res.*, vol. 10, no. 3, pp. 251–264, 1970.
[159] A. G. Brown and A. Iggo, “A quantitative study of cutaneous receptors and afferent fibres in the cat and rabbit,” *J. Physiol.*, vol. 193, no. 3, pp. 707–733, 1967.
[160] L. Kruger and B. Kenton, “Quantitative neural and psychophysical data for cutaneous mechanoreceptor function,” *Brain Res.*, vol. 49, no. 1, pp. 1–24, 1973.
[161] J. Marquínez, J. Lastra, and P. García, “Estimation models for precipitation in mountainous regions: the use of GIS and multivariate analysis,” *J. Hydrol.*, vol. 270, no. 1–2, pp. 1–11, 2003.
[162] L. Ye, M. Yang, L. Xu, C. Guo, L. Li, and D. Wang, “Optimization of inductive angle sensor using response surface methodology and finite element method,” *Measurement*, vol. 48, pp. 252–262, 2014.
[163] Z. Yi, Y. Zhang, and J. Peters, “Biomimetic tactile sensors and signal processing with spike trains: A review,” *Sensors Actuators A Phys.*, vol. 269, pp. 41–52, 2018.
[164] D. R. Lesniak and G. J. Gerling, “Predicting SA-I mechanoreceptor spike times with a skin-neuron model,” *Math. Biosci.*, vol. 220, no. 1, pp. 15–23, 2009.
[165] E. K. Kim, S. A. Wellnitz, S. M. Bourdon, E. A. Lumpkin, and G. J. Gerling, “Force sensor in simulated skin and neural model mimic tactile SAI afferent spiking response to ramp and hold stimuli,” *J. Neuroeng. Rehabil.*, vol. 9, no. 1, p. 45, 2012.
[166] P. Valdastri *et al.*, “Characterization of a novel hybrid silicon three-axial force sensor,” *Sensors Actuators A Phys.*, vol. 123, pp. 249–257, 2005.
[167] L. Beccai *et al.*, “Design and fabrication of a hybrid silicon three-axial force sensor for biomechanical applications,”

Sensors Actuators A Phys., vol. 120, no. 2, pp. 370–382, 2005.
[168] C. M. Oddo, M. Controzzi, L. Beccai, C. Cipriani, and M. C. Carrozza, “Roughness encoding for discrimination of surfaces in artificial active-touch,” *IEEE Trans. Robot.*, vol. 27, no. 3, pp. 522–533, 2011.
[169] C. M. Oddo, L. Beccai, M. Felder, F. Giovacchini, and M. C. Carrozza, “Artificial roughness encoding with a bio-inspired MEMS-based tactile sensor array,” *Sensors*, vol. 9, no. 5, pp. 3161–3183, 2009.
[170] S. Raspopovic *et al.*, “Restoring natural sensory feedback in real-time bidirectional hand prostheses,” *Sci. Transl. Med.*, vol. 6, no. 222, p. 222ra19-222ra19, 2014.
[171] D. R. Lesniak, S. A. Wellnitz, G. J. Gerling, and E. A. Lumpkin, “Statistical analysis and modeling of variance in the SA-I mechanoreceptor response to sustained indentation,” in *2009 Annual International Conference of the IEEE Engineering in Medicine and Biology Society*, 2009, pp. 6814–6817.
[172] V. E. Abraira and D. D. Ginty, “The sensory neurons of touch,” *Neuron*, vol. 79, no. 4, pp. 618–639, 2013.
[173] E. Gunther and S. O’Modhrain, “Cutaneous grooves: composing for the sense of touch,” *J. New Music Res.*, vol. 32, no. 4, pp. 369–381, 2003.
[174] C. Cipriani, J. L. Segil, F. Clemente, and B. Edin, “Humans can integrate feedback of discrete events in their sensorimotor control of a robotic hand,” *Exp. brain Res.*, vol. 232, no. 11, pp. 3421–3429, 2014.
[175] K. A. Kaczmarek, J. G. Webster, P. Bach-y-Rita, and W. J. Tompkins, “Electrotactile and vibrotactile displays for sensory substitution systems,” *IEEE Trans. Biomed. Eng.*, vol. 38, no. 1, pp. 1–16, 1991.
[176] L. H. Goldish and H. E. Taylor, “The Optacon: A Valuable Device for Blind Persons.,” *New Outlook Blind*, vol. 68, no. 2, pp. 49–56, 1974.
[177] C. Antfolk, M. D’Alonzo, B. Rosen, G. Lundborg, F. Sebelius, and C. Cipriani, “Sensory feedback in upper limb prosthetics,” *Expert Rev. Med. Devices*, vol. 10, no. 1, pp. 45–54, 2013.
[178] C. Bolzmacher, M. Hafez, M. B. Khoudja, P. Bernardoni, and

S. Dubowsky, “Polymer-based actuators for virtual reality devices,” in *Smart Structures and Materials 2004: Electroactive Polymer Actuators and Devices (EAPAD)*, 2004, vol. 5385, pp. 281–290.

[179] R. Pelrine, R. Kornbluh, Q. Pei, and J. Joseph, “High-speed electrically actuated elastomers with strain greater than 100%,” *Science (80-.).*, vol. 287, no. 5454, pp. 836–839, 2000.

[180] Y. Bar-Cohen and Y. Bar-Cohen, *Electroactive polymer (EAP) actuators as artificial muscles: reality, potential, and challenges*, vol. 136. SPIE press Bellingham, WA, 2004.

[181] H. S. Lee *et al.*, “Design analysis and fabrication of arrayed tactile display based on dielectric elastomer actuator,” *Sensors Actuators A Phys.*, vol. 205, pp. 191–198, 2014.

[182] I. M. Koo, K. Jung, J. C. Koo, J.-D. Nam, Y. K. Lee, and H. R. Choi, “Development of soft-actuator-based wearable tactile display,” *IEEE Trans. Robot.*, vol. 24, no. 3, pp. 549–558, 2008.

[183] T. Ninomiya, Y. Okayama, Y. Matsumoto, X. Arouette, K. Osawa, and N. Miki, “MEMS-based hydraulic displacement amplification mechanism with completely encapsulated liquid,” *Sensors Actuators A Phys.*, vol. 166, no. 2, pp. 277–282, 2011.

[184] M. Kawazoe, Y. Kosemura, and N. Miki, “Encoding and presentation of surface textures using a mechanotactile display,” *Sensors Actuators A Phys.*, vol. 261, pp. 30–39, 2017.

[185] B. M. Schena, “Haptic devices using electroactive polymers.” Google Patents, 27-Mar-2007.

[186] P. Saccomandi *et al.*, “Tactile piezoresistive sensors for robotic application: Design and metrological characterization,” in *2017 IEEE International Instrumentation and Measurement Technology Conference (I2MTC)*, 2017, pp. 1–6.

[187] L. Wang and Y. Li, “A review for conductive polymer piezoresistive composites and a development of a compliant pressure transducer,” *IEEE Trans. Instrum. Meas.*, vol. 62, no. 2, pp. 495–502, 2013.

[188] R. B. Katragadda and Y. Xu, “A novel intelligent textile technology based on silicon flexible skins,” *Sensors*

Actuators A Phys., vol. 143, no. 1, pp. 169–174, 2008.
[189] H.-K. Lee, J. Chung, S.-I. Chang, and E. Yoon, "Normal and shear force measurement using a flexible polymer tactile sensor with embedded multiple capacitors," *J. Microelectromechanical Syst.*, vol. 17, no. 4, pp. 934–942, 2008.
[190] K. Hosoda, Y. Tada, and M. Asada, "Anthropomorphic robotic soft fingertip with randomly distributed receptors," *Rob. Auton. Syst.*, vol. 54, no. 2, pp. 104–109, 2006.
[191] J. Wang, H. Sato, C. Xu, and M. Taya, "Bioinspired design of tactile sensors based on Flemion," *J. Appl. Phys.*, vol. 105, no. 8, p. 83515, 2009.
[192] G. Sziebig, B. Solvang, C. Kiss, and P. Korondi, "Vibro-tactile feedback for VR systems," in *Human System Interactions, 2009. HSI'09. 2nd Conference on*, 2009, pp. 406–410.
[193] A. U. Alahakone and S. M. N. A. Senanayake, "Vibrotactile feedback systems: Current trends in rehabilitation, sports and information display," in *Advanced Intelligent Mechatronics, 2009. AIM 2009. IEEE/ASME International Conference on*, 2009, pp. 1148–1153.
[194] T. Yamamoto, N. Abolhassani, S. Jung, A. M. Okamura, and T. N. Judkins, "Augmented reality and haptic interfaces for robot-assisted surgery," *Int. J. Med. Robot. Comput. Assist. Surg.*, vol. 8, no. 1, pp. 45–56, 2012.
[195] S. Choi and K. J. Kuchenbecker, "Vibrotactile display: Perception, technology, and applications," *Proc. IEEE*, vol. 101, no. 9, pp. 2093–2104, 2013.
[196] J. Sibert, J. Cooper, C. Covington, A. Stefanovski, D. Thompson, and R. W. Lindeman, "Vibrotactile feedback for enhanced control of urban search and rescue robots," in *Proceedings of the IEEE International Workshop on Safety, Security and Rescue Robotics*.
[197] C. Pacchierotti, S. Sinclair, M. Solazzi, A. Frisoli, V. Hayward, and D. Prattichizzo, "Wearable haptic systems for the fingertip and the hand: taxonomy, review, and perspectives," *IEEE Trans. Haptics*, vol. 10, no. 4, pp. 580–600, 2017.
[198] N. Caporusso, "A wearable Malossi alphabet interface for deafblind people," in *Proceedings of the working conference on Advanced visual interfaces*, 2008, pp. 445–448.

[199] A. M. Murray, R. L. Klatzky, and P. K. Khosla, “Psychophysical characterization and testbed validation of a wearable vibrotactile glove for telemanipulation,” *Presence Teleoperators Virtual Environ.*, vol. 12, no. 2, pp. 156–182, 2003.

[200] D. Tsetserukou, “HaptiHug: A novel haptic display for communication of hug over a distance,” in *International Conference on Human Haptic Sensing and Touch Enabled Computer Applications*, 2010, pp. 340–347.

[201] G. García-Valle, M. Ferre, J. Breñosa, R. Aracil, J. M. Sebastian, and C. Giachritsis, “Design and development of a multimodal vest for virtual immersion and guidance,” in *International Conference on Human Haptic Sensing and Touch Enabled Computer Applications*, 2016, pp. 251–262.

[202] R. Jimenez and A. M. Jimenez, “Blind waypoint navigation using a computer controlled vibrotactile belt,” in *Advances in Human Factors and System Interactions*, Springer, 2017, pp. 3–13.

[203] Y. H. Lee and G. Medioni, “RGB-D camera based wearable navigation system for the visually impaired,” *Comput. Vis. Image Underst.*, vol. 149, pp. 3–20, 2016.

[204] O. B. Kaul and M. Rohs, “Haptichead: A spherical vibrotactile grid around the head for 3D guidance in virtual and augmented reality,” in *Proceedings of the 2017 CHI Conference on Human Factors in Computing Systems*, 2017, pp. 3729–3740.

[205] V. A. de Jesus Oliveira, L. Brayda, L. Nedel, and A. Maciel, “Designing a vibrotactile head-mounted display for spatial awareness in 3d spaces,” *IEEE Trans. Vis. Comput. Graph.*, vol. 23, no. 4, pp. 1409–1417, 2017.

[206] K. O. Johnson and J. R. Phillips, “Tactile spatial resolution. I. Two-point discrimination, gap detection, grating resolution, and letter recognition,” *J. Neurophysiol.*, vol. 46, no. 6, pp. 1177–1192, 1981.

[207] I. D. Johnston, D. K. McCluskey, C. K. L. Tan, and M. C. Tracey, “Mechanical characterization of bulk Sylgard 184 for microfluidics and microengineering,” *J. Micromechanics Microengineering*, vol. 24, no. 3, p. 35017, 2014.

[208] P. Du, I.-K. Lin, H. Lu, and X. Zhang, “Extension of the beam theory for polymer bio-transducers with low aspect ratios

and viscoelastic characteristics," *J. Micromechanics Microengineering*, vol. 20, no. 9, p. 95016, 2010.
[209] R. T. Verrillo, "Psychophysics of vibrotactile stimulation," *J. Acoust. Soc. Am.*, vol. 77, no. 1, pp. 225–232, 1985.
[210] S. Brewster and L. M. Brown, "Tactons: structured tactile messages for non-visual information display," in *Proceedings of the fifth conference on Australasian user interface-Volume 28*, 2004, pp. 15–23.
[211] S. J. Bolanowski Jr, G. A. Gescheider, R. T. Verrillo, and C. M. Checkosky, "Four channels mediate the mechanical aspects of touch," *J. Acoust. Soc. Am.*, vol. 84, no. 5, pp. 1680–1694, 1988.
[212] F. Sorgini *et al.*, "Design and preliminary evaluation of haptic devices for upper limb stimulation and integration within a virtual reality cave," in *2016 6th IEEE International Conference on Biomedical Robotics and Biomechatronics (BioRob)*, 2016, pp. 464–469.
[213] A. Grinsted, J. C. Moore, and S. Jevrejeva, "Application of the cross wavelet transform and wavelet coherence to geophysical time series," *Nonlinear Process. Geophys.*, vol. 11, no. 5/6, pp. 561–566, 2004.
[214] L. A. Jones and N. B. Sarter, "Tactile displays: Guidance for their design and application," *Hum. Factors*, vol. 50, no. 1, pp. 90–111, 2008.
[215] R. Bogacz, E. Brown, J. Moehlis, P. Holmes, and J. D. Cohen, "The physics of optimal decision making: a formal analysis of models of performance in two-alternative forced-choice tasks.," *Psychol. Rev.*, vol. 113, no. 4, p. 700, 2006.
[216] C. Antfolk *et al.*, "Artificial redirection of sensation from prosthetic fingers to the phantom hand map on transradial amputees: vibrotactile versus mechanotactile sensory feedback," *IEEE Trans. neural Syst. Rehabil. Eng.*, vol. 21, no. 1, pp. 112–120, 2013.
[217] E. R. Kandel, J. H. Schwartz, T. M. Jessell, D. of B. and M. B. T. Jessell, S. Siegelbaum, and A. J. Hudspeth, *Principles of neural science*, vol. 4. McGraw-hill New York, 2000.
[218] G. Robles-De-La-Torre, "The importance of the sense of touch in virtual and real environments," *Ieee Multimed.*, vol. 13, no. 3, pp. 24–30, 2006.
[219] S. J. Bensmaia and L. E. Miller, "Restoring sensorimotor

function through intracortical interfaces: progress and looming challenges," *Nat. Rev. Neurosci.*, vol. 15, no. 5, p. 313, 2014.
[220] P. Bach-y-Rita, "Neurophysiological basis of a tactile vision-substitution system," *IEEE Trans. Man-Machine Syst.*, vol. 11, no. 1, pp. 108–110, 1970.
[221] P. Bach-y-Rita, C. C. Collins, F. A. Saunders, B. White, and L. Scadden, "Vision substitution by tactile image projection," *Nature*, vol. 221, no. 5184, p. 963, 1969.
[222] P. Bach-y-Rita, M. E. Tyler, and K. A. Kaczmarek, "Seeing with the brain," *Int. J. Hum. Comput. Interact.*, vol. 15, no. 2, pp. 285–295, 2003.
[223] P. Bach-y-Rita, K. A. Kaczmarek, M. E. Tyler, and J. Garcia-Lara, "Form perception with a 49-point electrotactile stimulus array on the tongue: a technical note," *J. Rehabil. Res. Dev.*, vol. 35, pp. 427–430, 1998.
[224] K. A. Kaczmarek, "Bach-Y-Rita, P.(1995). Tactile displays," *Virtual Environ. Adv. interface Des.*, pp. 349–414.
[225] O. Deroy and M. Auvray, "Reading the world through the skin and ears: A new perspective on sensory substitution," *Front. Psychol.*, vol. 3, p. 457, 2012.
[226] M. Auvray and E. Myin, "Perception with compensatory devices: From sensory substitution to sensorimotor extension," *Cogn. Sci.*, vol. 33, no. 6, pp. 1036–1058, 2009.
[227] F. Sorgini, R. Caliò, M. C. Carrozza, and C. M. Oddo, "Haptic-assistive technologies for audition and vision sensory disabilities," *Disabil. Rehabil. Assist. Technol.*, vol. 13, no. 4, pp. 394–421, 2018.
[228] C. Loscos *et al.*, "The Museum of Pure Form: touching real statues in an immersive virtual museum.," in *VAST*, 2004, pp. 271–279.
[229] H. Jörntell, F. Bengtsson, P. Geborek, A. Spanne, A. V Terekhov, and V. Hayward, "Segregation of tactile input features in neurons of the cuneate nucleus," *Neuron*, vol. 83, no. 6, pp. 1444–1452, 2014.
[230] V. Hayward and M. Cruz-Hernandez, "Tactile display device using distributed lateral skin stretch," in *Proceedings of the haptic interfaces for virtual environment and teleoperator systems symposium*, 2000, vol. 69, no. 2, pp. 1309–1314.
[231] V. Hayward, "A brief taxonomy of tactile illusions and

demonstrations that can be done in a hardware store," *Brain Res. Bull.*, vol. 75, no. 6, pp. 742–752, 2008.
[232] D. G. Caldwell, N. Tsagarakis, and A. Wardle, "Mechano thermo and proprioceptor feedback for integrated haptic feedback," in *Robotics and Automation, 1997. Proceedings., 1997 IEEE International Conference on*, 1997, vol. 3, pp. 2491–2496.
[233] V. G. Chouvardas, A. N. Miliou, and M. K. Hatalis, "Tactile displays: Overview and recent advances," *Displays*, vol. 29, no. 3, pp. 185–194, 2008.
[234] Y. Liu, Y. Yu, J. Yang, Y. Inai, and J. Wu, "Ability to recognize and identify the location of vibration stimulation on the fingers," in *2014 IEEE International Conference on Mechatronics and Automation*, 2014, pp. 1601–1606.
[235] C. Pacchierotti, D. Prattichizzo, and K. J. Kuchenbecker, "Cutaneous feedback of fingertip deformation and vibration for palpation in robotic surgery," *IEEE Trans. Biomed. Eng.*, vol. 63, no. 2, pp. 278–287, 2016.
[236] O. A. J. Van der Meijden and M. P. Schijven, "The value of haptic feedback in conventional and robot-assisted minimal invasive surgery and virtual reality training: a current review," *Surg. Endosc.*, vol. 23, no. 6, pp. 1180–1190, 2009.
[237] M. Tavakoli, R. V Patel, and M. Moallem, "A force reflective master-slave system for minimally invasive surgery," in *Intelligent Robots and Systems, 2003.(IROS 2003). Proceedings. 2003 IEEE/RSJ International Conference on*, 2003, vol. 4, pp. 3077–3082.
[238] M. E. H. Eltaib and J. R. Hewit, "Tactile sensing technology for minimal access surgery—a review," *Mechatronics*, vol. 13, no. 10, pp. 1163–1177, 2003.
[239] J. Peirs *et al.*, "A micro optical force sensor for force feedback during minimally invasive robotic surgery," *Sensors Actuators A Phys.*, vol. 115, no. 2–3, pp. 447–455, 2004.
[240] T. Hu, A. E. Castellanos, G. Tholey, and J. P. Desai, "Real-time haptic feedback in laparoscopic tools for use in gastro-intestinal surgery," in *International Conference on Medical Image Computing and Computer-Assisted Intervention*, 2002, pp. 66–74.
[241] M. Culjat, C.-H. King, M. Franco, J. Bisley, W. Grundfest, and

E. Dutson, “Pneumatic balloon actuators for tactile feedback in robotic surgery,” *Ind. Robot An Int. J.*, vol. 35, no. 5, pp. 449–455, 2008.

[242] A. Bicchi, E. P. Scilingo, E. Ricciardi, and P. Pietrini, “Tactile flow explains haptic counterparts of common visual illusions,” *Brain Res. Bull.*, vol. 75, no. 6, pp. 737–741, 2008.

[243] A. V Terekhov and V. Hayward, “The brain uses extrasomatic information to estimate limb displacement,” *Proc. R. Soc. B Biol. Sci.*, vol. 282, no. 1814, p. 20151661, 2015.

[244] F. Schumann and J. K. O’Regan, “Sensory augmentation: Integration of an auditory compass signal into human perception of space,” *Sci. Rep.*, vol. 7, p. 42197, 2017.

[245] E. M. Izhikevich, “Simple model of spiking neurons,” *IEEE Trans. neural networks*, vol. 14, no. 6, pp. 1569–1572, 2003.

[246] J. Miller and R. Ulrich, “On the analysis of psychometric functions: The Spearman-Kärber method,” *Percept. Psychophys.*, vol. 63, no. 8, pp. 1399–1420, 2001.

[247] H. Kerdegari, Y. Kim, and T. J. Prescott, “Head-mounted sensory augmentation device: Designing a tactile language,” *IEEE Trans. Haptics*, vol. 9, no. 3, pp. 376–386, 2016.

[248] A. Cassinelli, C. Reynolds, and M. Ishikawa, “Augmenting spatial awareness with haptic radar,” in *2006 10th IEEE International Symposium on Wearable Computers*, 2006, pp. 61–64.

[249] C. Bertram, M. H. Evans, M. Javaid, T. Stafford, and T. Prescott, “Sensory augmentation with distal touch: the tactile helmet project,” in *Conference on Biomimetic and Biohybrid Systems*, 2013, pp. 24–35.

[250] J. B. F. Van Erp, H. A. H. C. Van Veen, C. Jansen, and T. Dobbins, “Waypoint navigation with a vibrotactile waist belt,” *ACM Trans. Appl. Percept.*, vol. 2, no. 2, pp. 106–117, 2005.

[251] S. U. König *et al.*, “Learning new sensorimotor contingencies: Effects of long-term use of sensory augmentation on the brain and conscious perception,” *PLoS One*, vol. 11, no. 12, p. e0166647, 2016.

[252] L. F. Cuturi, E. Aggius-Vella, C. Campus, A. Parmiggiani, and M. Gori, “From science to technology: Orientation and mobility in blind children and adults,” *Neurosci. Biobehav. Rev.*, vol. 71, pp. 240–251, 2016.

[253] A. Destexhe and L. Foubert, “The Spikiss Project,” *First Publ. June*, 2016.
[254] B. Hannaford and A. M. Okamura, “Haptics,” in *Springer Handbook of Robotics*, Springer, United States, 2016.
[255] R. Velázquez and E. Pissaloux, “Tactile Displays in Human-Machine Interaction : Four Case Studies,” *Int. J. Virtual Real.*, 2008.
[256] B. D. Varalakshmi, J. Thriveni, K. R. Venugopal, and L. M. Patnaik, “Haptics: state of the art survey,” *Int. J. Comput. Sci. Issues*, vol. 9, no. 5, p. 234, 2012.
[257] R. S. Johansson and G. Westling, “Roles of glabrous skin receptors and sensorimotor memory in automatic control of precision grip when lifting rougher or more slippery objects,” *Exp. brain Res.*, vol. 56, no. 3, pp. 550–564, 1984.
[258] N. Yogeswaran *et al.*, “New materials and advances in making electronic skin for interactive robots,” *Adv. Robot.*, vol. 29, no. 21, pp. 1359–1373, 2015.
[259] O. Kroemer, C. H. Lampert, and J. Peters, “Learning dynamic tactile sensing with robust vision-based training,” *IEEE Trans. Robot.*, vol. 27, no. 3, pp. 545–557, 2011.
[260] M. Kaboli and G. Cheng, “Robust tactile descriptors for discriminating objects from textural properties via artificial robotic skin,” *IEEE Trans. Robot.*, vol. 34, no. 4, pp. 985–1003, 2018.
[261] Z. Su *et al.*, “Force estimation and slip detection/classification for grip control using a biomimetic tactile sensor,” in *Humanoid Robots (Humanoids), 2015 IEEE-RAS 15th International Conference on*, 2015, pp. 297–303.
[262] S. Shirafuji and K. Hosoda, “Detection and prevention of slip using sensors with different properties embedded in elastic artificial skin on the basis of previous experience,” *Rob. Auton. Syst.*, vol. 62, no. 1, pp. 46–52, 2014.
[263] K. Yao, M. Kaboli, and G. Cheng, “Tactile-based object center of mass exploration and discrimination,” in *Humanoid Robotics (Humanoids), 2017 IEEE-RAS 17th International Conference on*, 2017, pp. 876–881.
[264] B. W. White, “Perceptual findings with the vision-substitution system,” *IEEE Trans. Man-Machine Syst.*, vol. 11, no. 1, pp. 54–58, 1970.

[265] C. C. Collins, “Tactile television-mechanical and electrical image projection,” *IEEE Trans. man-machine Syst.*, vol. 11, no. 1, pp. 65–71, 1970.
[266] J. C. Bliss, M. H. Katcher, C. H. Rogers, and R. P. Shepard, “Optical-to-tactile image conversion for the blind,” *IEEE Trans. Man-Machine Syst.*, vol. 11, no. 1, pp. 58–65, 1970.
[267] D. W. Sparks, L. A. Ardell, M. Bourgeois, B. Wiedmer, and P. K. Kuhl, “Investigating the MESA (multipoint electrotactile speech aid): The transmission of connected discourse,” *J. Acoust. Soc. Am.*, vol. 65, no. 3, pp. 810–815, 1979.
[268] N. Ranasinghe, R. Nakatsu, H. Nii, and P. Gopalakrishnakone, “Tongue mounted interface for digitally actuating the sense of taste,” in *2012 16th Annual International Symposium on Wearable Computers (ISWC)*, 2012, pp. 80–87.
[269] N. Ranasinghe and E. Y.-L. Do, “Digital lollipop: Studying electrical stimulation on the human tongue to simulate taste sensations,” *ACM Trans. Multimed. Comput. Commun. Appl.*, vol. 13, no. 1, p. 5, 2017.
[270] H. Iwata, H. Yano, T. Uemura, and T. Moriya, “Food simulator: A haptic interface for biting,” in *Virtual Reality, 2004. Proceedings. IEEE*, 2004, pp. 51–57.
[271] A. Cruz and B. G. Green, “Thermal stimulation of taste,” *Nature*, vol. 403, no. 6772, p. 889, 2000.
[272] A. D. Wilson and M. Baietto, “Advances in electronic-nose technologies developed for biomedical applications,” *Sensors*, vol. 11, no. 1, pp. 1105–1176, 2011.
[273] A. Albini, S. Denei, and G. Cannata, “Human hand recognition from robotic skin measurements in human-robot physical interactions,” in *IEEE International Conference on Intelligent Robots and Systems*, 2017.
[274] M. Kaboli, K. Yao, D. Feng, and G. Cheng, “Tactile-based active object discrimination and target object search in an unknown workspace,” *Auton. Robots*, pp. 1–30, 2018.
[275] T. J. Prescott, M. E. Diamond, and A. M. Wing, “Active touch sensing,” *Philos. Trans. R. Soc. B Biol. Sci.*, 2011.
[276] D. Feng, M. Kaboli, and G. Cheng, “Active Prior Tactile Knowledge Transfer for Learning Tactual Properties of New Objects,” *Sensors*, vol. 18, no. 2, p. 634, 2018.
[277] U. B. Rongala, A. Mazzoni, and C. M. Oddo, “Neuromorphic Artificial Touch for Categorization of Naturalistic Textures,”

IEEE Trans. Neural Networks Learn. Syst., pp. 1–11, 2015.
[278] A. L. Hodgkin and A. F. Huxley, "A quantitative description of membrane current and its application to conduction and excitation in nerve," *J. Physiol.*, vol. 117, no. 4, pp. 500–544, 1952.
[279] E. M. Izhikevich, "Which model to use for cortical spiking neurons?," *IEEE Trans. Neural Networks*, vol. 15, no. 5, pp. 1063–1070, 2004.
[280] L. Massari *et al.*, "A Machine-Learning-Based Approach To Solve Both Contact Location And Force In Soft-Material Tactile Sensors."
[281] L. Massari, C. M. Oddo, E. Sinibaldi, R. Detry, J. Bowkett, and K. Carpenter, "Tactile Sensing and Control of Robotic Manipulator Integrating Fiber Bragg Grating Strain-Sensor," *Front. Neurorobot.*, vol. 13, p. 8, 2019.
[282] J. D'Abbraccio, L. Massari, A. Aliperta, C. M. Oddo, M. Zaltieri, and E. Palermo, "Design and Development of Large-Area FBG-Based Sensing Skin for Collaborative Robotics," pp. 1–4.
[283] L. Massari, A. Bulletti, S. Prasanna, M. Mazzoni, and F. Frosini, "A mechatronic platform for computer aided detection of nodules in anatomopathological analyses via stiffness and ultrasound measurements," pp. 1–13, 2019.
[284] D. Esposito, F. Lanotte, C. Mugnai, L. Massari, D. Camboni, and C. M. Oddo, "A neuromorphic model to match the spiking activity of Merkel mechanoreceptors with biomimetic tactile sensors for bioengineering applications."
[285] J. D'Abbraccio *et al.*, "Haptic Glove and Platform with Gestural Control For Neuromorphic Tactile Sensory Feedback In Medical Telepresence," *Sensors*, vol. 19, no. 3, p. 641, 2019.